

AN ERBIUM-DOPED 1-D FIBER-BRAGG GRATING AND ITS EFFECT UPON
ER³⁺ RADIATIVE SPONTANEOUS EMISSION

by

BRYAN S. BOGGS

A DISSERTATION

Presented to the Department of Physics
and the Graduate School of the University of Oregon
in partial fulfillment of the requirements
for the degree of
Doctor of Philosophy

December 2012

DISSERTATION APPROVAL PAGE

Student: Bryan S. Boggs

Title: An Erbium-Doped 1-D Fiber-Bragg Grating and Its Effect Upon Er³⁺ Radiative Spontaneous Emission

This dissertation has been accepted and approved in partial fulfillment of the requirements for the Doctor of Philosophy degree in the Department of Physics by:

Hailin Wang	Chair
Stephen Gregory	Member
Steve Kevan	Member
Mark Lonergan	Outside Member

and

Kimberly Andrews Espy	Vice President for Research & Innovation/Dean of the Graduate School
-----------------------	--

Original approval signatures are on file with the University of Oregon Graduate School.

Degree awarded December 2012

Copyright; 2012; Bryan Scott Boggs

DISSERTATION ABSTRACT

Bryan S. Boggs

Doctor of Philosophy

Department of Physics

December 2012

Title: An Erbium-Doped 1-D Fiber-Bragg Grating and Its Effect Upon Er^{3+} Radiative Spontaneous Emission

Spontaneous atomic emission is not a process of the isolated atom but rather a cooperative effect of the atom and the vacuum field. It is now well established that spontaneous radiative decay rates can be enhanced or suppressed through the effect of cavities comprising various types of discrete, reflective-mirror type, boundaries. The cavity effect is generally understood in terms of a cavity-induced modification of the vacuum spectral energy density. Recently, interest has grown in the possibility that systems characterized by distributed periodic boundary conditions, such as a spatially varying index of refraction, might be effective in controlling radiative atomic processes.

A semi-classical theory is given that enables an estimate of the size of the lifetime modification of a two-level radiator contained within a three-dimensionally incomplete photonic bandgap structure called a fiber-Bragg grating. Following this is an exploration of a specific system and its effect upon radiative spontaneous emission. It is found through fluorescence line narrowing and frequency hole burning measurements that the observation of lifetime modification of the specific system is complicated due to intra and inter Stark energy migration. A lifetime modification measurement then shows that no change in lifetime is observed beyond the error bars on the measurement results.

The tuning and coherence properties of a short-external-cavity diode laser that may be useful for future time-dependent spectroscopic measurements are examined using a fiber-based, self-heterodyne technique. Coherence properties during active frequency scans are characterized through analysis of time-dependent heterodyne beat signals at the output of a fiber interferometer.

CURRICULUM VITAE

NAME OF AUTHOR: Bryan S. Boggs

GRADUATE AND UNDERGRADUATE SCHOOLS ATTENDED:

University of Oregon, Eugene

DEGREES AWARDED:

Doctor of Philosophy, Physics, 2012, University of Oregon

Master of Science, Physics, 1996, University of Oregon

Bachelor of Science, Physics and Mathematics, 1995, University of Oregon

Bachelor of Music Education, 1989, University of Oregon

PROFESSIONAL EXPERIENCE:

Science Laboratory Preparator, University of Oregon, January 2010 to present

Graduate Research Assistant, University of Oregon, 1996 - 2001

Graduate Teaching Fellow, University of Oregon, 1995 - 1996

Physics Tutor, University of Oregon, 1992-1995

GRANTS, AWARDS, AND HONORS:

NKT Summer School Prize, Copenhagen, Denmark, 2001

Physics Prize, Department of Physics, University of Oregon, 1995

PUBLICATIONS:

Greiner, C., Boggs, B., Wang, T., Loftus, T. and Mossberg, T.W., “Cavity-accelerated superradiance and pulse area quantization”, *Opt. Photon. News* 12, p. 59 (2001).

Greiner, C., Boggs, B. and Mossberg, T.W., “Superradiant emission dynamics of an optically thin material sample in a short-decay-time optical cavity”, *Phys. Rev. Lett.*, 18, 85 (2000).

Mossberg, T. W., Greiner, C., Boggs, B., “Method and apparatus for laser frequency stabilization”, U.S. Pat. 6,034,976 (2000).

Greiner, C., Boggs, B., Loftus, T., Wang, T. and Mossberg, T.W., “Polarization-dependent Rabi frequency beats in the coherent response of Tm^{3+} in YAG”, *Phys. Rev. A* 60, 2657 (1999).

Greiner, C., Boggs, B., Wang, T. and Mossberg, T.W., “Laser frequency stabilization by means of optical self-heterodyne beat-frequency control”, *Opt. Lett.* 23, 1280 (1998).

Boggs, B., Greiner, C., Wang, T., Lin, H. and Mossberg, T.W., “Simple high-coherence rapidly tunable external-cavity diode laser”, *Opt. Lett.* 23, 1906 (1998).

TABLE OF CONTENTS

Chapter	Page
I. INTRODUCTION	1
Premise.....	3
Topical Outline	4
II. BACKGROUND	6
The Two-Level Atom	7
Rabi Frequency and Pulse Area.....	7
Spontaneous Emission as Radiative Emission Stimulated by the Vacuum Field.....	9
Random Walk Model for Spontaneous Emission of a Two-Level Atom.....	10
Quantum Light Field Driving the Two-Level Atom.....	13
Discrete-Reflector Cavities.....	14
Distributed-Reflector Cavities	15
Photonic Bandgap Structure	16
Optical Fiber Operating Principle: Total Internal Reflection	17
Optical Losses.....	19
Material Considerations	20
Transverse Light Mode Considerations	21
Other Considerations	22

Chapter	Page
Fiber-Bragg Gratings	23
The Making of a Fiber-Bragg Grating	25
Properties of Fiber-Bragg Gratings.....	26
FBG Effect on the Spontaneous Emission Rate of a Two-level Atom	28
III. REAL SYSTEM: ERBIUM-GLASS CASE STUDY	30
Material Parameters	31
The FLN Sample.....	33
The Cryostat.....	34
Fluorescence Line Narrowing Experiment: Experimental Setup	36
The Fluorescence Line Narrowing Data	41
Discussion of Fluorescence Line Narrowing Data	72
Frequency Hole-Burning Experiment: Experimental Setup.....	74
The Frequency Hole-Burning Data.....	76
Discussion of the Frequency Hole-Burning Data	84
IV. LIFETIME MODIFICATION MEASUREMENT: EXPERIMENTAL ATTEMPTS.....	87
First Attempt: Experimental Setup	88
First Attempt: Transmission Versus Wavelength of Sample.....	92
Fractional Lifetime Change Versus Wavelength.....	94
Second Attempt: Experimental Setup.....	97

Chapter	Page
Second Attempt: Data	99
Possible Future Attempt.....	100
V. CONSTRUCTION AND CHARACTERIZATION OF A RAPIDLY TUNABLE LASER SYSTEM	102
Description of System.....	103
Tuning.....	106
Self-Heterodyned vs. Actual Laser Frequency Modeling and Interpretation	106
Experimental Results: Quiescent Linewidth.....	109
Tuning Characteristics	109
Frequency-Swept Coherence	110
Locking Suggestions.....	113
VI. CONCLUSION.....	114
REFERENCES CITED.....	115

LIST OF FIGURES

Figure	Page
2.1. Schematic of a two level atom	8
2.2. Pseudospin resonantly driven by electromagnetic field.....	11
2.3. Side view of a typical discrete-reflector atom/cavity implementation ...	14
2.4. Side view of a distributed-reflector atom/cavity implementation.....	16
2.5. Side view of a typical atom/PBGS implementation	17
2.6. Light ray undergoing total internal reflection	18
2.7. Light ray traveling down a fiber core undergoing total internal reflection	19
2.8. Illustration of step and continuous variation of refractive index	20
2.9. Fundamental field mode amplitude vs. radial distance.....	22
2.10. A fiber-Bragg grating in a single mode fiber.....	23
2.11. Transmission versus wavelength for light incident on a fiber-Bragg grating.....	24
2.12. Illustration of phase mask technique for inscribing fiber-Bragg gratings.....	26
2.13. Reflectivity versus wavelength for a 1 cm length grating	28
3.1. Energy level structure of an erbium-doped glass fiber	31
3.2. Energy-level Stark splittings of the $^4I_{13/2} - ^4I_{15/2}$ transition	32
3.3. Schematic of fiber sample.....	34
3.4. Simplified schematic of cryostat.....	35

Figure	Page
3.5. Experimental setup for fluorescence line narrowing measurements	37
3.6. Representation of optical chopper wheel	39
3.7. Schematic of spectrometer and detector apparatus	40
3.8. Fluorescence power versus wavelength for 1510.00 nm excitation	42
3.9. Fluorescence power versus wavelength for 1512.50 nm excitation	43
3.10. Fluorescence power versus wavelength for 1515.00 nm excitation	44
3.11. Fluorescence power versus wavelength for 1517.50 nm excitation	45
3.12. Fluorescence power versus wavelength for 1520.00 nm excitation	46
3.13. Fluorescence power versus wavelength for 1522.50 nm excitation	47
3.14. Fluorescence power versus wavelength for 1525.00 nm excitation	48
3.15. Fluorescence power versus wavelength for 1527.50 nm excitation	49
3.16. Fluorescence power versus wavelength for 1530.00 nm excitation	50
3.17. Fluorescence power versus wavelength for 1532.50 nm excitation	51
3.18. Fluorescence power versus wavelength for 1535.00 nm excitation	52
3.19. Fluorescence power versus wavelength for 1537.50 nm excitation	53
3.20. Fluorescence power versus wavelength for 1540.00 nm excitation	54
3.21. Fluorescence power versus wavelength for 1542.50 nm excitation	55
3.22. Fluorescence power versus wavelength for 1545.00 nm excitation	56
3.23. Fluorescence power versus wavelength for 1547.50 nm excitation	57
3.24. Fluorescence power versus wavelength for all excitation wavelengths.....	58

Figure	Page
3.25. Power of direct transition fluorescence peak versus peak wavelength	59
3.26. Wavelength difference between broad and narrow features	60
3.27. Area of broad spectral feature versus excitation wavelength	61
3.28. Fluorescence power versus wavelength for 1510.00 nm excitation	62
3.29. Fluorescence power versus wavelength for 1520.00 nm excitation	63
3.30. Fluorescence power versus wavelength for 1530.00 nm excitation	64
3.31. Fluorescence power versus wavelength for 1540.00 nm excitation	65
3.32. Fluorescence power versus wavelength for 1550.00 nm excitation	66
3.33. Fluorescence power versus wavelength for 1560.00 nm excitation	67
3.34. Fluorescence power versus wavelength for 1570.00 nm excitation	68
3.35. Fluorescence power versus wavelength for all excitation wavelengths.....	69
3.36. Spectrometer background noise with fluorescence light blocked.....	70
3.37. Fluorescence power versus wavelength for 980 nm excitation	71
3.38. Schematic outline for hole-burning experiment	74
3.39. Interferometer's transmission versus time for frequency chirped laser	76
3.40. 3 μ W pump hole burning data	77
3.41. 0.5 μ W pump hole burning data	78
3.42. 100nW pump hole burning data.....	79

Figure	Page
3.43. 10nW pump hole burning data.....	80
3.44. 1nW pump hole burning data.....	81
3.45. Decay constant versus pump power.....	82
3.46. Hole width versus pump power	83
4.1. Experimental setup for first series of lifetime variation measurement attempts.....	88
4.2. Diagram of optical chopper wheel employed in ionic lifetime measurements.....	90
4.3. Schematic of erbium doped fiber-Bragg grating sample	91
4.4. Experimental setup for measuring transmission at 4.5 K of sample	93
4.5. Transmission versus wavelength of sample at 4.5 K.....	93
4.6. The fractional lifetime change for the sample and experimental setup	94
4.7. Fluorescence decay versus time for a single trace recorded at 1521.2 nm	95
4.8. Fluorescence decay versus time for trace recorded at 1521.2 nm	96
4.9. Experimental setup for second lifetime variation measurement attempt.....	97
4.10. Two wavelength ionic lifetime measurement of sample and second experimental setup	99

Figure	Page
5.1. Littrow grating laser configuration	103
5.2. Schematic of experimental setup	105
5.3. Interferometer intensity beat signal linewidth as a function of laser linewidth	108
5.4. Interferometer output intensity beat signal versus time	110
5.5. Average cross-correlation magnitude of simulated beat signals.....	112

CHAPTER I

INTRODUCTION

Spontaneous atomic emission is not a process of the isolated atom but rather a cooperative effect of the atom and the vacuum field. In a famous paper in 1946 [1], Purcell pointed out that the probability of spontaneous emission may be increased by coupling the atom to a resonant reservoir. It is now well established that spontaneous radiative decay rates can be enhanced or suppressed through the effect of cavities comprising various types of discrete, reflective-mirror type, boundaries. The cavity effect is generally understood in terms of a cavity-induced modification of the vacuum spectral energy density, i.e., in the strength of the electromagnetic reservoir that drives spontaneous radiative decay. A variety of experiments have been reported which demonstrate either suppression or enhancement, or both, of the radiative spontaneous emission rate of atoms placed within these discrete cavities [2-6].

Recently, interest has grown in the possibility that systems characterized by distributed periodic boundary conditions, such as a spatially varying index of refraction, might be effective in controlling radiative atomic processes [7-14]. Interest in periodic refractive index structures, sometimes called photonic bandgap materials, stems in part from the notion that such systems can display photonic bandstructure, and in some instances even exhibit bandgaps, i.e., spectral regions in which no photonic modes exist. Physically, this results from Bragg reflection of electromagnetic waves off the periodic material layers. Atoms resonant at frequencies within a three-dimensional spatially-

complete photonic bandgap will, according to the prevailing view, exhibit a complete suppression of spontaneous decay. A series of field-initiating papers [15-18] describes the optical properties of periodic dielectric structures as well as their effect on the radiative properties of atoms placed within the structures. The case of a complete photonic bandgap provides a natural focus of attention but represents, in fact, only an extreme limit of a continuum of interesting scenarios wherein the presence of periodic structure perturbs the electromagnetic vacuum, imbuing it features not found in spatially homogeneous environments. This consideration, combined with the fact that the fabrication of materials whose periodic index variations act to create complete three-dimensional photonic bandgaps has proven challenging, provides strong motivation for the study of vacuum-mediated processes in diverse types of periodic structures – even those lacking complete three-dimensional photonic bandgaps.

Following an exploration of a specific system and its effect upon radiative spontaneous emission, the tuning and coherence properties of a short-external-cavity diode laser that may be useful for future time dependent spectroscopic measurements are examined using a fiber-based, self-heterodyne technique. Coherence properties during active frequency scans are characterized through analysis of time-dependent heterodyne beat signals at the output of a fiber interferometer.

Premise

Can one expect to see a modification of the spontaneous emission rate of a radiator spatially contained within a type of three-dimensionally incomplete photonic bandgap material called a fiber-Bragg grating?

This question is addressed by theoretically analyzing the spontaneous radiation of a two-level atom contained within a fiber-Bragg grating. It is shown that the spontaneous radiation rate is expected to be suppressed for a two-level atom spatially contained within a fiber-Bragg grating whose optical transition frequency is resonant with the fiber-Bragg-grating's photonic bandgap. That is, if the atom is spatially located deep within a grating of sufficiently high reflectivity, then the amount of suppression expected is equal to the solid angle ratio of the perturbed environment to unperturbed environment that the atom experiences.

The presentation of a case study of a real system follows this theoretical discussion. This case study provides a material parameter analysis for an Erbium-glass system that may be used to study the radiative spontaneous emission of ions within a fiber-Bragg grating and reveals that, given the system under study, an experiment to measure the suppression of the erbium ion's spontaneous emission rate is complicated due to the characteristics of the real system. That is, the effects of intra/inter Stark-level energy migration dynamics increase greatly the complexity of the system over that of the theoretically analyzed, above mentioned, two-level system. A description of experimental attempts to measure the suppression of ionic spontaneous emission and a discussion of these attempts follows.

Topical Outline

Chapter I provides a brief background, motivation and introduction to the existing research conducted in this field, and states the premise of the Dissertation. An outline of the path to be taken that addresses the premise is also given.

Background material concerning an atom interacting with an electromagnetic field is given in Chapter II. This analysis begins with a description of the linear dipole oscillator and is followed by an explication of the two-level atom. With the development of the two-level atom accomplished, the next step is to formulate the semi-classical picture of a two-level atom interacting with a classical electromagnetic field. It is with this semi-classical picture that an estimate of the spontaneous emission rate of the two-level atom is given. It is shown that a full quantum treatment, with both atom and field quantized, yields the same result as the semi-classical approach for the estimate of the spontaneous emission rate of the two-level atom. After this, optical fiber, photonic bandgap structures and fiber-Bragg gratings and their optical properties are described.

A case study of a real system is given in Chapter III, beginning with a physical description of the rare-earth-doped glass material and the physical parameters associated with this material, e.g., dimensions, level structure, absorption and doping concentration. Following, is a spectroscopic and holeburning analysis of the material's optical parameters. A discussion of the energy migration dynamics found in the spectroscopic results is given. Finally, a conclusion as to the estimated size of the lifetime modification effect given the system under study is provided.

Chapter IV constitutes a detailed description of the material and optical properties of the sample employed in the experimental attempt to measure suppression of the ionic spontaneous emission rate. The experimental setup, mode of detection and results of the attempted measurements are also provided. A description of the methods used to eliminate some systematic errors and the misleading signals they produced is given.

Chapter V describes the construction and subsequent characterization of the quiescent and frequency-swept coherence properties of a rapidly-tunable external-cavity diode laser.

Chapter VI briefly recaps the motivation for radiative lifetime modification and the physical system explored in this work. A possible future pathway forward to the experimental realization of measurable lifetime modification in the presently considered system is restated.

CHAPTER II

BACKGROUND

An atom interacts with light through the coupling between its electrons and the electromagnetic field associated with the light. Under the assumption that the electrons are bound into an ionic core, such that the whole electron/ion system is electrically neutral and that the electrons oscillate about their equilibrium positions with small amplitudes, the atom couples to the electromagnetic field through its electric dipole moment. See reference [19] for a more detailed description of the first three sections of this chapter.

A very basic property of a linear dipole oscillator is that it produces light. That is, it radiates energy and, as a consequence, its dipole equation of motion has a damping term and is of the form

$$\ddot{x} + \Gamma \dot{x} + \omega_a^2 x = \frac{e}{m} E \quad (2-1)$$

,where x is the dipole amplitude, Γ is the incoherent radiative damping factor, ω_a is the natural oscillation frequency of the dipole, $e(m)$ is the electron charge (mass), and E is the electric field strength along the dipole. The radiative lifetime or the average time in which the linear dipole oscillator radiates its energy, is proportional to $1/\Gamma$. The linear dipole oscillator picture does not take into account the quantum nature of the atoms as does the two-level atom.

The Two-Level Atom

The electronic energy levels of an atom are quantized or discrete by nature. The semi-classical theory of atom/field interaction is one which employs an atom with quantized energy levels interacting with a classical field. A two level atom is an idealization, but one which may not (in usual circumstances) be far from the truth. Consider an atom with energy levels given by

$$\begin{aligned} E_+ &= \hbar\omega_+ \\ E_- &= \hbar\omega_- \end{aligned} \tag{2-2}$$

, where $\omega_+ > \omega_-$. (see Fig. 2.1). If the electromagnetic field has sufficiently narrow spectral width compared to the energy separation between the atomic energy levels under consideration and is nearly resonant with the atomic level transition, i.e., $\omega \approx \omega_+ - \omega_-$. then the two level approximation is a good one. A two-level atom in the presence of a light field may exchange energy with the field. A measure of this process is the Rabi frequency.

Rabi Frequency and Pulse Area

For a two-level atom/light-field system with zero atom-field detuning, the inversion or energy of the atom will make oscillations with a frequency that is associated with the dipole interaction energy $E_{int} = -d_r \cdot E$, where d_r is the dipole moment and E is the field amplitude. That is, the oscillation frequency is

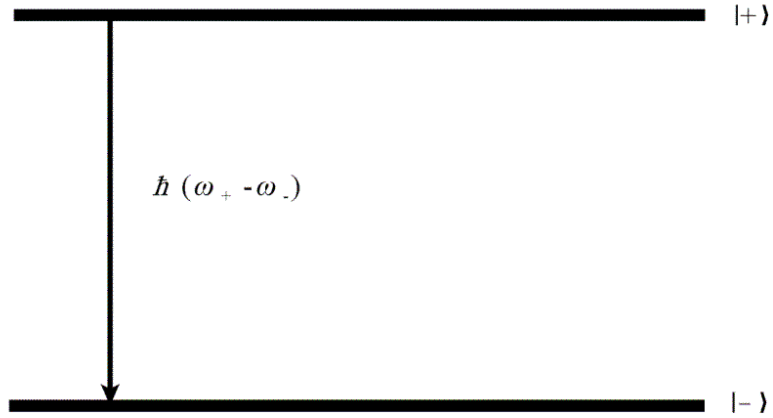


Figure 2.1. Schematic of a two level atom.

$$\Omega = \frac{|d_r||E|}{\hbar} \quad (2-3)$$

, where Ω is called the Rabi frequency. A quantity called the pulse area is defined to be, for a time invariant electric field amplitude, the Rabi frequency times the time the field is applied. A more general expression for the pulse area is given by

$$\Theta(t) = \int_{-\infty}^t \Omega(t') dt'. \quad (2-4)$$

Now that Rabi frequency and pulse area have been discussed they may be used to derive the cavity mediated spontaneous emission rate of an atom in a cavity.

Spontaneous Emission as Radiative Emission Stimulated by the Vacuum Field

Radiative emission from an atom is generally considered to be of two types. The first type is spontaneous emission. That is, radiative emission that occurs in a seemingly spontaneous manner from an excited atom. The second type is stimulated emission. That is, radiative emission that occurs from an excited atom in a sympathetic response to an applied electromagnetic field. It has been found that spontaneous emission may be thought of as emission stimulated by the vacuum field [20-21]. It is also known that the rate in which an atom is stimulated to emit is proportional to the energy density of the light field interacting with the atom [22]. In this light, with knowledge of the characteristics of the vacuum field interacting with the atom, the spontaneous emission rate of a two-level atom may be calculated.

Consider now, a single mode of the vacuum field with specific energy density $\hbar\omega_k/(2V_k)$, where V_k is an appropriate choice for the modal volume. The general classical result for the energy density of an electromagnetic field is

$$u = \epsilon_0 E^2 \quad (2-5)$$

,where ϵ_0 is the permittivity of free space . Equation (2-5), with the previous choice for the specific vacuum field energy density, leads to a vacuum field amplitude

$$E_{vac} = \sqrt{\frac{\hbar\omega_k}{2\epsilon_0 V_k}}. \quad (2-6)$$

Given the result in equation (2-6), the Rabi frequency associated with an atom/vacuum-field system is

$$\Omega_{vac} = \frac{|d_r||E_{vac}|}{\hbar}. \quad (2-7)$$

Neglecting decoherence, the atom will evolve in a continuous and directional manner with the frequency given in equation (2-7).

Random Walk Model for Spontaneous Emission of a Two-Level Atom

Consider an initially excited two-level atom in a perturbed, non-uniform environment, e.g., a cavity or some more general set of boundary conditions, where the perturbation concerns only a single resonant mode of the electromagnetic field. The time evolution of the pseudospin (Bloch vector) ρ describing the system may be thought of as making a random walk starting at the North pole (see fig. 2.2) where w represents the inversion and v represents the absorptive component of the dipole moment. The step size of the random walk Θ_c is defined to be the pulse area attained from the coherent evolution of the Bloch vector before a random phase jump occurs between the atom's dipole oscillation and the vacuum field.

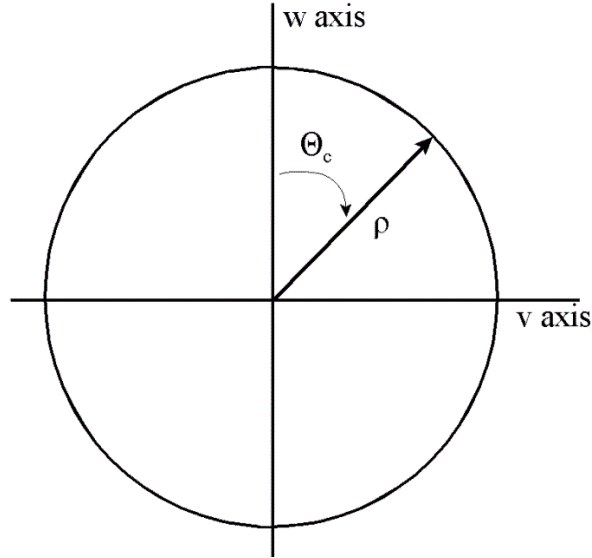


Figure 2.2. Pseudospin resonantly driven by electromagnetic field.

That is,

$$\Theta_c = \Omega_{vac} \cdot T_c \quad (2-8)$$

where T_c is the average time before a phase jump. The phase jump may be produced by either a dephasing event acting on the field (e.g., a photon leaking out of a cavity) or a dephasing event acting on the atomic dipole oscillation (e.g., a scattering event which abruptly alters the atomic dipole evolution). When the vacuum field is weak enough so that the coherent evolution of the Bloch vector is a small fraction of π before a dephasing event occurs, the Bloch vector “walks” from the North pole to the South taking a great number of steps, reversing its direction many times, eventually winding up at the South pole. Since the probability for evolving toward the North pole equals the probability of evolving toward the South pole the probability for the Bloch vector being N steps from the North pole is $N^{1/2}$. Therefore, the root mean square (rms) pulse area is given by

$$\Theta_{rms} = \sqrt{N}\Theta_c. \quad (2-9)$$

The number of steps the Bloch vector takes is given by

$$N = \frac{t}{T_c}, \quad (2-10)$$

where t is the time that the atomic dipole interacts with the vacuum field. To find the time the dipole takes to incoherently evolve from the North pole to the South pole equations 2-8 through 2-10 can be used and yield

$$t_\pi = \frac{\pi^2}{T_c \cdot \Omega_{vac}^2}. \quad (2-11)$$

The rate A_c at which the dipole loses its energy (radiates a photon) or its spontaneous emission rate is approximately given by the inverse of equation (2-11), and is

$$A_c = \frac{2T_c \cdot \Omega_{vac}^2}{\pi}. \quad (2-12)$$

Considering an atom where only two terms influence the spontaneous emission rate, one coming from coupling to an unperturbed environment and one from a coupling to a perturbed environment, the total spontaneous emission rate can be written as

$$A_T = A_\beta \left(1 - \frac{\Phi_c}{4\pi}\right) + A_c \frac{\Phi_c}{4\pi}, \quad (2-13)$$

where A_{fs} is the unperturbed (free space) spontaneous emission rate and Φ_c is the solid angle over which the atom interacts with the perturbed environment. Equation (2-12) shows that when the vacuum Rabi frequency Ω_{vac} is small and/or the coherent atom/field interaction time T_c is small, A_c may be much less than A_{fs} so that the change from A_{fs} in A_T is controlled almost entirely by that solid angle factor in the A_{fs} term of equation (2-13).

Quantum Light Field Driving the Two-Level Atom

The above analysis concerning the cavity mediated spontaneous emission rate of a two-level atom simplifies the situation by considering a classical light field interacting with a quantized two-level atom. When the problem of calculating the cavity mediated spontaneous emission rate is given the full quantum treatment from the beginning, the end result, within certain physical limits, is the same as that derived in the semi-classical approach, i.e., A_c of equation (2-12) above.

The fully quantum approach involves starting from a Jaynes-Cummings Hamiltonian [23] describing the interaction of an atom and a cavity, modifying the Hamiltonian to include cavity losses, assuming a weak atom/cavity coupling and finally determining the equation of motion for the upper state density operator. This procedure yields

$$\Gamma_{cav}(\Delta_{AC}) = \frac{g^2 \gamma}{\Delta_{AC}^2 + \left(\frac{\gamma}{2}\right)^2}, \quad (2-14)$$

where Δ_{AC} is the atom cavity detuning, g is the atom-cavity mode coupling factor and γ_C is the cavity damping rate. For zero atom/cavity detuning this expression is equivalent to the expression for the spontaneous emission rate given in equation (2-12).

Now that the cavity mediated spontaneous emission rate has been calculated in the semi-classical approach and has been found to agree with the fully-quantum approach, the next topic to explore is that of cavities.

Discrete-Reflector Cavities

The types of optical cavities used in scientific experiments are many and diverse. A typical cavity consists of two or more discrete reflective elements within which a sample may be situated and may resemble figure 2.3. The cavity is of a discrete-reflector

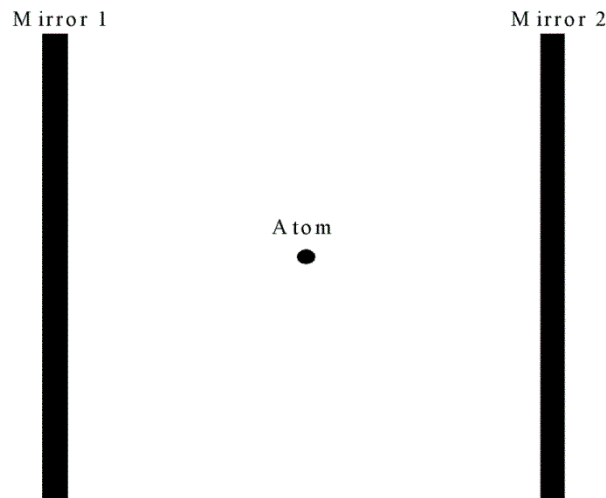


Figure 2.3. Side view of a typical discrete-reflector atom/cavity implementation.

type in the sense that the boundary regions (the penetration depths of the light into the mirror surfaces) are small compared to the distance between the mirrors. The discrete mirrors are usually optical quality glass which is coated with a material that has the desired optical properties (reflection, transmission, absorption, etc.) for the wavelength of light used to probe the atom/cavity system. The mirrors may also have a finite radius of curvature (not necessarily symmetric), as opposed to the symmetric (infinite radius of curvature mirrors) cavity depicted in figure 2.3. Neglecting material absorption, the optical properties of such a cavity depend upon the reflection coefficient, curvature radius, the size and separation distance of the mirrors. A more general type of cavity is the distributed-reflector cavity discussed next.

Distributed-Reflector Cavities

A distributed-reflector cavity employs a more general or distributed set of boundary conditions. That is, a distributed structure may be exploited to produce a non-discrete reflective environment. An implementation of a these distributed-reflector cavities may look like that shown in figure 2.4. In figure 2.4 two distributed structures are used as reflective elements. The structures usually consist of an optically transparent material (usually fabricated) wherein the refractive index varies about a mean value on a length scale that is of the order of the wavelength of light employed to probe the atom/cavity system. The reflection coefficient of an individual refractive index layer is usually very small compared to the reflection coefficient of the discrete boundary mirror shown in figure 2.3 above. Thus, the light traverses many refractive index layers before

scattering or reflecting backwards. The optical properties (again neglecting material absorption) of such a cavity depend upon the spatial period and the amplitude of the refractive index modulation, the length of the distributed reflector, and the distance between the distributed reflectors. The distributed-reflector planes do not usually have curvature but can be angled with respect to the optical axis.

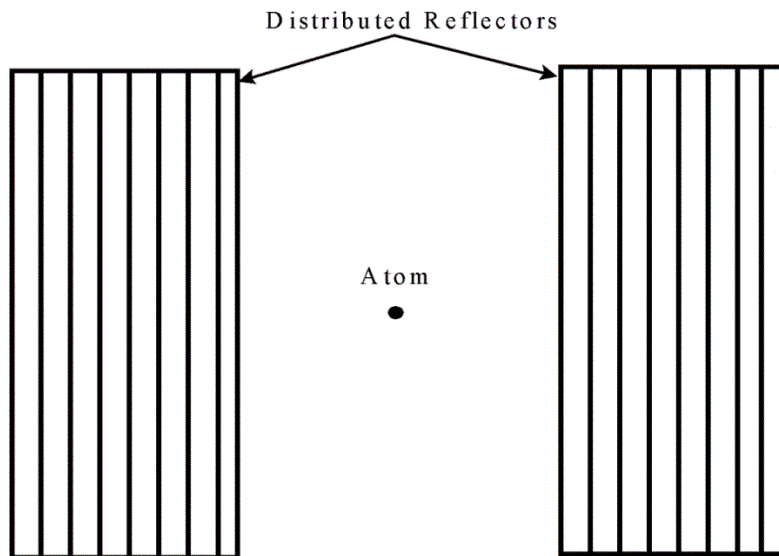


Figure 2.4. Side view of a distributed-reflector atom/cavity implementation.

Photonic Bandgap Structure

In figure 2.5 a different (but related) type of structure known as a photonic bandgap structure (PBGS) is shown.

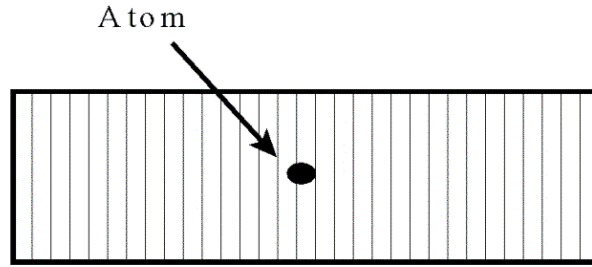


Figure 2.5. Side view of a typical atom/PBGS implementation.

This is a type of a generalized cavity usually consisting of a single distributed reflector that is of the same nature as the distributed reflectors shown in figure 2.4.

The optical properties of the PBGS depend upon the dimensionality and detailed geometry of the periodic structure, the period and amplitude of refractive index modulation, the length of the structure and the phase relation between the layers. PBGS have been created in 1, 2 and 3 dimensions [24-27]. The rest of this section will describe, in more detail, a pseudo one-dimensional PBGS called a fiber-Bragg grating that is formed within optical fiber, and its optical properties. To start this explanation a brief introduction to optical fiber should be given.

Optical Fiber Operating Principle: Total Internal Reflection

The operating principle of optical fiber is total internal reflection. It has been known from the nineteenth century that when light is incident on a lesser valued refractive-index medium from a higher valued refractive-index medium the possibility of

total reflection exists. For a more detailed description of this section see [28]. Light that is incident upon the boundary at an angle greater than a critical angle given by

$$\Theta_c = \sin^{-1}\left(\frac{n_t}{n_i}\right) \quad (2-15)$$

where n_i (n_t) is the refractive index of the medium of which the light is incident from (transmitted to), is totally reflected as shown in figure 2.6.

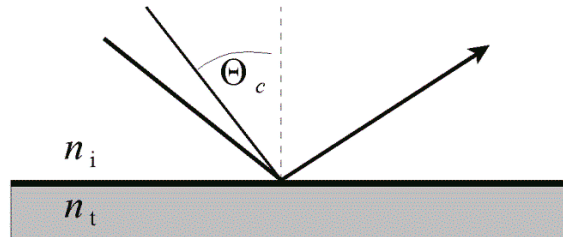


Figure 2.6. Light ray undergoing total internal reflection.

An optical fiber is usually composed of three layers. The innermost layer, where the light is confined, is called the core. The middle layer called the cladding has a refractive index that is less than that of the core providing the conditions for total internal reflection within the core. The outermost layer is usually a protective plastic material that mechanically stabilizes the glass cladding. Light initially in the fiber's core is guided or confined within the core, with core (cladding) material refractive index given by n_c (n_{cl}), by the fact that (in the ray picture) the light is incident upon the core/cladding boundary at angles that are always larger than the critical angle required for total internal reflection.

Figure 2.7 depicts this case, where it is indicated that no light leaks out of the core and into the cladding.

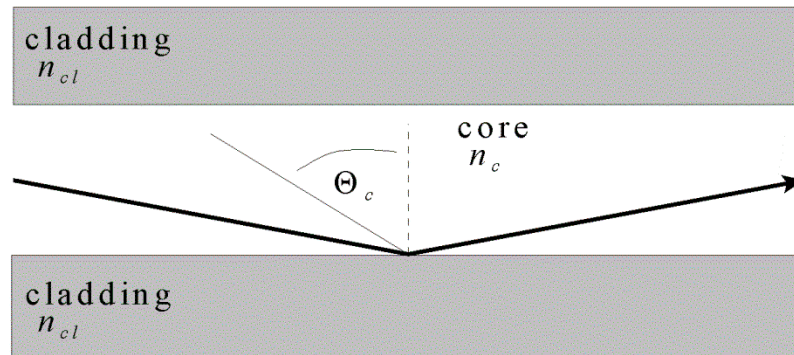


Figure 2.7. Light ray traveling down a fiber core undergoing total internal reflection.

Optical Losses

Optical fiber can transmit light very long distances (1000's of kilometers) with the chief attenuating factor being not loss of light due to transmission through the core-cladding boundary but material absorption of light by the silica, OH ion impurities within the silica and Rayleigh scattering off density fluctuations within the core itself. Taken together these loss mechanisms leave a low loss region around 1550nm. The losses in this wavelength region are typically around 0.2dB per kilometer.

Material Considerations

The core and cladding materials are usually composed of silica glass, where the refractive index difference is realized by the addition of dopants to the core and/or cladding. Germanium or phosphorus such as, GeO_2 and P_2O_5 may be added to the core to increase its refractive index while boron or fluorine may be added to the cladding to decrease its refractive index. The refractive index profile across the core/cladding boundary may be of a discrete or continuous nature as shown in figure 2.8.

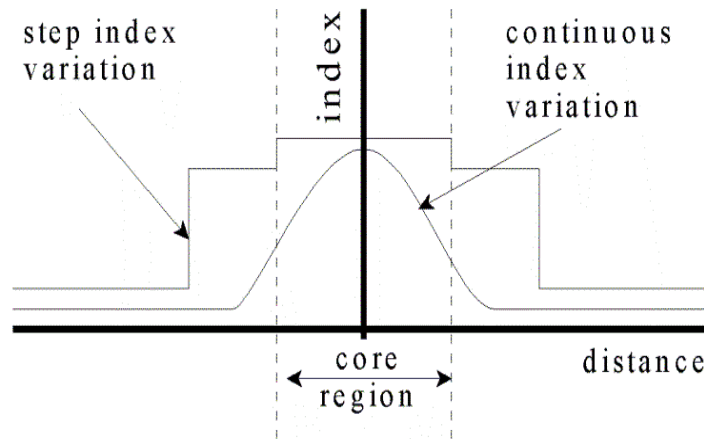


Figure 2.8. Illustration of step and continuous variation of refractive index.

Transverse Light Mode Considerations

Optical fiber can be single mode or multimode. This designation refers to the transverse characteristics of the light carried down the fiber's core. A single mode fiber supports the propagation of only the fundamental transverse mode of light. The nature of the mode is dictated by the material, geometrical and dimensional factors of the fiber's core and cladding and for single mode fiber the transverse intensity profile is very close to Gaussian. The condition for single-mode behavior is $V \leq 2.405$ where,

$$V = k_0 a \sqrt{n_c^2 - n_{cl}^2} \quad (2-16)$$

is called the normalized frequency or V -number, $k_0 = 2\pi/\lambda$, λ is the wavelength of light and a is the core radius. Due to the cylindrical geometry of the core/cladding boundary, Bessel functions are found to be solutions of the transverse portion of the wave equation for the electric field in the core. When $J_0(V) = 0$ for the smallest V , only the fundamental mode will exist in the core. That is, when $V \leq 2.405$ the fiber is said to be single mode for the given wavelength. Equation (2-16) may be solved for a cut-off wavelength λ_c where V is set to 2.405. For all wavelengths greater than λ_c , for a given fiber, the fiber is said to be single mode. Outside the core, in the cladding, the field decays exponentially. The transverse profile of the fundamental mode electric field is usually approximated by a Gaussian profile as shown in figure 2.9.

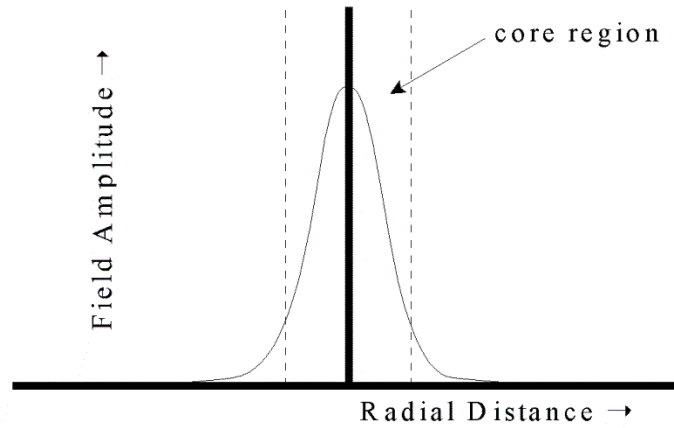


Figure 2.9. Fundamental field mode amplitude vs. radial distance.

Other Considerations

Besides those mentioned above, there are many other characteristics of light in optical fiber that may be considered. For example, chromatic dispersion occurs because the refractive index is not a constant as indicated above but is a slowly varying function of wavelength. This causes light of different wavelengths to propagate down the fiber with slightly different velocities. In addition, optical fiber can be of the polarization preserving type or polarization non-preserving type. Fiber that preserves the light polarization is made by preferentially stressing the core along one radial direction or by changing the core geometry from cylindrical to elliptical.

Fiber-Bragg Gratings

The simplest form of a fiber-Bragg grating is that of a single mode optical fiber with a periodic refractive-index modulation along the core as shown in figure 2.10. For a more detailed description of fiber Bragg gratings see [29].

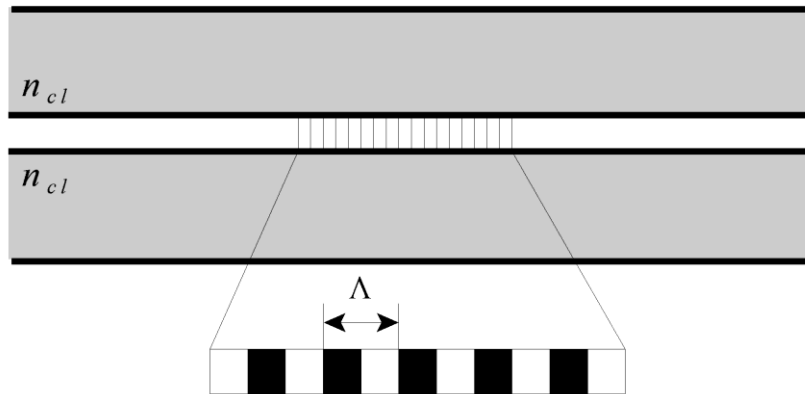


Figure 2.10. A fiber-Bragg grating in a single mode fiber.

Light incident on the modulated refractive index region, or grating, is reflected backward off the boundary regions between the high and low refractive index segments. When the incident light does not meet the Bragg condition

$$\lambda_B = 2n\Lambda \quad (2-17)$$

where λ_B is the free-space wavelength that meets the Bragg condition, n is the effective refractive index of the fiber core at the Bragg wavelength and Λ is the grating spacing, the light is reflected backward off each grating plane in an incoherent manner and adds destructively producing a weak reflected light signal. When light that meets the Bragg condition is incident on the fiber-Bragg grating it is reflected backward off each grating plane in a coherent fashion and adds constructively to produce a strong reflected light signal. Shown in figure 2.11 is the transmission versus wavelength for light incident on the fiber-Bragg Grating.

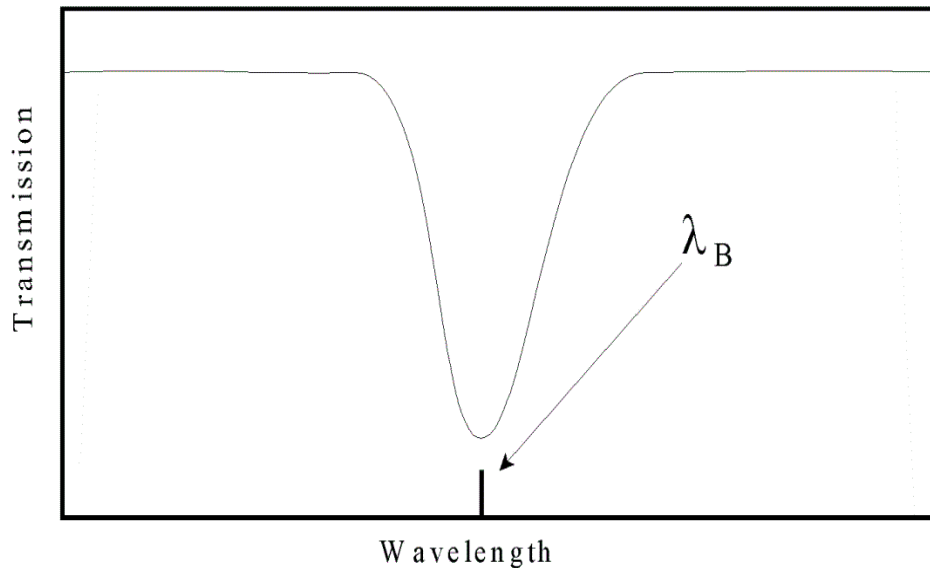


Figure 2.11. Transmission versus wavelength for light incident on a fiber-Bragg grating.

The Making of a Fiber-Bragg Grating

In 1978 it was accidentally discovered that an optical fiber may have its core refractive index altered. Hill and co-workers [30] introduced visible light (488nm) from an argon-ion laser into the core of a germanium-doped silica optical fiber. The light reflected off the cleaved end of the fiber and formed a standing wave. The refractive index at the locations of the high intensity regions of the standing wave were altered permanently. This light induced effect in an optical fiber was termed fiber photosensitivity. It was shown [31] that the magnitude of the refractive index change was proportional to the squared optical power of the argon-ion laser used to create the fiber-Bragg grating. This proportionality suggested a two-photon mechanism was responsible for the refractive index variation in the fiber. It was subsequently shown that relatively large magnitude refractive index variations could be obtained by using UV light of approximately 240nm wavelength to illuminate the fiber core. This wavelength is coincident with a well-known GeO defect in the germanium doped silica fiber [32].

A fiber-Bragg grating can be formed with a variety of techniques. The technique Hill and coworkers used (longitudinal standing wave) has a number of drawbacks. These include, Bragg resonance wavelengths limited to the wavelengths accessible with the argon-ion laser and relatively weak or small magnitude refractive index variations. Other techniques include the interferometric technique, point by point technique and the phase mask technique [29]. Figure 2.12 illustrates the phase mask technique.

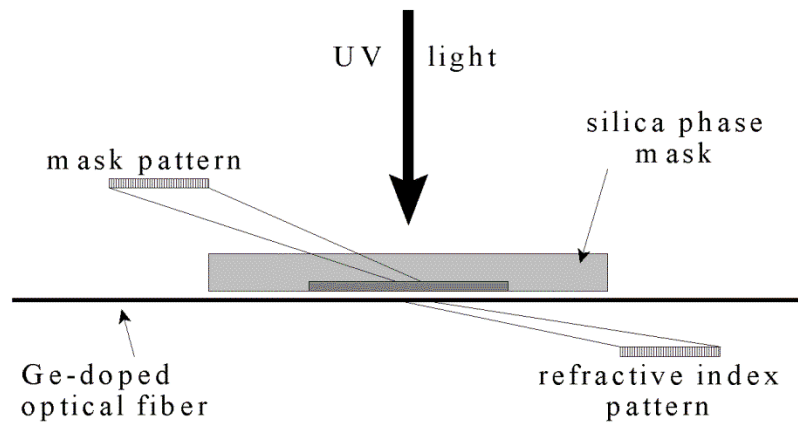


Figure 2.12. Illustration of phase mask technique for inscribing fiber-Bragg gratings.

As the phase masks are formed holographically or lithographically, complicated patterns may be written into the fiber-Bragg grating's refractive index profile. In addition, the Bragg wavelength is set by the phase mask pattern not the UV wavelength, so much greater flexibility is obtained over the Bragg wavelength.

Properties of Fiber-Bragg Gratings

The simplest case to treat analytically may be that of a sinusoidally varying constant amplitude refractive index profile where the refractive index as a function of length is given as

$$n(x) = n_0 + \Delta n \cdot \cos\left(\frac{2\pi \cdot x}{\Lambda}\right), \quad (2-18)$$

where n_0 is the average refractive index, Δn is the amplitude of the refractive index modulation and Λ is the grating spacing [29]. Using coupled mode theory [31] the reflectivity as a function of length and wavelength may be shown to be

$$R(L, \lambda) = \frac{\Omega^2 \sinh^2(sL)}{\Delta k^2 \sinh^2(sL) + s^2 \cosh^2(sL)}, \Omega^2 > \Delta k^2 \quad (2-19)$$

$$R(L, \lambda) = \frac{\Omega^2 \sin^2(isL)}{\Delta k^2 - \Omega^2 \cos^2(isL)}, \Omega^2 < \Delta k^2$$

where

$$\Omega = \frac{\pi \cdot \Delta n \cdot \eta(V)}{\lambda} \quad (2-20)$$

with $\eta(V) \approx 1 - 1/V^2$ is the coupling coefficient,

$$\Delta k = \frac{2\pi n_0}{\lambda} - \frac{\pi}{\lambda} \quad (2-21)$$

is the detuned wave vector and $s = (\Omega^2 - \Delta k^2)^{1/2}$. The bandwidth (full width at half maximum) is given approximately by

$$\Delta\lambda = \lambda_B \alpha \sqrt{\frac{\Delta n^2}{2n_0} + \frac{1^2}{N}} \quad (2-22)$$

where $\alpha \sim 1$ for fiber-Bragg gratings with reflectivity near 100% and N is the number of grating planes. Figure 2.13 shows a typical grating reflectivity as a function of wavelength close to $\lambda_B = 1530\text{nm}$.

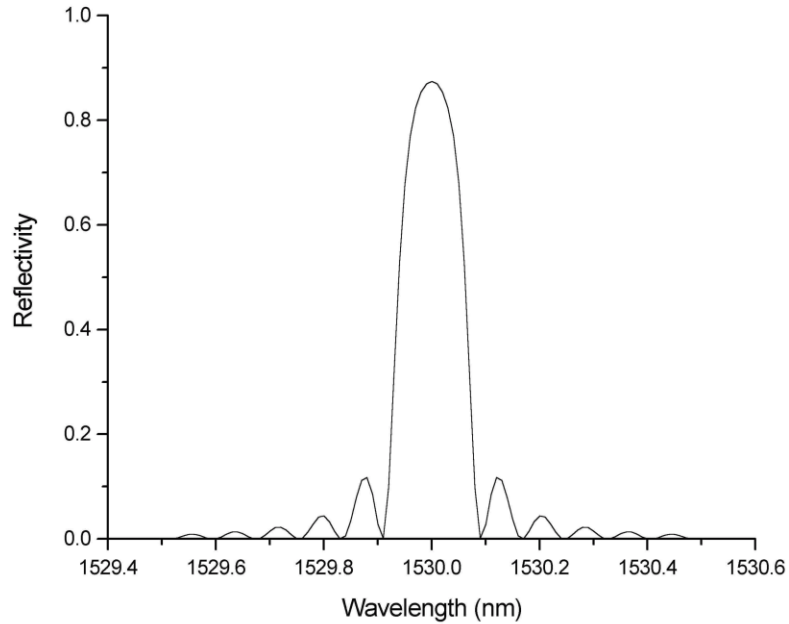


Figure 2.13. Reflectivity versus wavelength for a 1 cm length grating.

FBG Effect on the Spontaneous Emission Rate of a Two-level Atom

Given Equation 2-13 above for the total spontaneous emission rate of an atom, and assuming A_c is much less than A_f and Φ_c is much less than 4π (which is the case for our system), also assuming that most of the ions reside deep within the grating (grating surface effects can be neglected), and that ions deep within the grating are completely

shielded from the vacuum field mode perpendicular to the grating planes, the fractional change in the spontaneous emission rate is given by

$$\frac{A_{fs} - A_T}{A_{fs}} = \frac{\Phi_c}{4\pi}. \quad (2-23)$$

As will be shown in Chapter IV, the ratio of solid angle perturbed by our fiber-Bragg grating that the erbium atom's experience to 4π is $\sim 1\%$. This result indicates that for an ideal two-level atom interacting with the vacuum-field environment perturbed by our fiber-Bragg grating a 1% maximum variation in ionic lifetime may be expected.

CHAPTER III

REAL SYSTEM: ERBIUM-GLASS CASE STUDY

The material system employed in the experimental attempt to measure a modification in the ionic spontaneous emission rate (Chapter IV) is the erbium-doped silica core of a single-mode optical fiber. In this chapter, experiments measuring the material parameters of the system are described along with the results.

This description begins with the level structure, absorption, unperturbed lifetime [33 - 38], doping concentration and fiber characteristics of the material system as reported elsewhere in the literature or specified by the company that makes the fiber. Following this is a description of fluorescence line narrowing (FLN) experiments and the spectroscopic results obtained at liquid nitrogen and liquid helium temperatures. A holeburning experiment to measure the homogeneous width and the unperturbed longitudinal dephasing time (T_1) of the relevant optical transition (${}^4I_{13/2}$ - ${}^4I_{15/2}$) at liquid helium temperature follows.

A discussion of the physics relevant to the low-temperature homogeneous linewidth and the intra/inter-Stark-level energy migration seen in the FLN results is presented. Finally, an estimate of the on/off fiber-Bragg grating resonance variation in the ionic spontaneous emission rate of the real system is given.

Material Parameters

The energy level structure of erbium in an erbium-doped silica fiber is not the structure of the simple two-level atom considered in the previous chapter. The erbium-doped silica is a complex solid state material. Complications result from the fact that the wavefunctions of the electrons in the erbium atoms are altered from their free atomic form by the presence of the host (silica + co-dopants) material [39]. Figure 3.1 shows some of the energy levels of an erbium-doped glass fiber similar to that reported in reference [40].

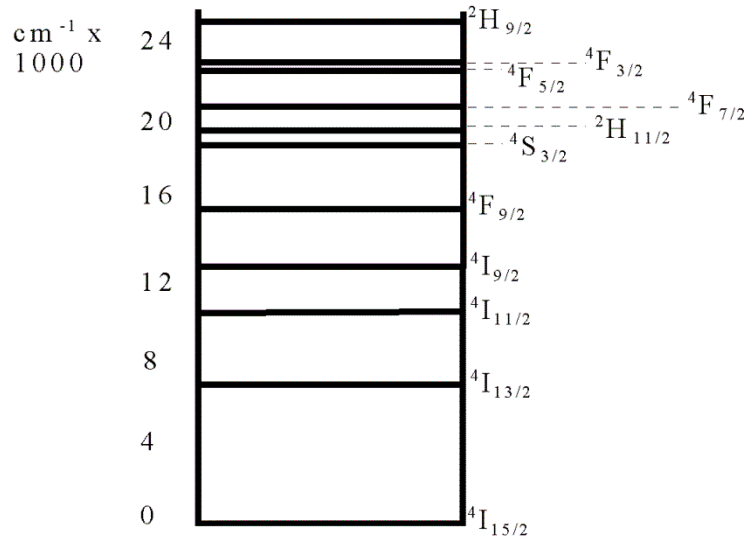


Figure 3.1. Energy level structure of an erbium-doped glass fiber.

Figure 3.2 (A) shows an expanded energy-level diagram for the ${}^4I_{13/2} - {}^4I_{15/2}$ transition as reported in reference [33]. Figure 3.2 (B) shows a typical pumping scheme (upward arrow represents pump energy) for the fluorescence line narrowing measurements.

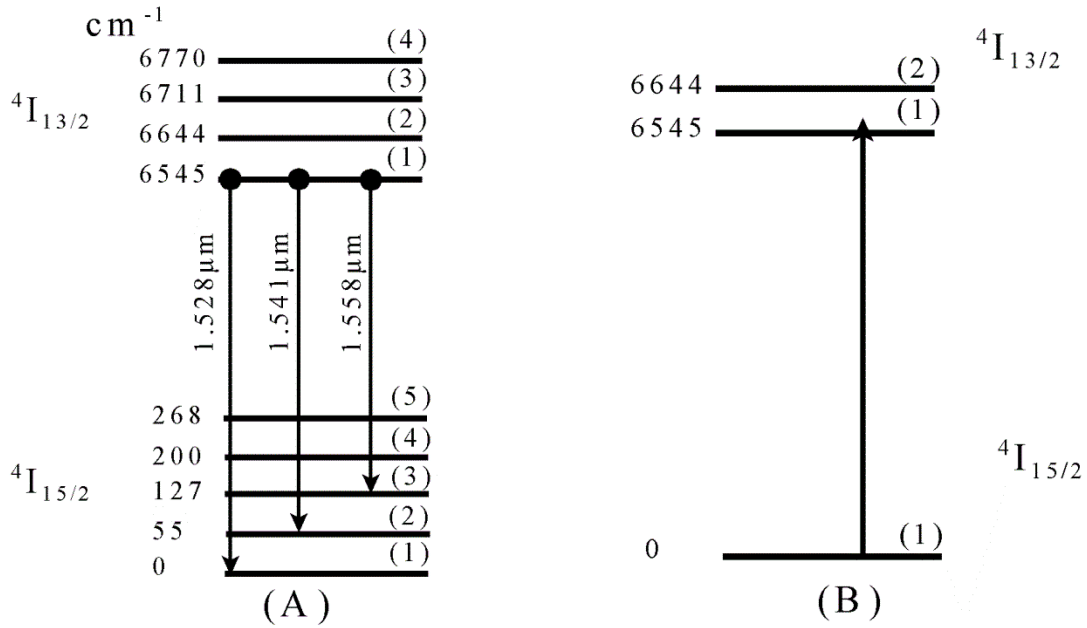


Figure 3.2. Energy-level Stark splittings of the ${}^4I_{13/2} - {}^4I_{15/2}$ transition.

The ${}^4I_{13/2}(1) - {}^4I_{15/2}(1)$ transition is the transition of interest concerning the experimental attempt to measure a change in the erbium's spontaneous emission rate. As can be seen in figure 3.2 there are five Stark levels in the lower state manifold and four Stark levels in the upper state manifold. The erbium-doped fiber reported in reference [33] is similar to our erbium-doped fiber; however differences (erbium concentration, co-dopants, co-dopant concentration, contaminants, etc.) may exist.

The erbium-doped optical fiber employed in our material system is made by INO in Canada and is their product number ER 103. The optical absorption of our fiber sample is specified to be 4 ± 1 dB/m at room temperature and a wavelength of 1531nm, while at the experimental temperature of 4.5 K the absorption is measured to be 8.6 ± 0.2 dB/m at 1530nm. The free space or unperturbed lifetime (T_1), for a similar fiber, is reported in the

literature as 10 ms while the homogeneous width is given as an upper limit of ≤ 13 GHz at 4.2 K [33]. The erbium doping concentration is 900 ± 300 ppm. The erbium-doped fiber has a core with a diameter of 4 ± 1 μm , a numerical aperture of 0.16 ± 0.02 , and is single transverse mode throughout the wavelength range of interest with a cutoff wavelength of 900 ± 50 nm.

The FLN Sample

The erbium-doped fiber sample is 20 cm in length and fusion spliced (with fixed V-groove splicer) at each end onto SMF-28 optical fiber made by Corning Incorporated. Fusion splicing is a process whereby two optical fibers are connected using an electrical arc to fuse the fibers together in such a way as to produce a connection with relatively little optical loss. That is, light incident upon the fusion splice is transmitted further down the fiber core with little scattering loss. The SMF-28 fiber has a core diameter of 8.2 μm , a cut-off wavelength of 1260 nm, a numerical aperture of 0.14 and an effective refractive index of 1.4682 at 1550 nm. The schematic of the erbium-doped-fiber/SMF-28-fiber sample is shown in figure 3.3. The black circles shown in figure 3.3 represent the erbium ions. The erbium ions are contained only in the core and are concentrated in the center of the core with approximately 50% of the ions within 1 μm of the core's axis.

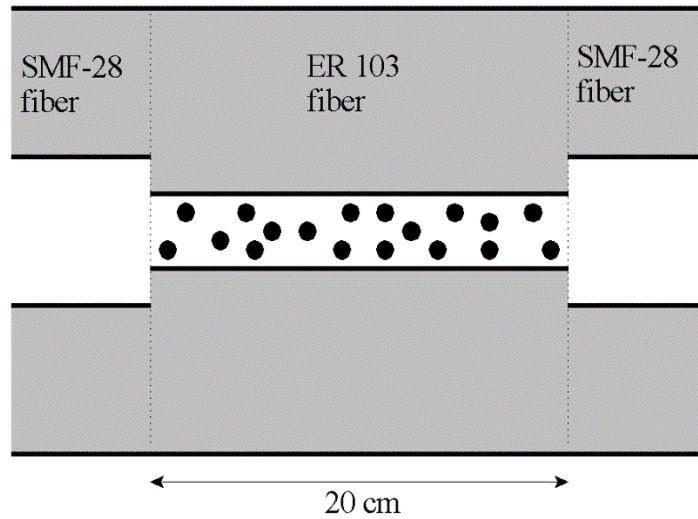


Figure 3.3. Schematic of fiber sample: Gray area: fiber cladding. White area: fiber core.

The schematic in figure 3.3 is inconsistent with the real sample in that erbium ions diffuse out of the ER 103 fiber and into the SMF-28 fiber during the fusion splicing process. In addition, low loss fusion splicing usually occurs when the fibers to be spliced have closely matched core diameters, numerical apertures and core refractive indices. Our fibers (ER 103 and SMF-28) do not have closely matched parameters. Consequently, the nature of the sample in the regions of the fusion splices is largely unknown [41].

The Cryostat

The sample is immersed in either liquid helium or liquid nitrogen in a modified immersion cryostat made by Janis Research Company model RD and serial number 205. Figure 3.4 shows a simplified schematic of the cryostat. As can be seen in figure 3.4 the

sample is located in the liquid helium reservoir which can be filled with liquid helium (LHe) or liquid nitrogen (LN₂).

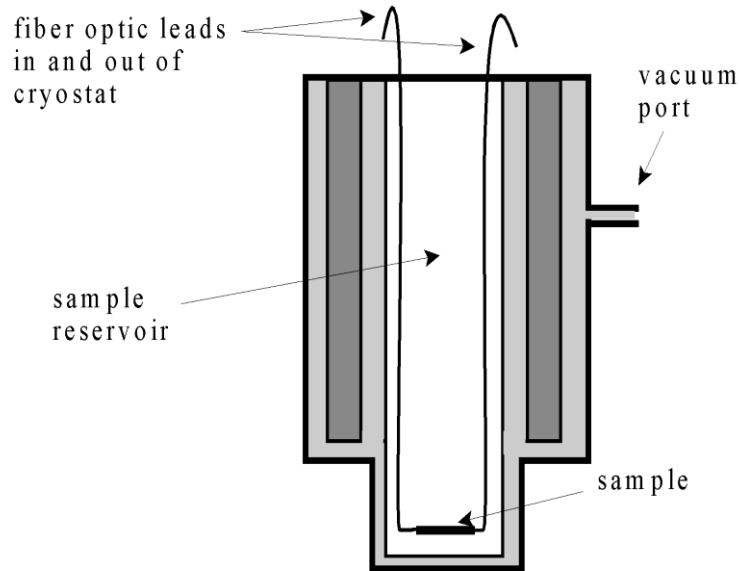


Figure 3.4. Simplified schematic of cryostat: Light gray areas are the vacuum jacket, dark gray areas are the liquid nitrogen reservoir and the central white area is the LHe reservoir where the sample is located.

A temperature sensor DT-470-CU-13 from LakeShore Cryotronics, Inc. is mounted on an aluminum platform (not shown in figure 3.4) a few inches above the sample and is connected to a LakeShore Cryotronics temperature controller model DRC 80C for monitoring the temperature in the LHe reservoir. A vacuum is induced (≤ 10 mTorr) in the vacuum jacket of the cryostat by attaching a Varian Inc. mechanical pump model SD-200 to the vacuum port. The fiber optic leads (the SMF-28 fiber fusion spliced onto the

sample) are directed out the top of the cryostat through sealed ports and sent to the laser and the optical detection system.

Typically, when the sample is to be immersed in liquid helium or liquid nitrogen, the cool down procedure starts by mechanically pumping the vacuum jacket to around 10 mTorr in pressure then introducing liquid nitrogen into the liquid nitrogen reservoir. Following this, either liquid nitrogen is introduced immediately into the sample reservoir or, after a period of time (so that the temperature in the sample reservoir is approximately 77K), liquid helium is introduced into the sample reservoir.

Fluorescence Line Narrowing Experiment: Experimental Setup

The experimental setup employed in the fluorescence line narrowing measurements [42-44] is shown in figure 3.5. The components indicated in box a) are F1 a focal length $f = 5$ cm lens, F2 a $f = 50$ cm lens and F3 a $f = 10$ cm lens which is ~ 10 cm away from the entrance slits of the spectrometer. M indicates an IR coated flat mirror, F1 and F2 are separated by 55 cm and all lenses are IR coated. The components in box a) are employed in order to match the light beam's geometry at the entrance slits to the acceptance geometry of the spectrometer. The coupler is a fiber to free space light coupler from Thorlabs model number F220FC that produces a single-mode beam with approximately a 1 mm beam diameter (FWHM). The laser is a single-mode fiber-coupled tuneable external-cavity diode laser model number 6200 from New Focus. The laser has a maximum output power of approximately 4 mW (fiber coupled), a wavelength range of \sim

1508 nm to 1583 nm and a specified linewidth of less than 5 MHz over 5 seconds. The Wavemeter is model number WA-1000 from Burleigh.

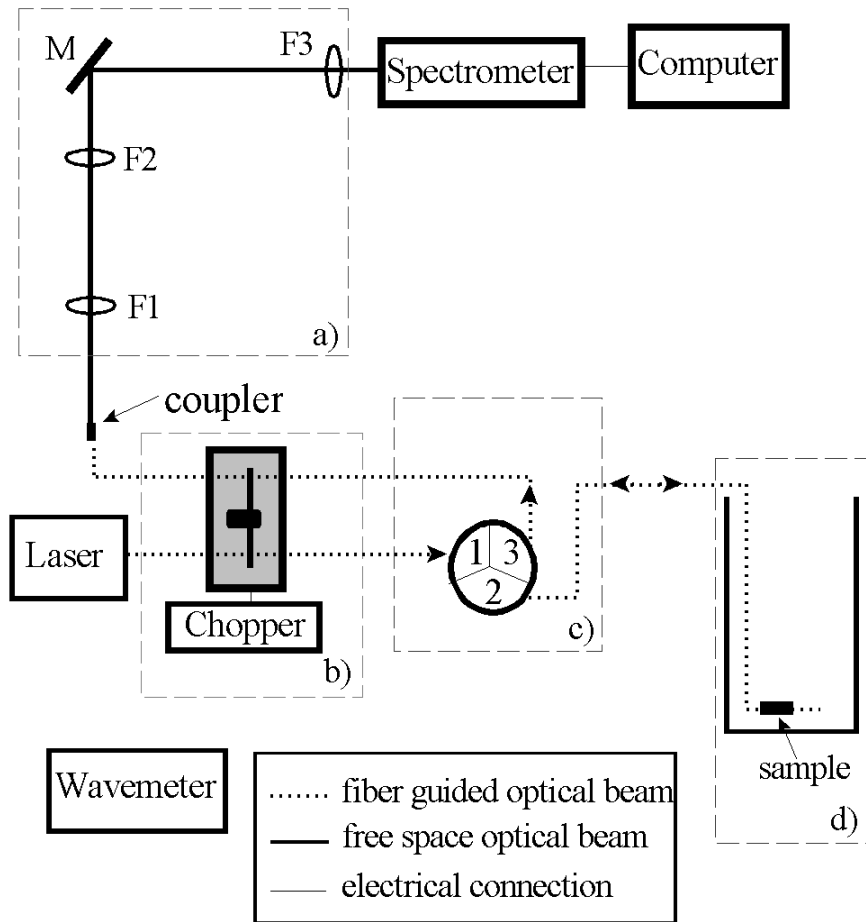


Figure 3.5. Experimental setup for fluorescence line narrowing measurements.

The components indicated in box b) are an optical chopper and controller model number SR 540 from Stanford Research Systems. In box c) a fiber-coupled optical circulator model number CIRD 1550 from Telelight Communication Inc. is shown. Box d) shows the cryostat and sample. The spectrometer is model number HR 460 from Instruments S.A. Group with a focal length of 460 mm and an $f/5.3$ aperture and unity magnification

at the exit slits. The grating used in the spectrometer to spectrally disperse the fluorescence is a 76 x 76 mm 600 line/mm grating blazed at 1.5 μm . Employed along with the spectrometer is a liquid nitrogen cooled IR (InGaAs) detector model number DSS-IGA020L from Electro-Optical Systems Inc. and a DataScan 2 module from Instruments S.A. Group that interfaces the detector, spectrometer and computer. The computer is a 120 MHz PC with Microsoft's Windows 95 operating system and Instrument S.A. Group's Spectromax software. The IR detector is operated at $\sim 77\text{K}$ with a spectral range of approximately 1.0 - 1.7 μm . In the mode that the detector is used it has a responsivity of 2.0×10^{10} V/W, a bandwidth of DC-150Hz and a NEP of 1×10^{-15} W/Hz^{1/2}. The chopper wheel is non-commercial and was constructed in the University of Oregon's Student Machine Shop with the guidance of Chris Johnson and David Senkovich. A representation of the wheel is shown in figure 3.6. The representation of the chopper wheel shown in figure 3.6 is meant to convey the general pattern. The actual chopper wheel has 24 holes in an outer pattern and 24 holes in an inner pattern. The outer hole pattern has an on/off duty cycle of $\sim 50\%$ while the inner hole pattern has an on/off duty cycle of $\sim 36\%$. The outer and inner hole patterns allow light to pass in a mutually exclusive manner. That is, when light is allowed through the inner hole pattern (for example, to excite the sample) light is not allowed to pass through the outer hole pattern (for example, to detect fluorescence from the sample).

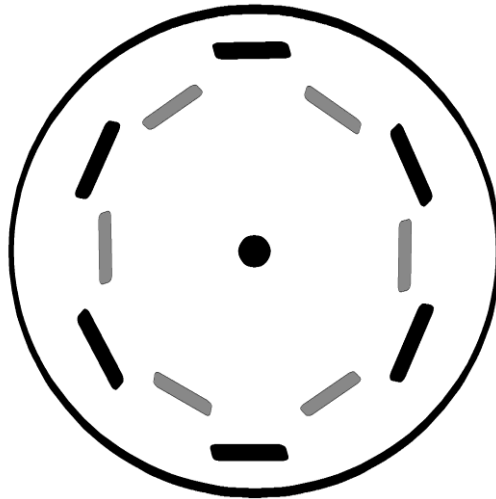


Figure 3.6. Representation of optical chopper wheel.

In this manner, light collected and sent to the spectrometer is assured to be fluorescence from the sample and not excitation light.

As figure 3.5 indicates, the light from the laser is directed to the inner hole pattern of the optical chopper. The light is then guided through the optical circulator and on to the sample. The circulator is a directional device that directs light from port 1 to port 2 and light from port 2 to port 3 with little loss (~ 0.5 dB). Large loss (~ 45 dB) occurs for light directed from port 2 to 1 and port 3 to 2 and ~ 65 dB loss from port 1 to 3. The light is fiber coupled for most of this path except at the optical chopper wheel where it is free space coupled (so as to pass through the chopper wheel) by a fiber-U-bench from Thorlabs Inc. model number FB211-FC. Fluorescence from the excited erbium ions that is guided by the fiber is then directed back to circulator port 2 where the circulator sends it out of port 3 with little loss and on to the outer hole pattern of the optical chopper wheel. Most of this optical path is also fiber coupled except, as mentioned above, directly

at the chopper wheel where it is again free space coupled by another fiber-U-bench. A fiber to free space coupler is then used to make the fluorescence light incident on the spectrometer-matching optics indicated in box a) of figure 3.5. The fluorescence is then coupled into the spectrometer. A schematic of the spectrometer is given in figure 3.7.

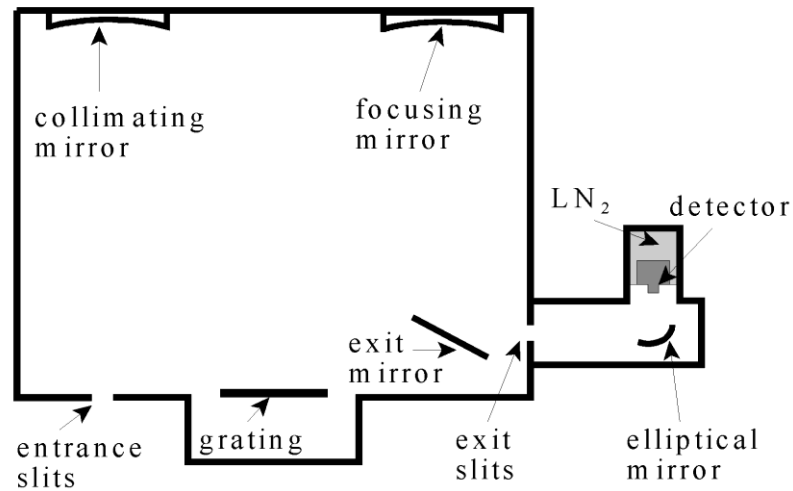


Figure 3.7. Schematic of spectrometer and detector apparatus.

The optical path through the spectrometer begins with the fluorescence, focused by F3 to a spot, at the entrance slits. The beam then diverges until it reaches the collimating mirror where it is collimated and made incident upon the grating. The grating angularly separates the fluorescence as a function of its spectral content and sends the spectrally diffused fluorescence on to the focusing mirror. The focusing mirror directs the light to the flat exit mirror where it is then sent to a spot on the exit slits. The fluorescence light

then diverges to the elliptical mirror where it is sent to the active area of the detector with a magnification of 1/6.

The Fluorescence Line Narrowing Data

The laser is wavelength calibrated with the Wavemeter to an absolute wavelength accuracy of ~ 0.005 nm. The excitation light from the laser is chopped with a frequency of ~ 1800 Hz. The time averaged excitation power is ~ 12 nW. The wavelength scan increment is 0.1 nm with an integration time of 0.5 sec. while the instrumental resolution is measured to be 0.2 nm. Figures 3.8 through 3.23 show the fluorescence power collected from the liquid-helium-cooled sample and sent to the spectrometer versus wavelength for the given excitation wavelengths. Figure 3.24 shows the liquid helium sample's fluorescence power versus wavelength for all excitation wavelengths superimposed.

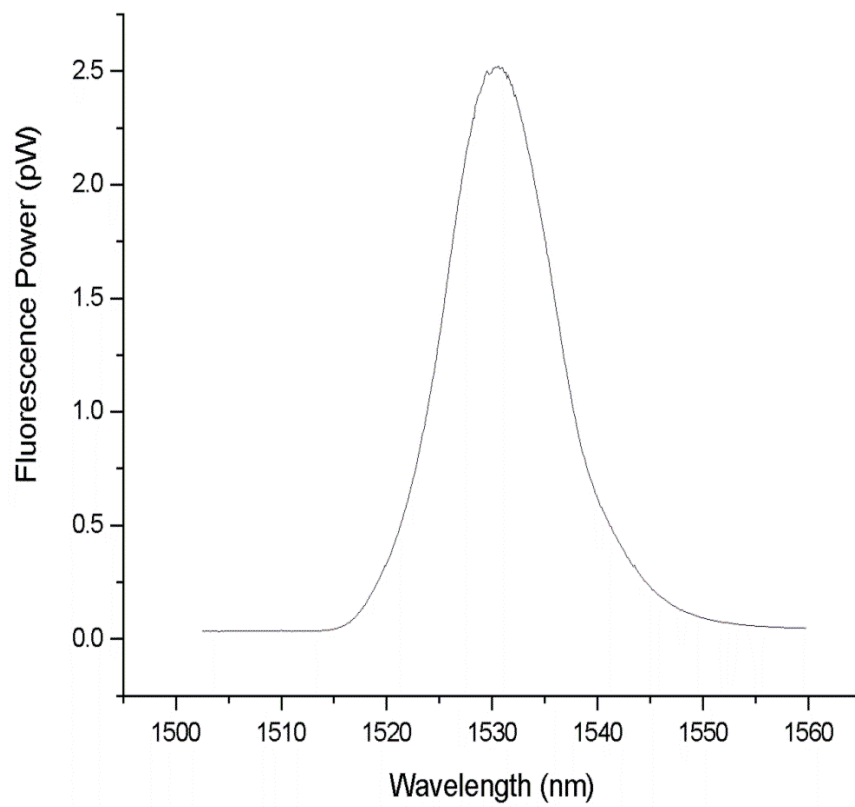


Figure 3.8. Fluorescence power versus wavelength for 1510.00 nm excitation.

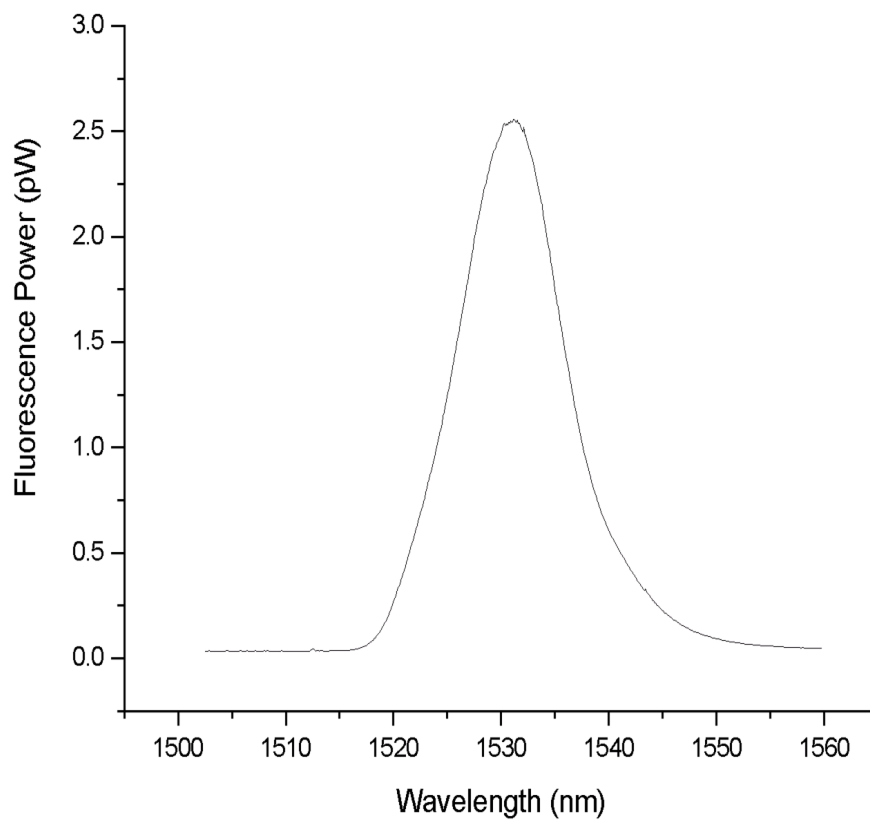


Figure 3.9. Fluorescence power versus wavelength for 1512.50 nm excitation.

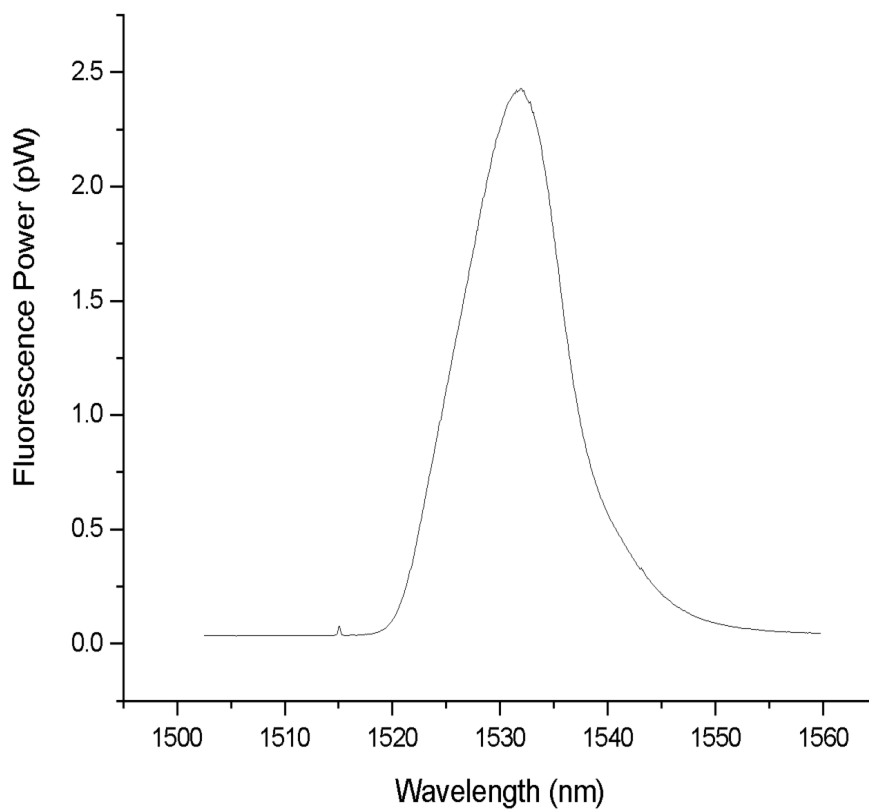


Figure 3.10. Fluorescence power versus wavelength for 1515.00 nm excitation.

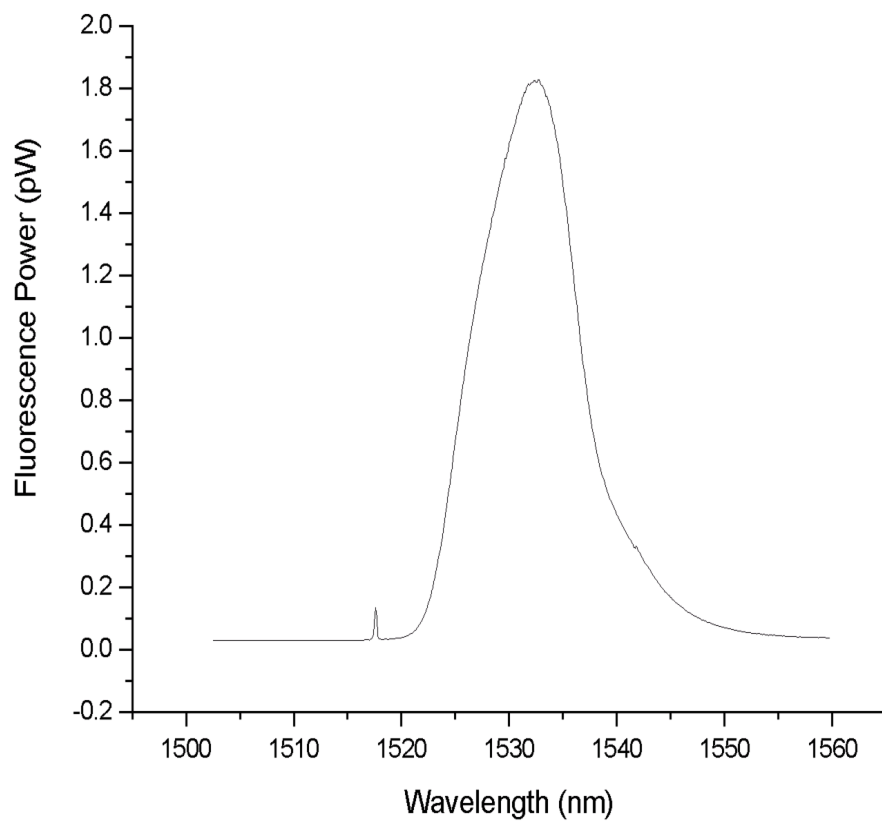


Figure 3.11. Fluorescence power versus wavelength for 1517.50 nm excitation.

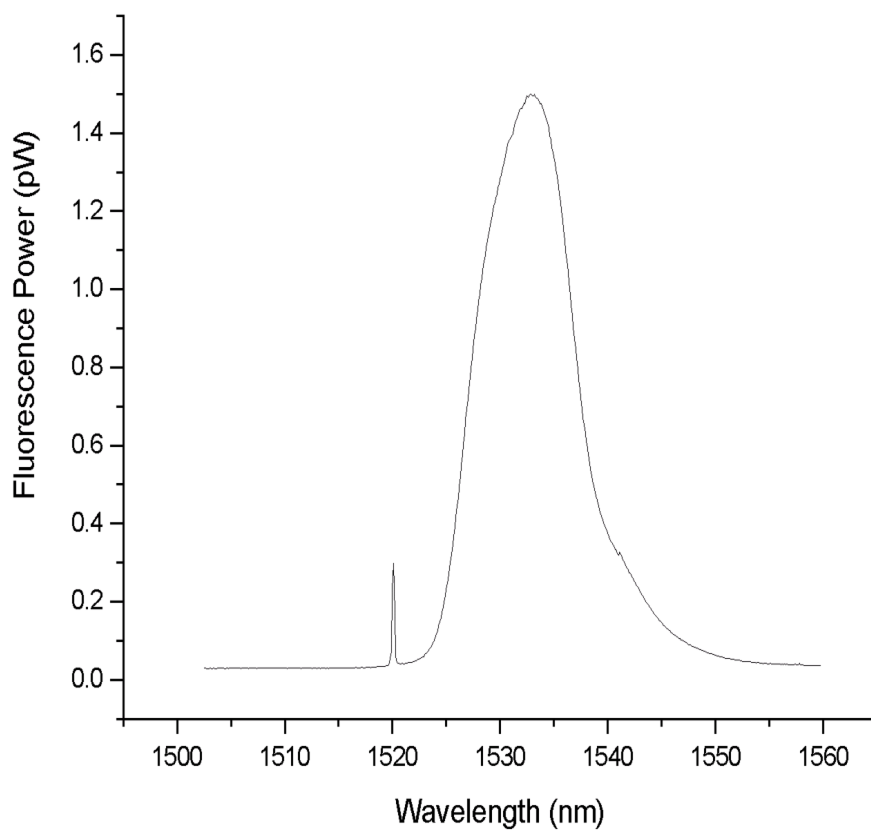


Figure 3.12. Fluorescence power versus wavelength for 1520.00 nm excitation.

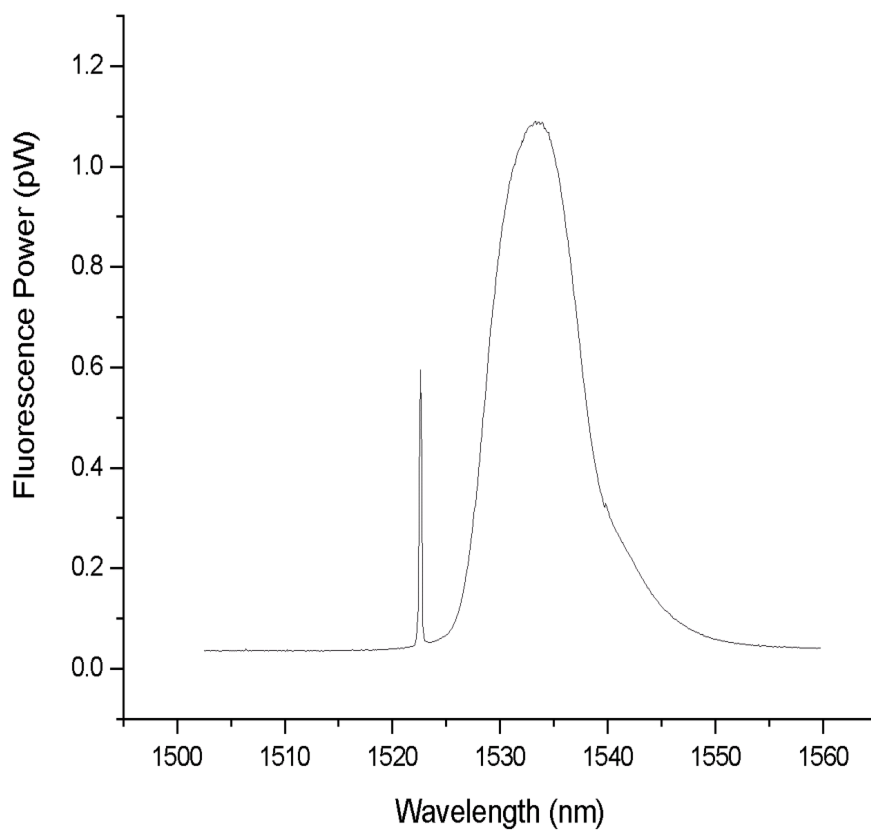


Figure 3.13. Fluorescence power versus wavelength for 1522.50 nm excitation.

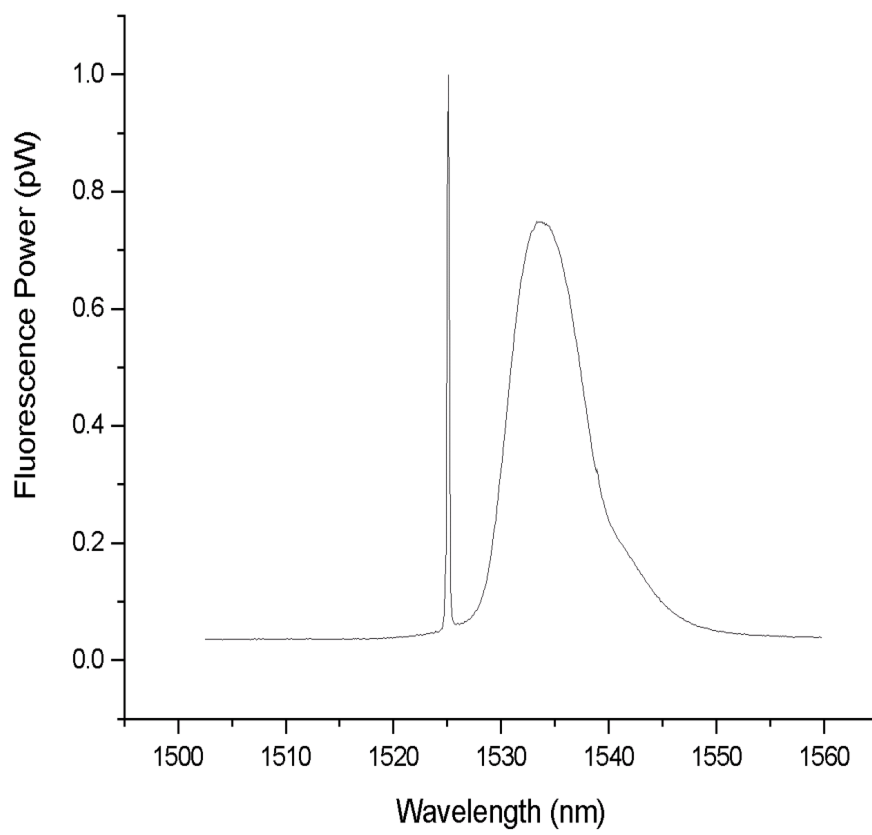


Figure 3.14. Fluorescence power versus wavelength for 1525.00 nm excitation.

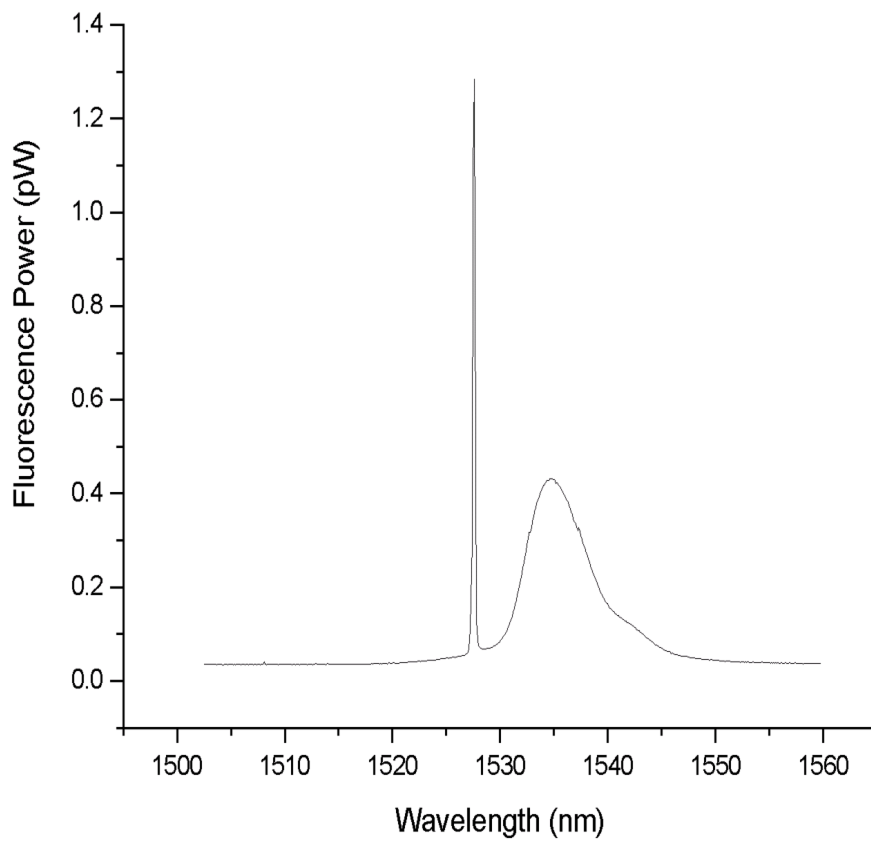


Figure 3.15. Fluorescence power versus wavelength for 1527.50 nm excitation.

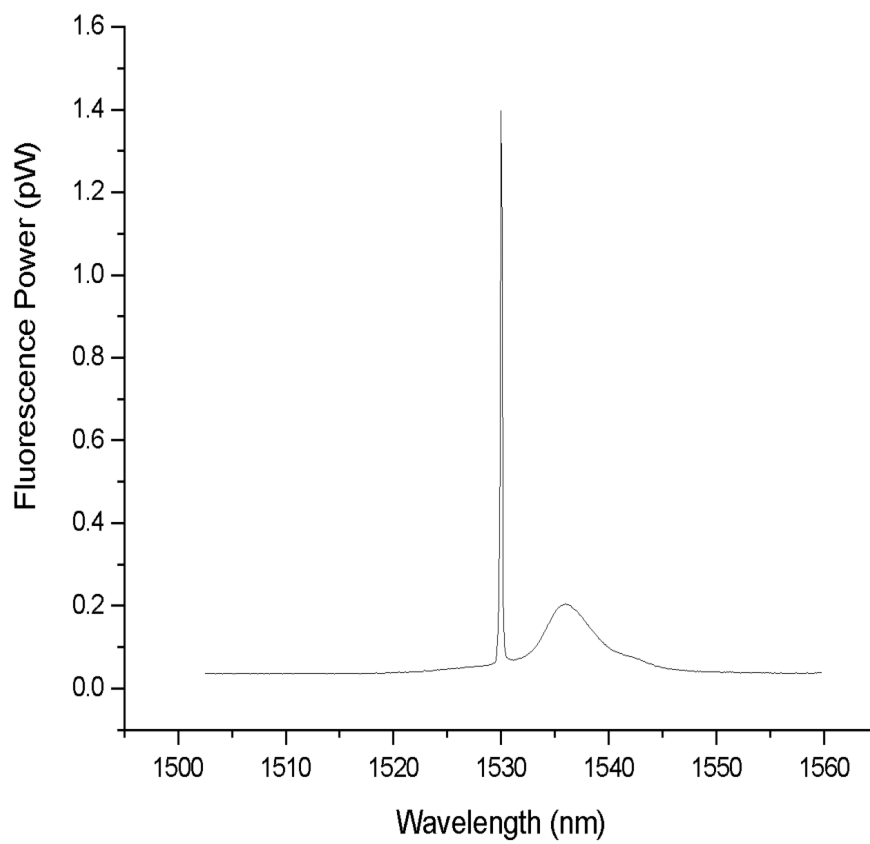


Figure 3.16. Fluorescence power versus wavelength for 1530.00 nm excitation.

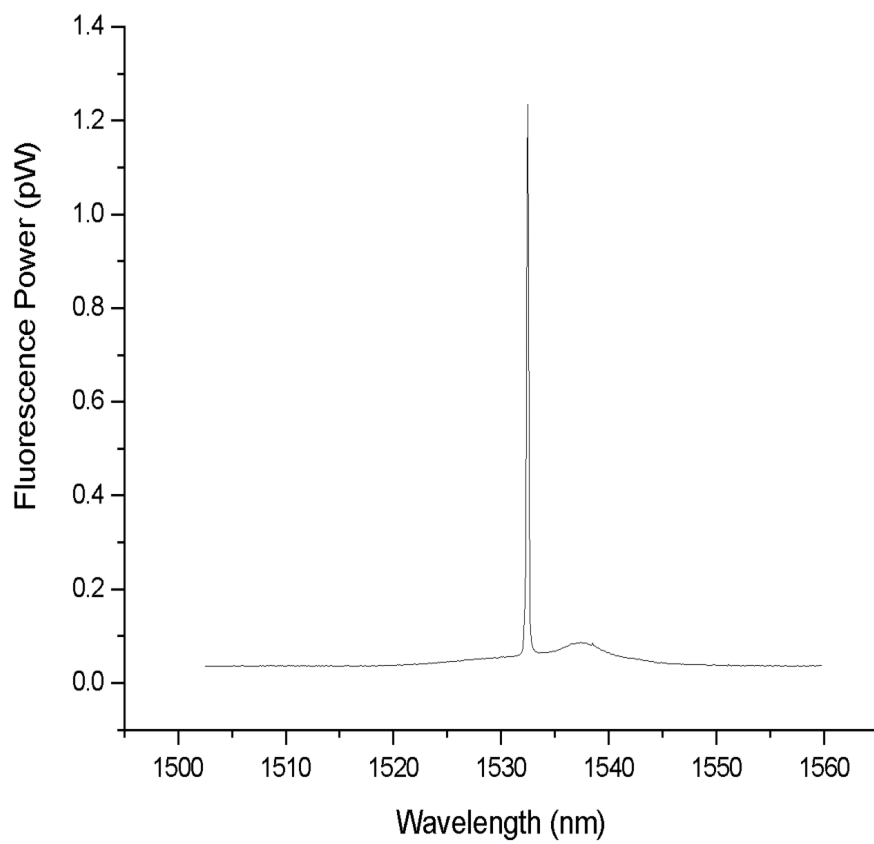


Figure 3.17. Fluorescence power versus wavelength for 1532.50 nm excitation.

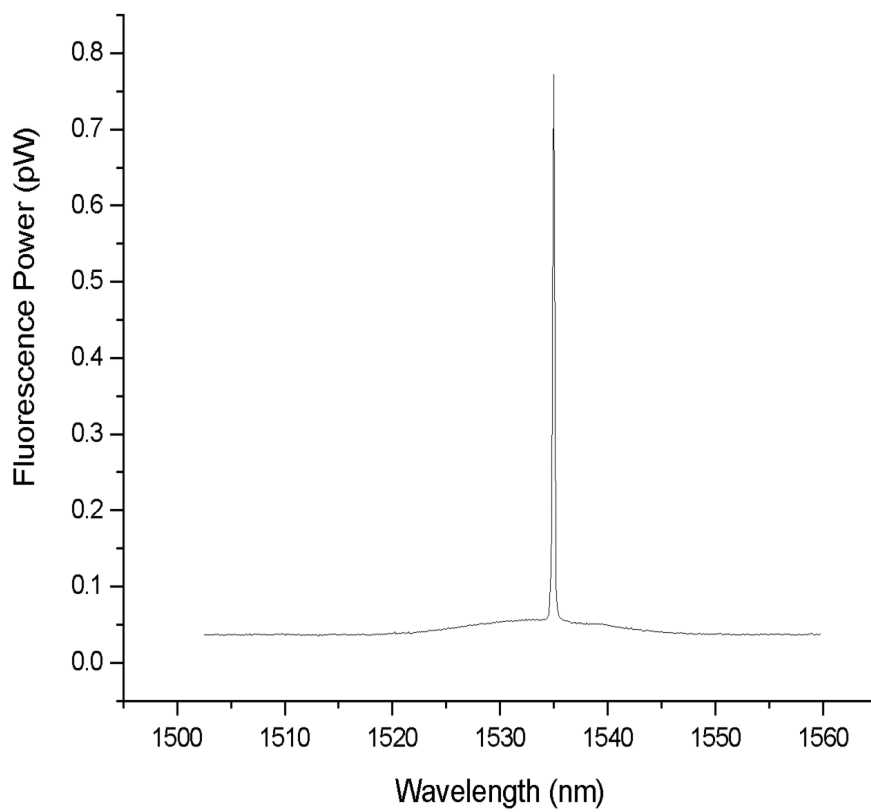


Figure 3.18. Fluorescence power versus wavelength for 1535.00 nm excitation.

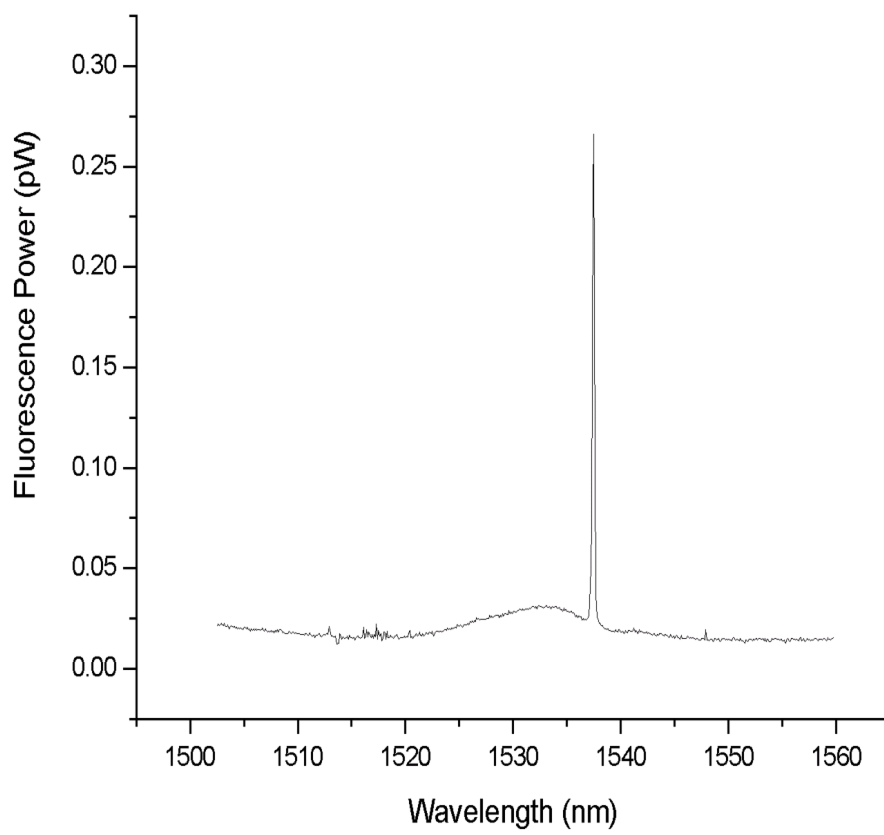


Figure 3.19. Fluorescence power versus wavelength for 1537.50 nm excitation.

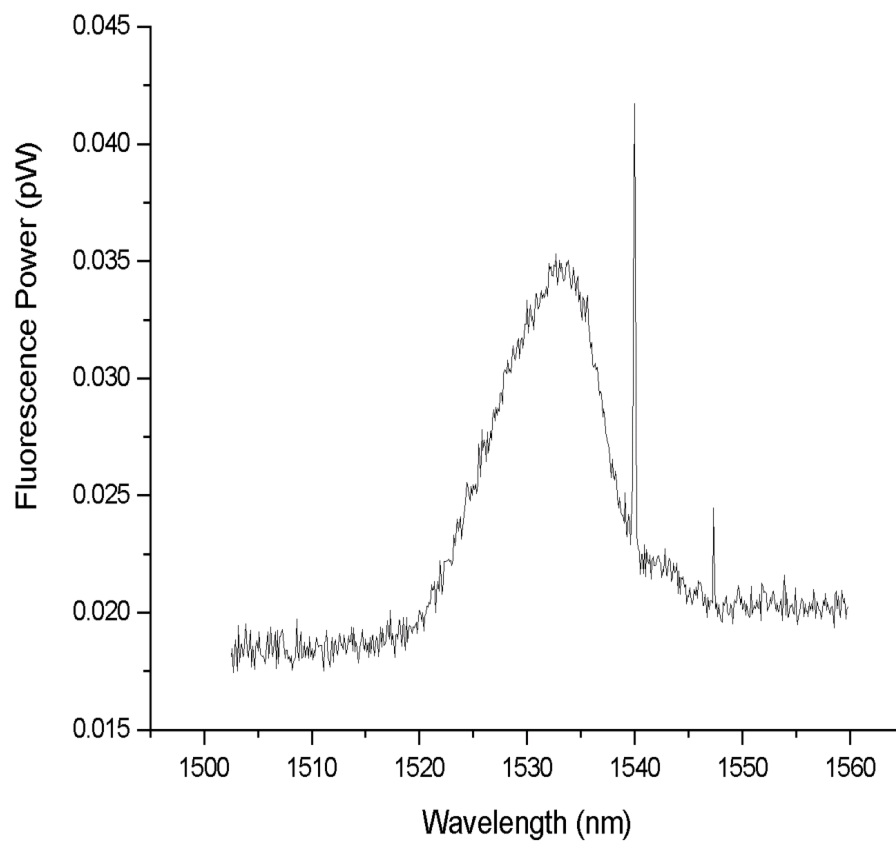


Figure 3.20. Fluorescence power versus wavelength for 1540.00 nm excitation.

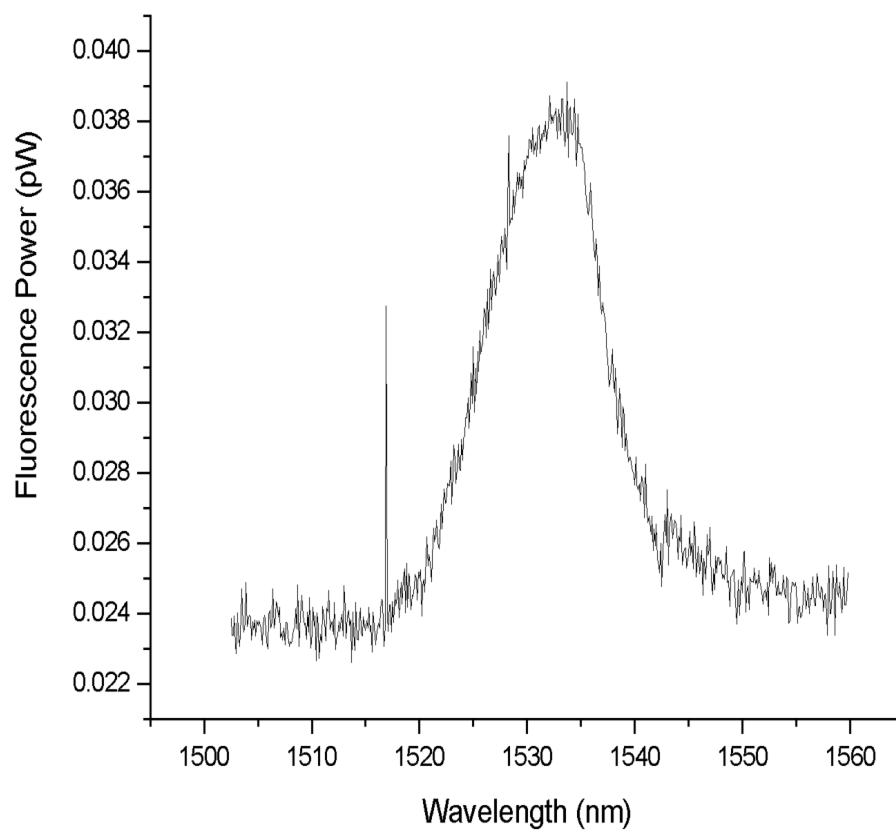


Figure 3.21. Fluorescence power versus wavelength for 1542.50 nm excitation.

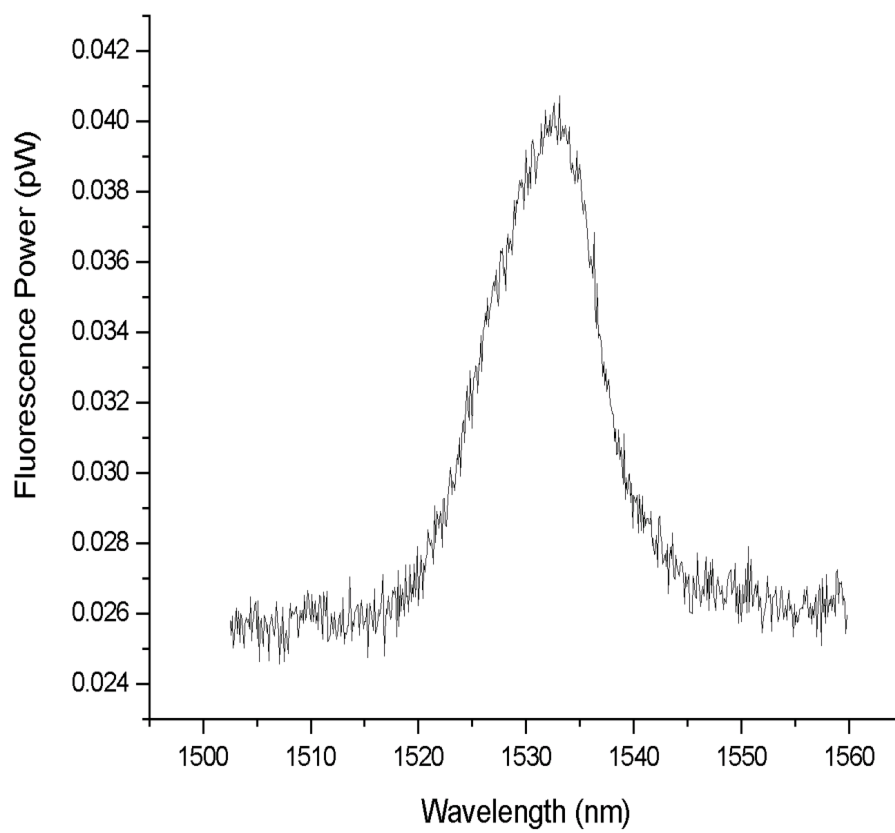


Figure 3.22. Fluorescence power versus wavelength for 1545.00 nm excitation.

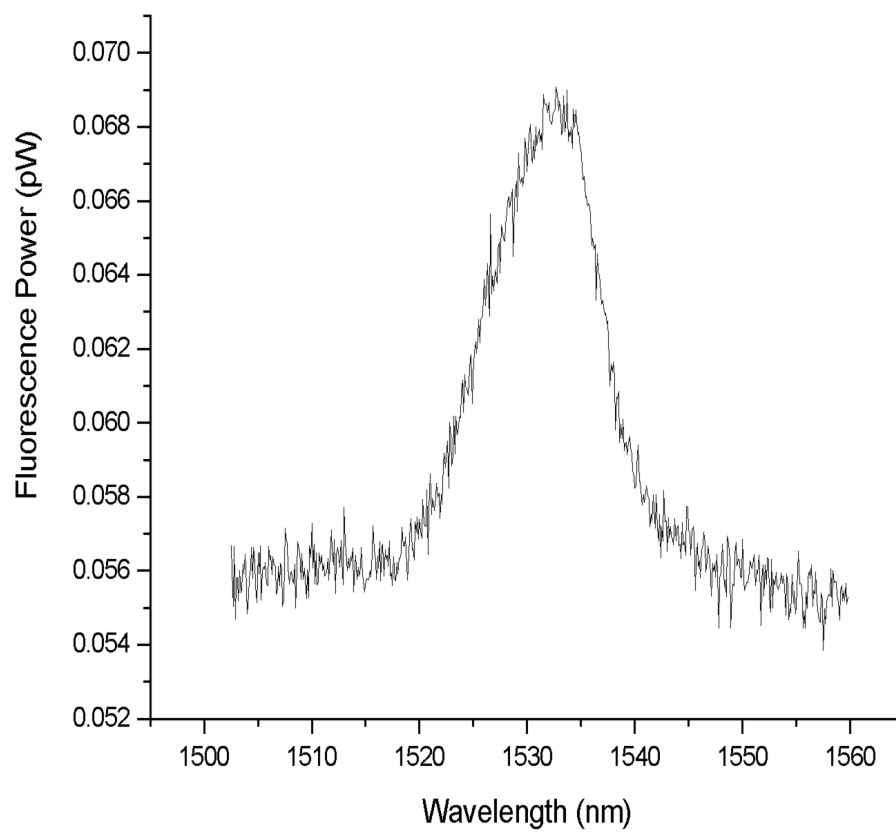


Figure 3.23. Fluorescence power versus wavelength for 1547.50 nm excitation.

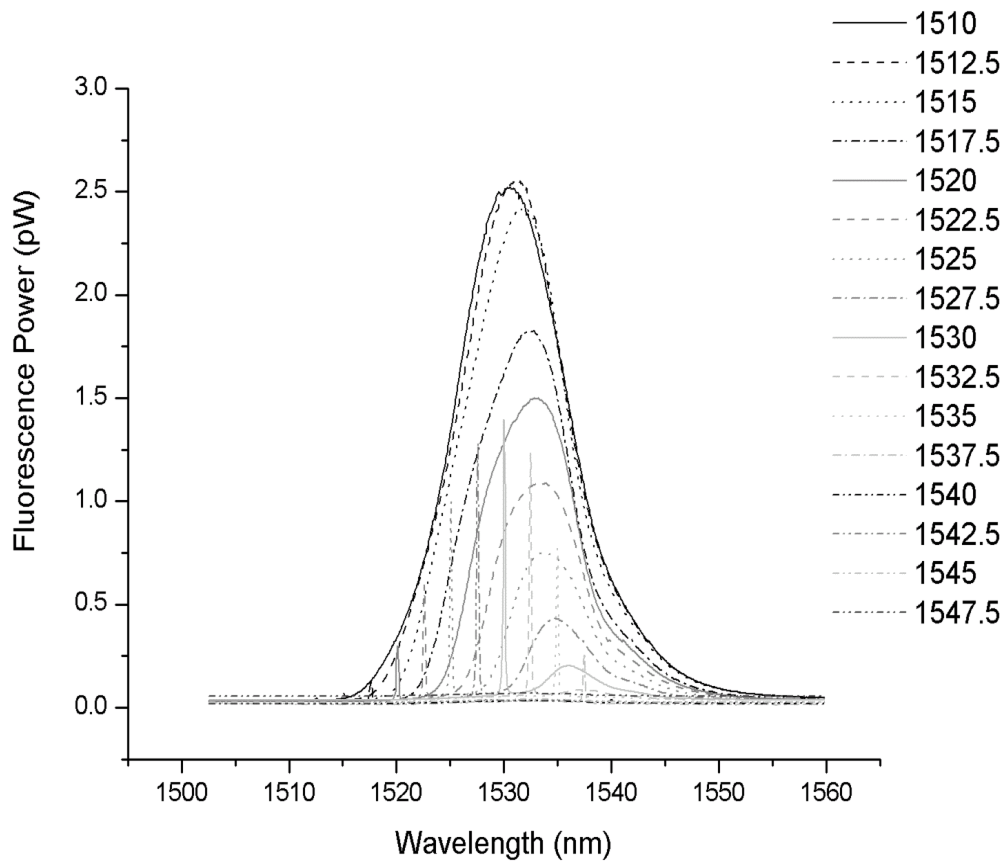


Figure 3.24. Fluorescence power versus wavelength for all excitation wavelengths.

Figure 3.25 shows the maximum optical power of the narrow feature (that spectroscopic feature corresponding to the direct optical transition ${}^4I_{13/2}(1)$ to ${}^4I_{15/2}(1)$) as a function of the spectroscopically narrow feature's wavelength.

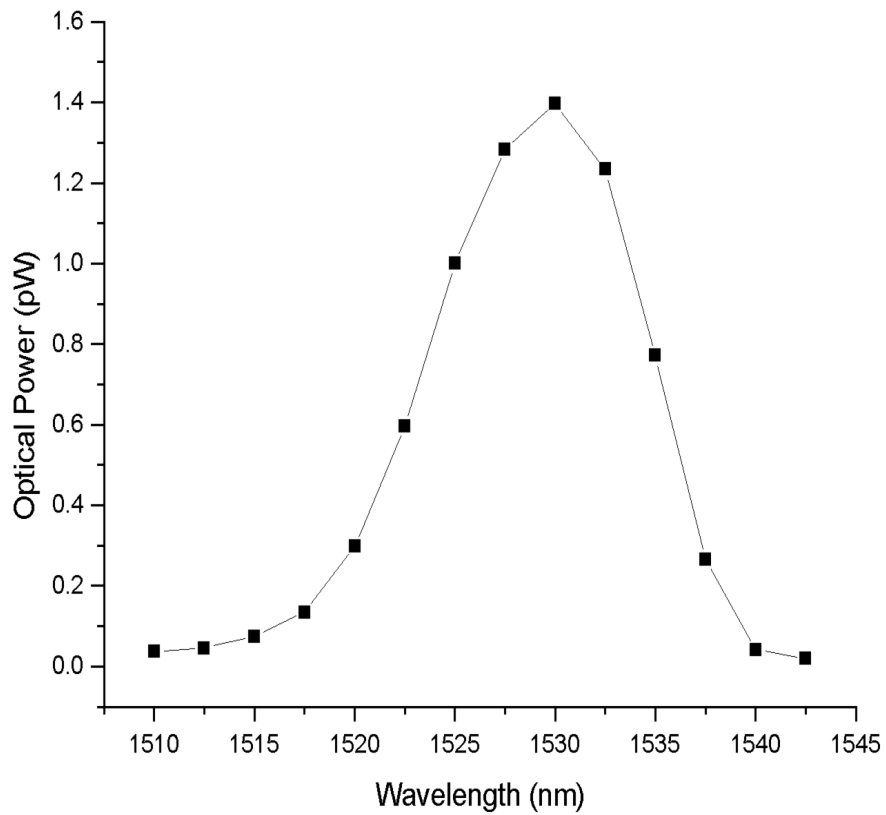


Figure 3.25. Power of direct transition fluorescence peak versus peak wavelength.

Figure 3.26 is a plot of the wavelength difference between the spectrally broad feature and the spectrally narrow feature or the excitation wavelength.

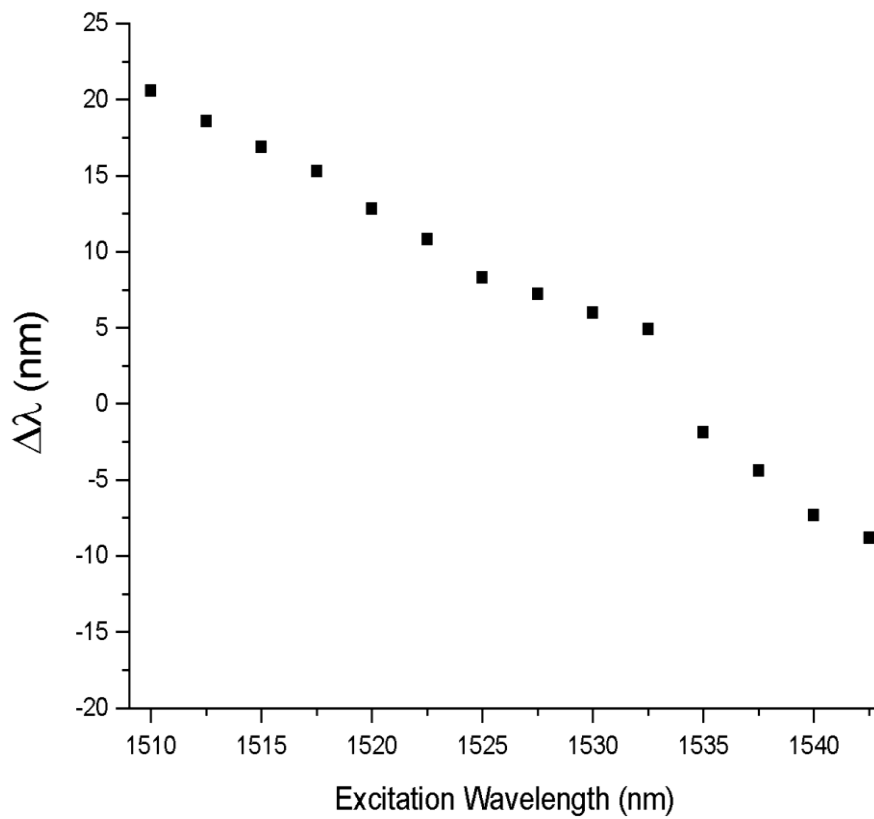


Figure 3.26. Wavelength difference between broad and narrow spectral features.

Figure 3.27 is a plot of the area of the broad spectral feature as a function of excitation wavelength.

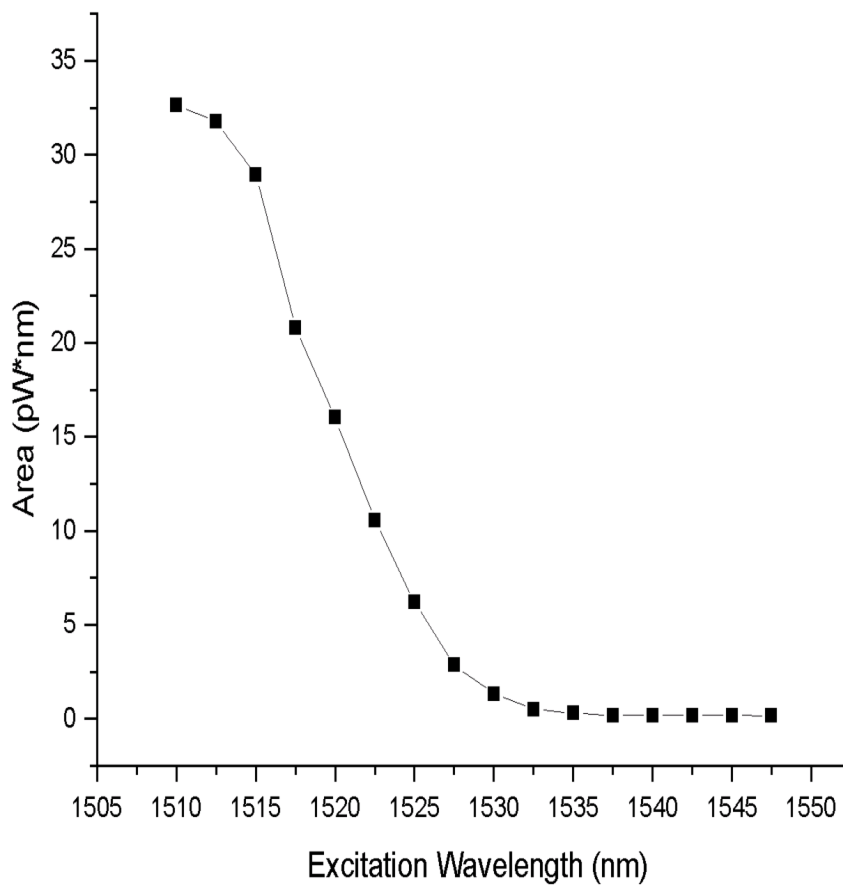


Figure 3.27. Area of broad spectral feature versus excitation wavelength.

Figures 3.28 through 3.34 show the fluorescence power collected from the liquid nitrogen cooled sample and sent to the spectrometer versus wavelength for the given excitation wavelengths. The excitation light from the laser is chopped with a frequency of ~ 1900 Hz. The time-averaged excitation power is ~ 10 nW. The wavelength scan increment is 0.1 nm with an integration time of 0.5 sec. while the instrumental resolution is measured to be 0.2 nm. Figure 3.35 shows the liquid nitrogen cooled sample's fluorescence power versus wavelength for all excitation wavelengths superimposed.

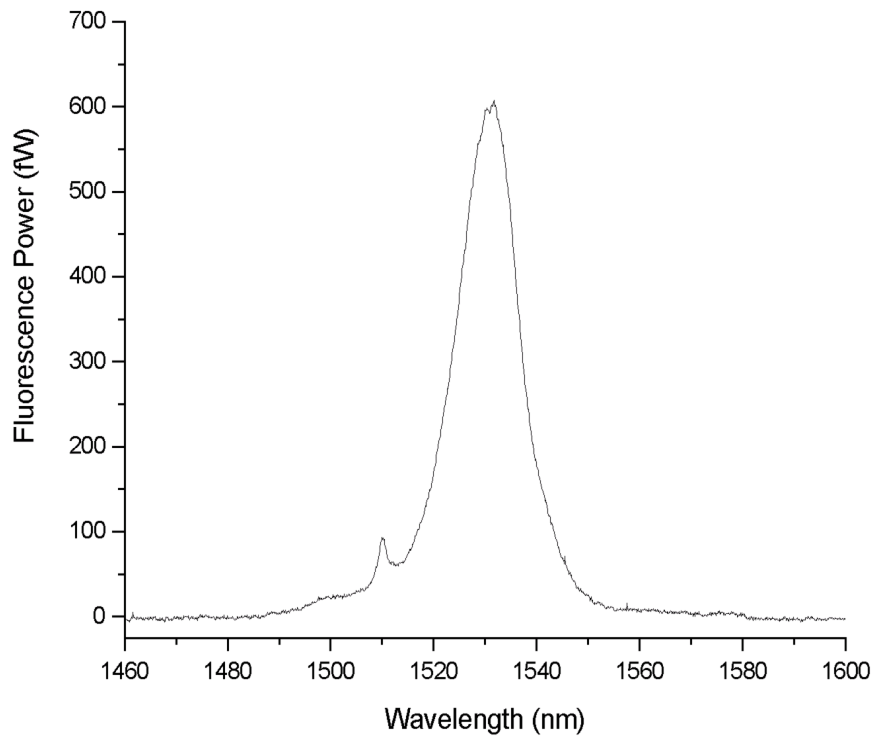


Figure 3.28. Fluorescence power versus wavelength for 1510.00 nm excitation.

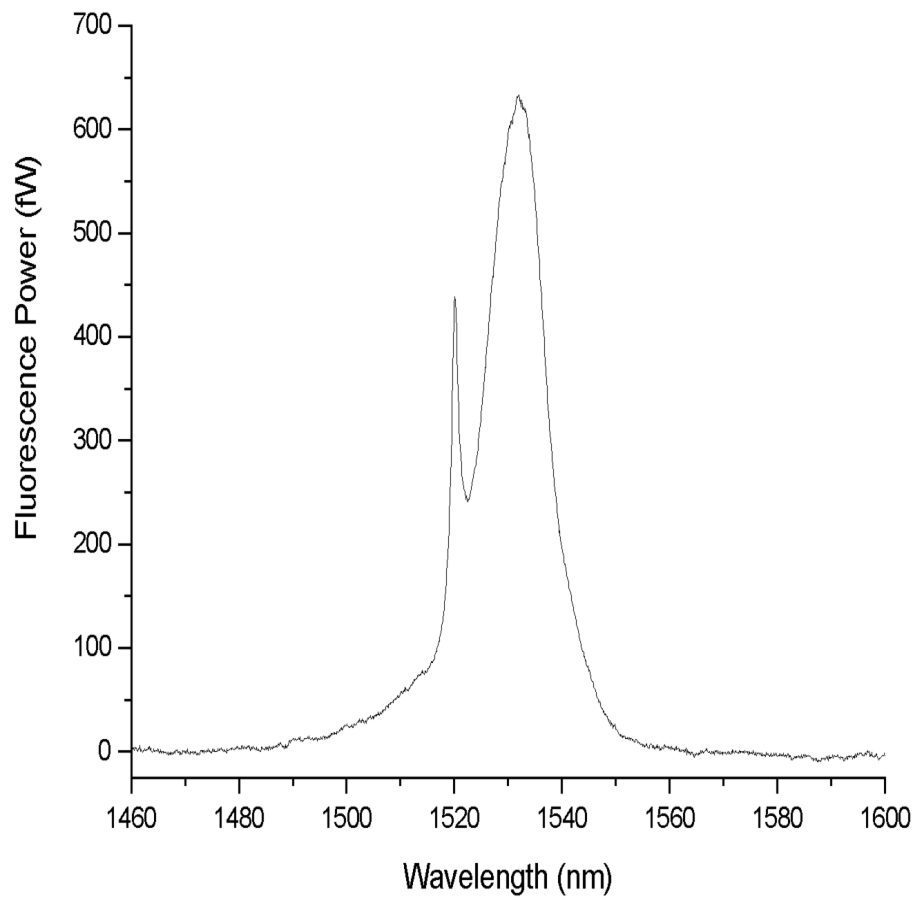


Figure 3.29 Fluorescence power versus wavelength for 1520.00 nm excitation.

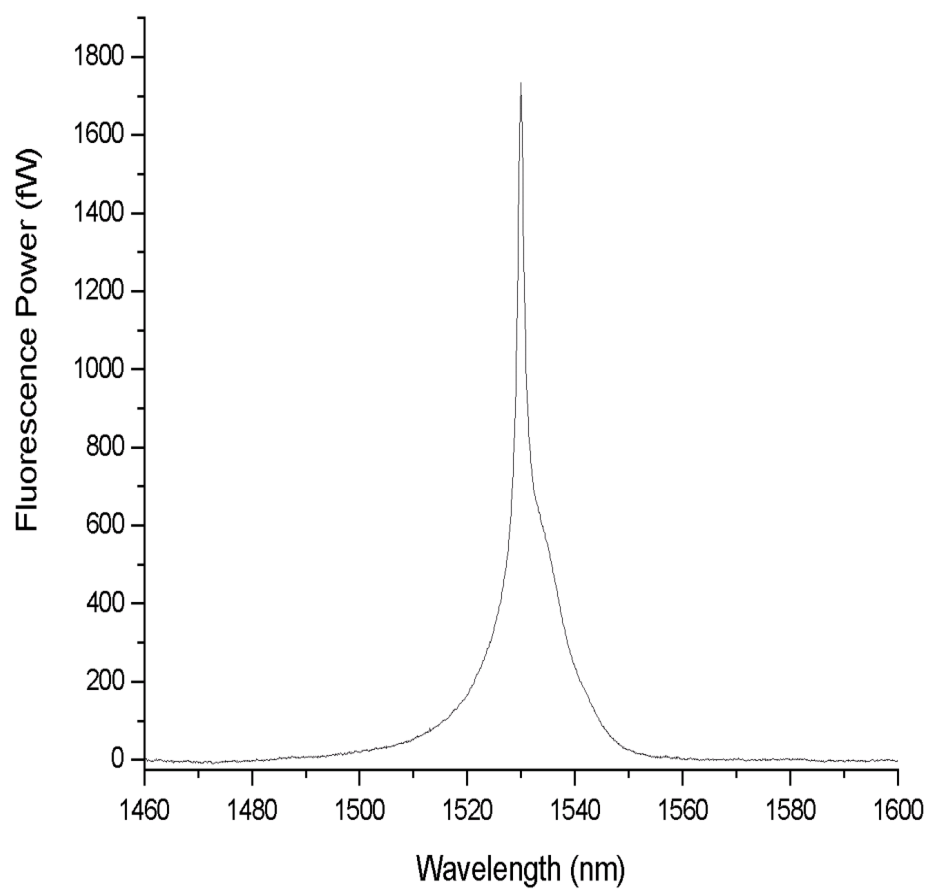


Figure 3.30 Fluorescence power versus wavelength for 1530.00 nm excitation.

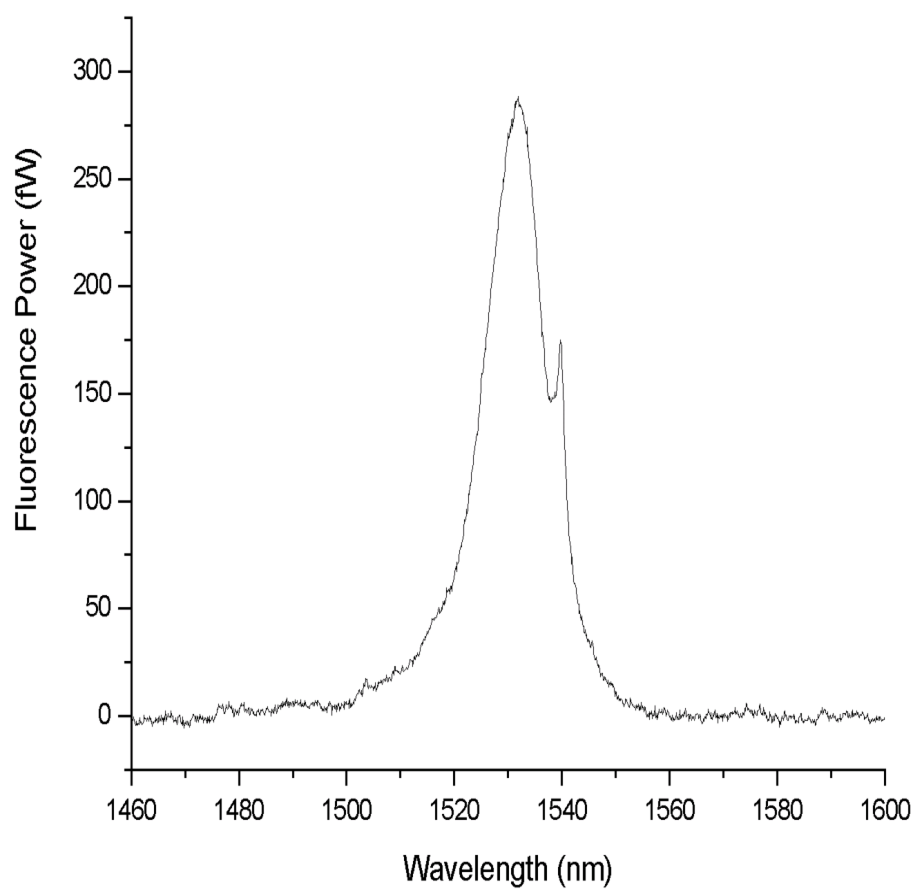


Figure 3.31 Fluorescence power versus wavelength for 1540.00 nm excitation.

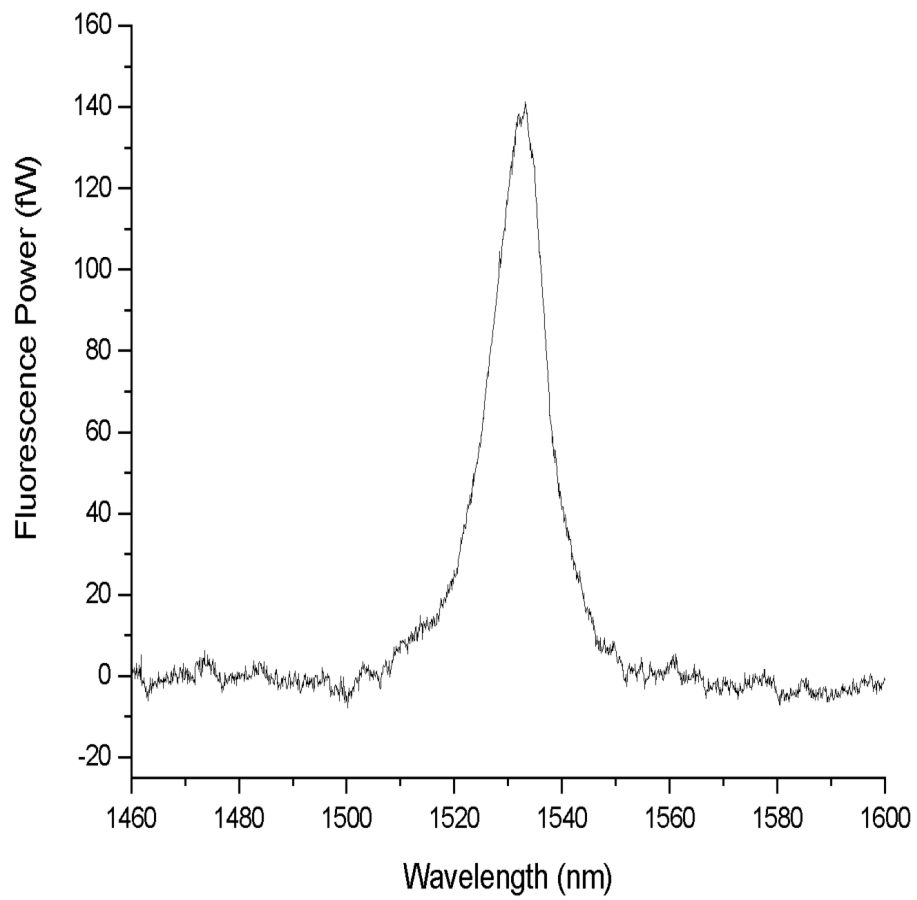


Figure 3.32 Fluorescence power versus wavelength for 1550.00 nm excitation.

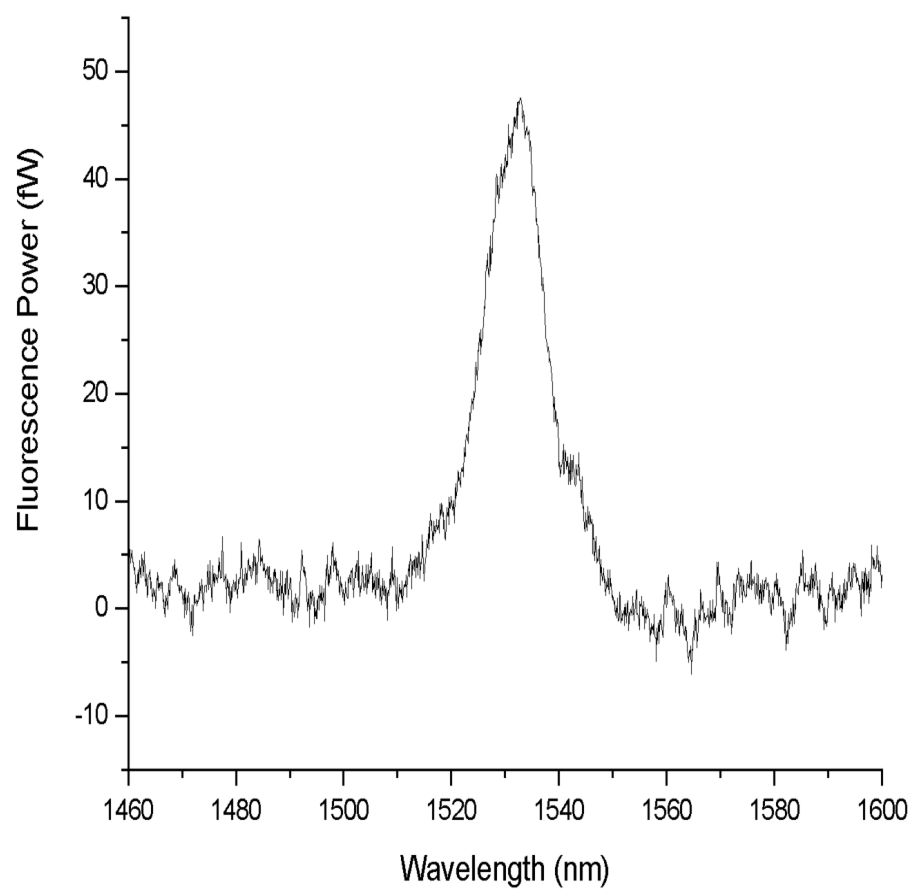


Figure 3.33 Fluorescence power versus wavelength for 1560.00 nm excitation.

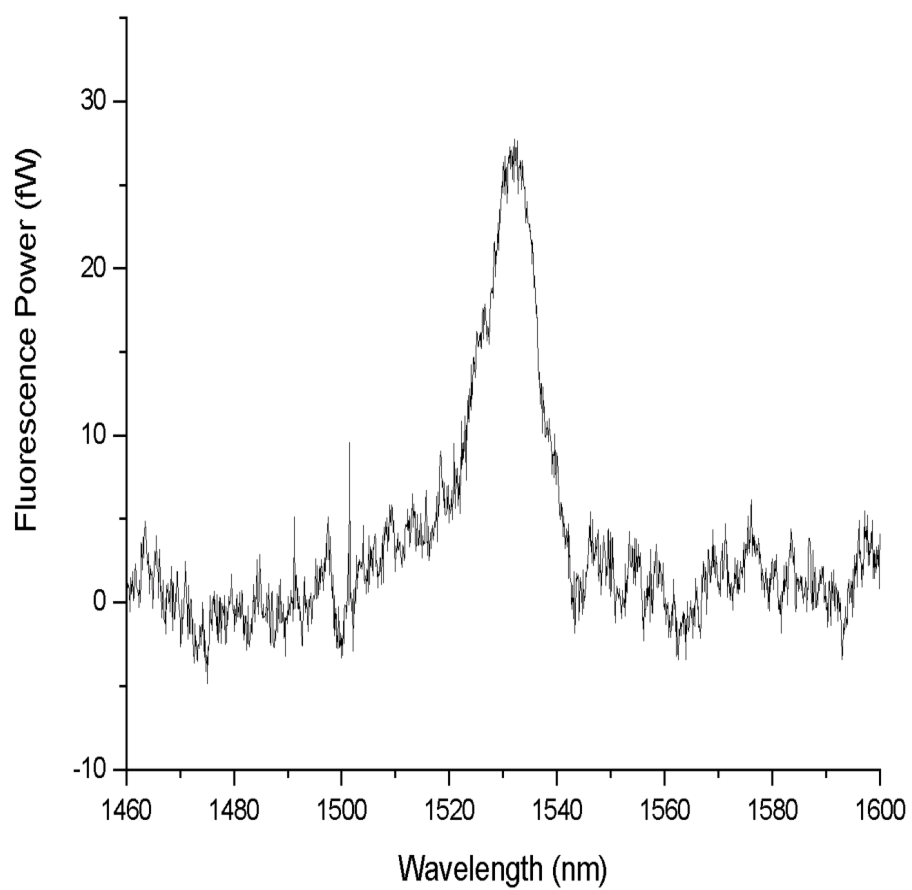


Figure 3.34 Fluorescence power versus wavelength for 1570.00 nm excitation.

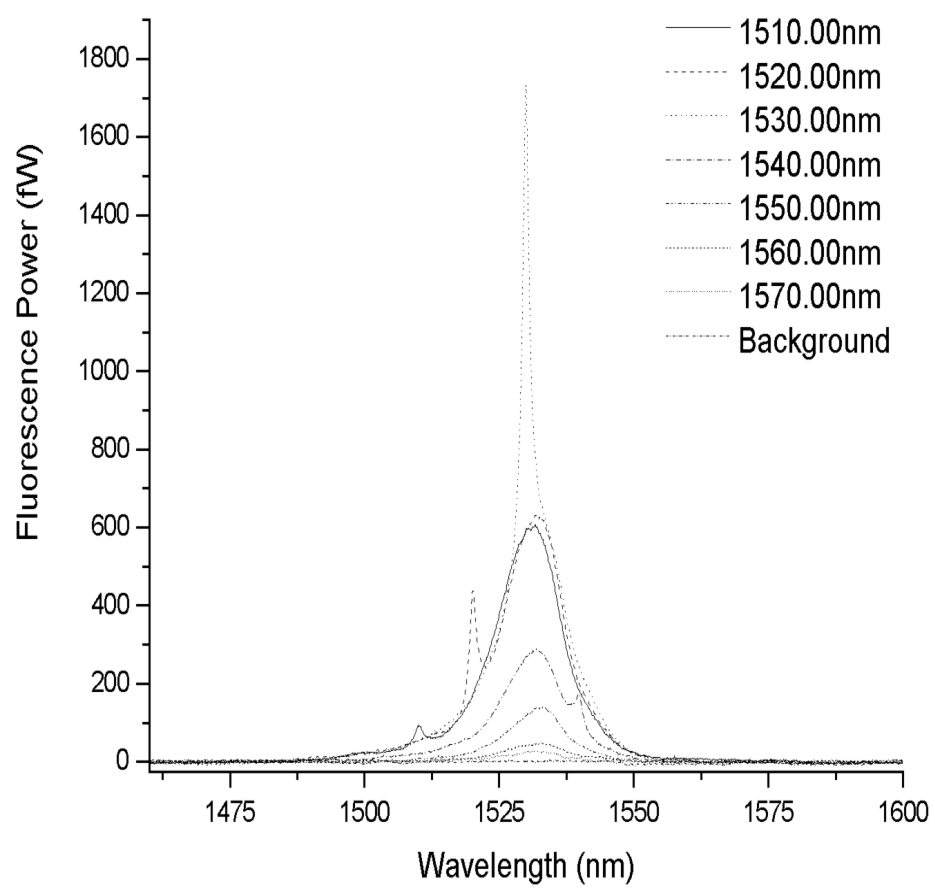


Figure 3.35. Fluorescence power versus wavelength for all excitation wavelengths.

Figure 3.36 is a plot of the background (i.e., the output of the spectrometer with the sample fluorescence blocked).

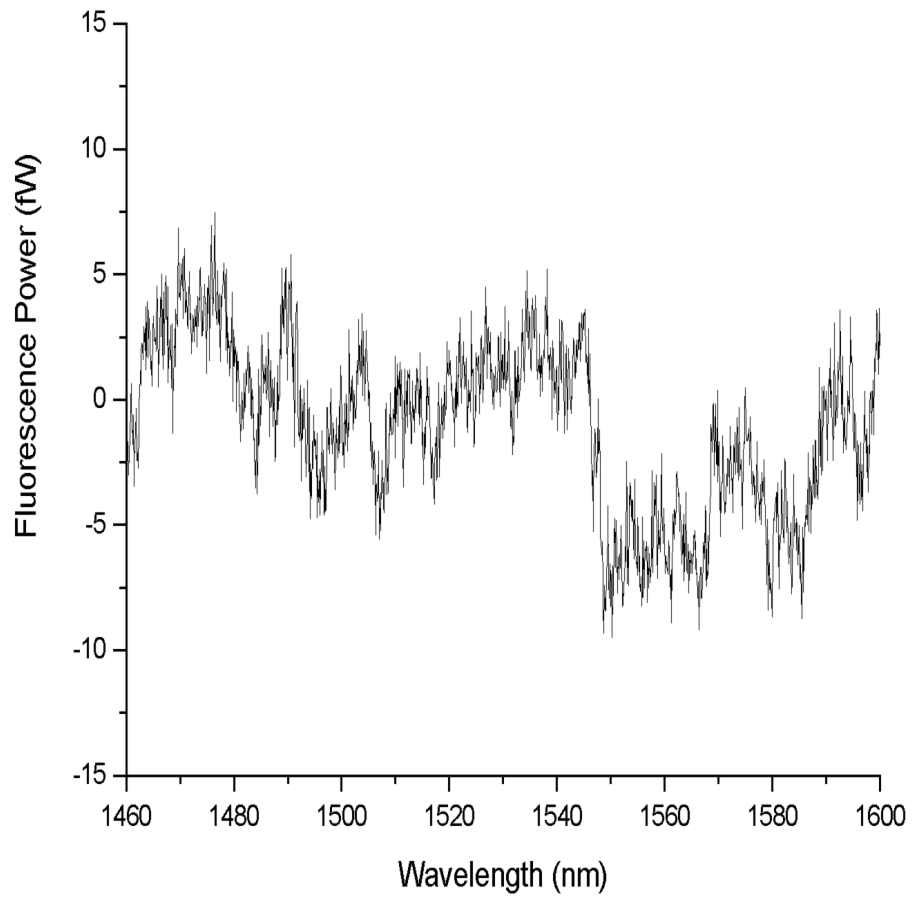


Figure 3.36 Spectrometer background noise with fluorescence light blocked.

Figure 3.37 is a plot of the liquid helium cooled sample's fluorescence power versus wavelength for an 0.2 mW 980 nm excitation pump laser. The excitation light from the laser is chopped with a frequency of ~ 2000 Hz. The wavelength scan increment is 0.5 nm with an integration time of 0.25 sec. while the instrumental resolution is ~ 1 nm.

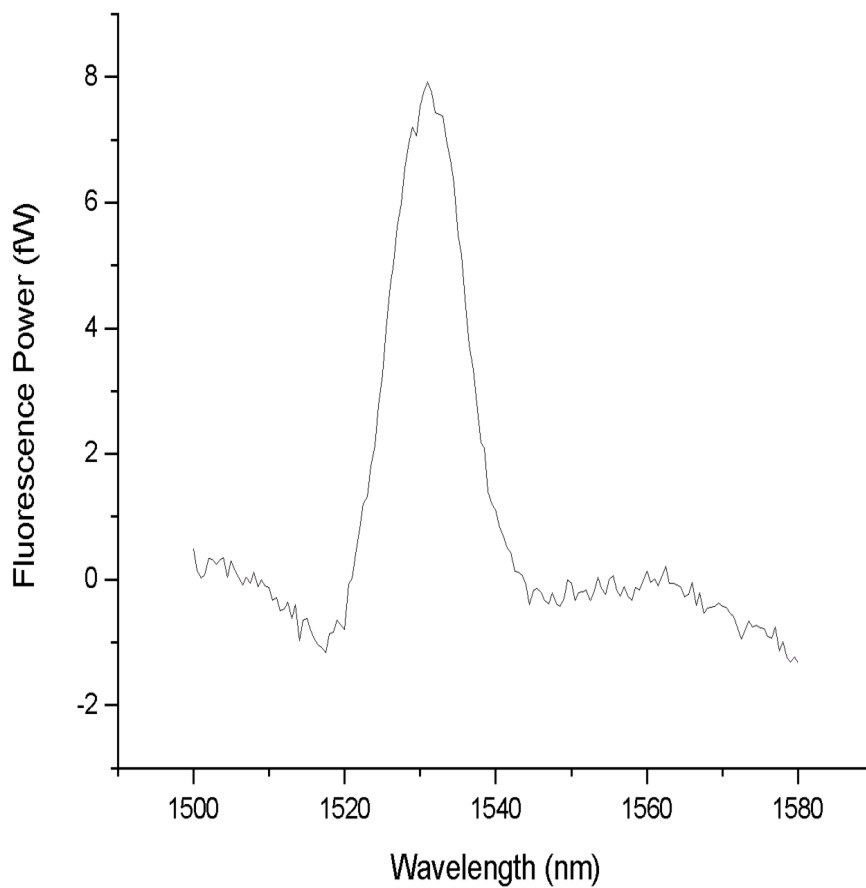


Figure 3.37. Fluorescence power versus wavelength for 980 nm excitation.

Discussion of Fluorescence Line Narrowing Data

As can be seen from figures 3.8 through 3.24 there are spectrally narrow features and spectrally broad features contained in the power spectra of the liquid-helium cooled sample fluorescence. The narrow feature has a width that is approximately equal to the spectrometer's instrumental resolution and a center wavelength equal to the excitation wavelength. This narrow feature corresponds to direct optical radiation on the ${}^4I_{13/2}(1)$ to ${}^4I_{15/2}(1)$ transition. That is, this fluorescence comes from ions that are resonantly excited into the inhomogeneously broadened ${}^4I_{13/2}(1)$ level by the excitation field. Figure 3.25 shows the power of the narrow feature as a function of wavelength, thereby mapping out the inhomogeneous profile of the ${}^4I_{13/2}(1)$ Stark level. The inhomogeneous profile is centered close to 1531.00 nm with a full width at half maximum of ~ 12 nm. This fluorescent method of measuring the inhomogeneous profile has the advantage, over the absorptive method generally used, of removing absorptive features associated with the non-ground Stark levels of the ${}^4I_{15/2}$ manifold.

The spectrally broad feature contained within the fluorescence power spectrum is associated with two sets of ions. 1) Ions that are excited to the ${}^4I_{13/2}(2)$ Stark level, undergo phonon-mediated, inter-Stark decay across the entire inhomogeneously broadened ${}^4I_{13/2}(1)$ Stark level and, finally, decay optically into the ${}^4I_{15/2}$ Stark manifold [45]. And 2) ions that are resonantly excited to the ${}^4I_{13/2}(1)$ level but subsequently follow intra-Stark, spontaneously-emitted, phonon-mediated energy migration pathways [46-47]. The ions that undergo this prominent intra-Stark-level energy migration pathway do so with a single-phonon direct process as indicated by the well-defined separation between

the broad and narrow fluorescence features as shown in figures 3.12 through 3.17 where the excitation wavelength was clearly within the ${}^4I_{13/2}(1)$ level. That is, low phonon-mediated energy transfer at small energies is expected due to vanishing lattice-phonon mode density at the small energies characteristic of the homogeneous linewidth in the system. The small broad, blue-shifted feature (with respect to the narrow feature) seen clearly in figures 3.18 through 3.23 results from phonon absorption [47]. The fact that, when the excitation wavelength is on the red side of the barycenter of the ${}^4I_{13/2}(1)$ level, there are small broad features on both sides of the narrow feature at small energies indicates that these features are brought about by an intra-Stark, two-phonon process. The weak nature of these small, two-phonon spectrally diffusive features compared to the former large red-shifted, single-phonon feature is explained by the expected mismatch in transition probabilities between one and two-phonon mediated absorptive/emissive processes at this temperature.

The difference between the narrow and broad peak changes as a function of excitation wavelength as shown in figure 3.26 and is a result of the interplay between the intra/inter Stark-level energy migration dynamics as the excitation wavelength changes.

Figures 3.28 through 3.35 show essentially the same type of fluorescence power spectra as before except that the sample is cooled to liquid nitrogen temperature. As can be seen in these figures, there are again spectrally narrow and a spectrally broad features. The explanations for these features is largely the same as before. But in this case the broad feature does not shift as much with respect to excitation wavelength as in the LHe-cooled case. An explanation for this is that the broadening of the ${}^4I_{13/2}(1)$ Stark level is partly homogeneous and partly inhomogeneous at 77 K.

Figure 3.37 is a plot of the non-resonant excitation fluorescence power spectrum for a 980 nm wavelength non-resonant excitation field. The peak is located at 1531.0 nm and has a width of approximately 11 nm.

Frequency Hole-Burning Experiment: Experimental Setup

The setup utilized in the hole-burning experiment is outlined in figure 3.38. The laser is the same as used in the spectroscopic measurements and the wavelength is tuned to 1530 nm.

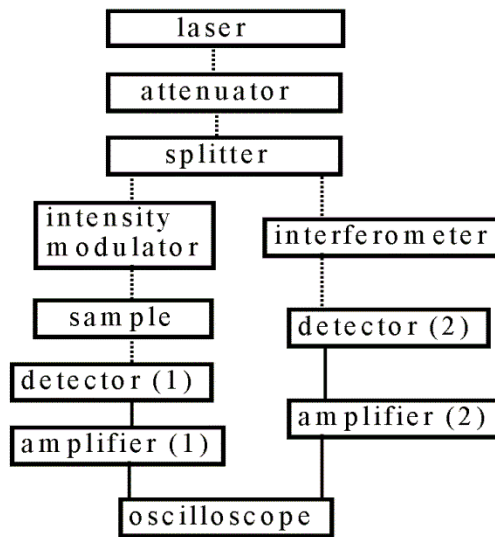


Figure 3.38. Schematic outline for hole-burning experiment.

The attenuator is a fiber optic fixed attenuation 10dB attenuator from WaveOptics Inc. The splitter is a 4-port 50/50 fiber optic beam splitter also from WaveOptics Inc. The intensity modulator is a single-mode fiber-optic coupled Mach-Zehnder-type

interferometric device from Uniphase Inc. with an insertion loss of ~ 3 dB, an extinction ratio of ~ 30 dB and a modulation bandwidth greater than 2 GHz. Detectors 1 and 2 are fiber-optic-coupled pin InGaAs photodiode optical detectors model D400FC from Thorlabs with a responsivity of 0.95 A/W at 1550 nm and a NEP of $1 \text{ fW/Hz}^{1/2}$. Amplifier 1 is a current amplifier model SR570 from Stanford Research Systems Inc. Amplifier 2 is a voltage amplifier model SR560 also from Stanford Research Systems. The oscilloscope is an 8-bit vertical resolution, 1 GHz analog bandwidth, digital storage oscilloscope model 9384L from Lecroy Inc. The interferometer (used to measure the frequency chirp rate of the frequency modulated laser) is a non-commercial (home-made) length of SMF-28 optical fiber housed in an aluminum box for temperature stabilization. The length of fiber is such that the interferometric free spectral range is $50 \text{ MHz} \pm 50 \text{ kHz}$. When the two ends of the fiber interferometer are connected to the rest of the fiber optic setup (as indicated in figure 3.38) with a small air gap between the interferometer's fiber and the splitter's and sample's fiber, small reflections at these interfaces produce the transmission pattern shown in figure 3.39. This figure shows the interferometer's transmission as a function of time while the laser is being frequency chirped. By counting the number of intensity peaks (or any other points of constant phase) during a given time the laser's frequency chirp rate can be measured. The approximate chirp rate and modulation amplitude were initially chosen such that the laser's frequency modulation frequency is below 2 kHz (the instrumental frequency modulation bandwidth limit). The form of the frequency modulation is triangular beginning and ending at the frequency of the burned hole. That is, the pump beam impacts upon the sample for ~ 50 ms, then the intensity modulator attenuates the pump beam (to produce the probe

beam) while the laser's frequency is swept across the burned hole ($\pm \sim 2\text{GHz}$ with respect to the hole frequency) in a triangular wave pattern.

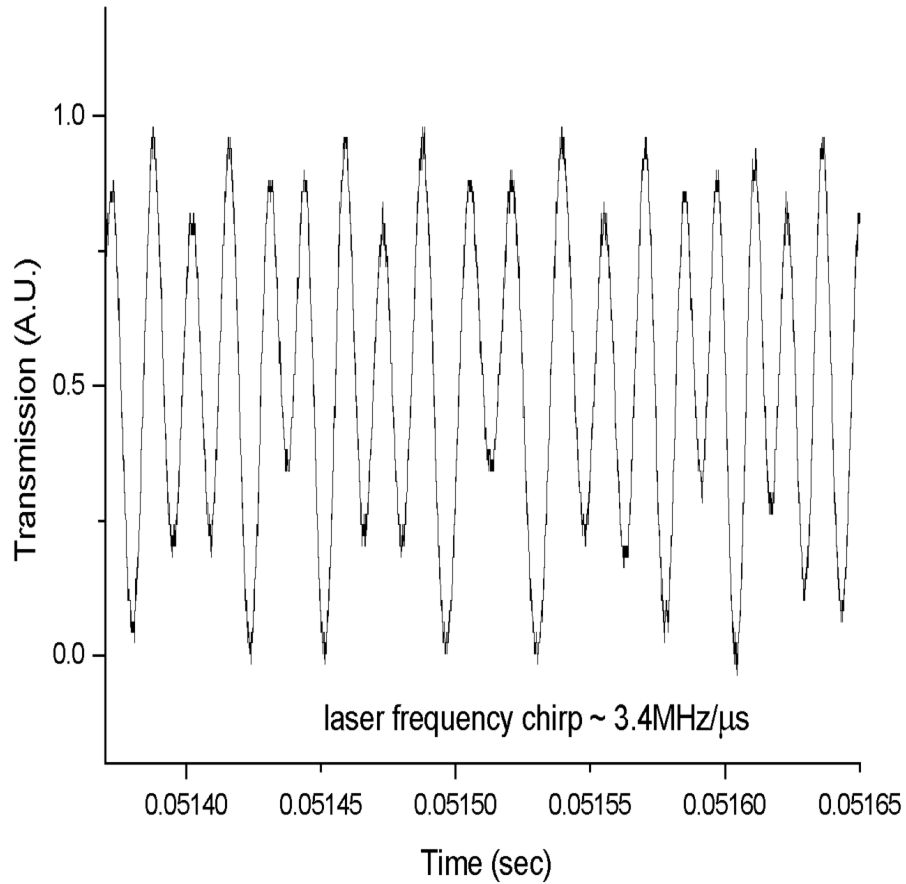


Figure 3.39. Interferometer's transmission versus time for frequency chirped laser.

The Frequency Hole-Burning Data

Frequency hole burning can occur when a laser of narrow linewidth (compared to the inhomogeneous width of a collection of atoms or ions) impacts these atoms putting a

portion of the absorption profile in an excited state. It is said that a hole has been burned or bleached within the absorption profile of these atoms

Figure 3.40 shows, for 4 probe powers relative to the $3\mu\text{W}$ pump power, the frequency swept probe transmission through the burned frequency hole.

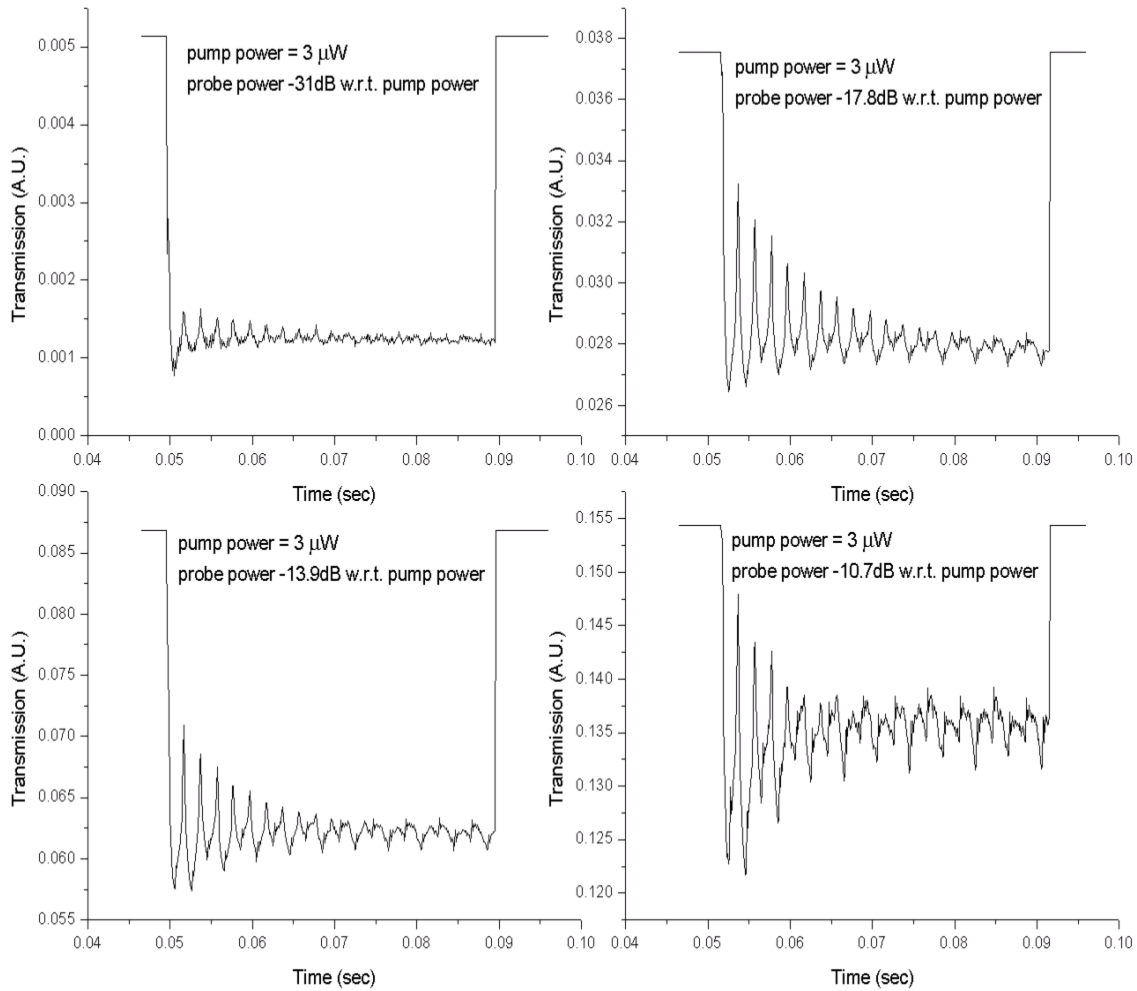


Figure 3.40. $3\mu\text{W}$ pump hole burning data.

Figure 3.41 shows, for 4 probe powers relative to the $0.5\mu\text{W}$ pump power, the frequency swept probe transmission through the burned frequency hole.

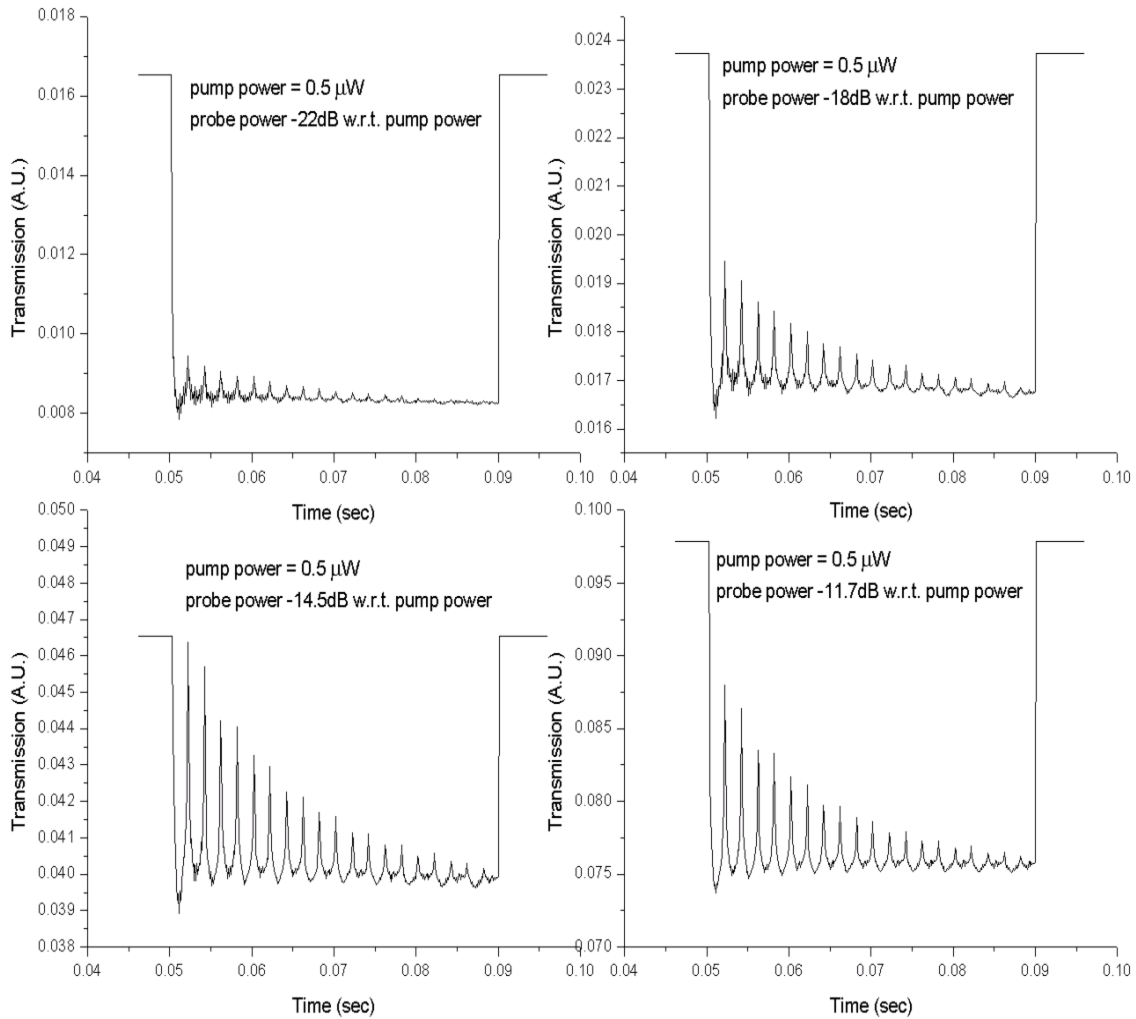


Figure 3.41. $0.5\mu\text{W}$ pump hole burning data.

Figure 3.42 shows, for 4 probe powers relative to the 100nW pump power, the frequency swept probe transmission through the burned frequency hole.

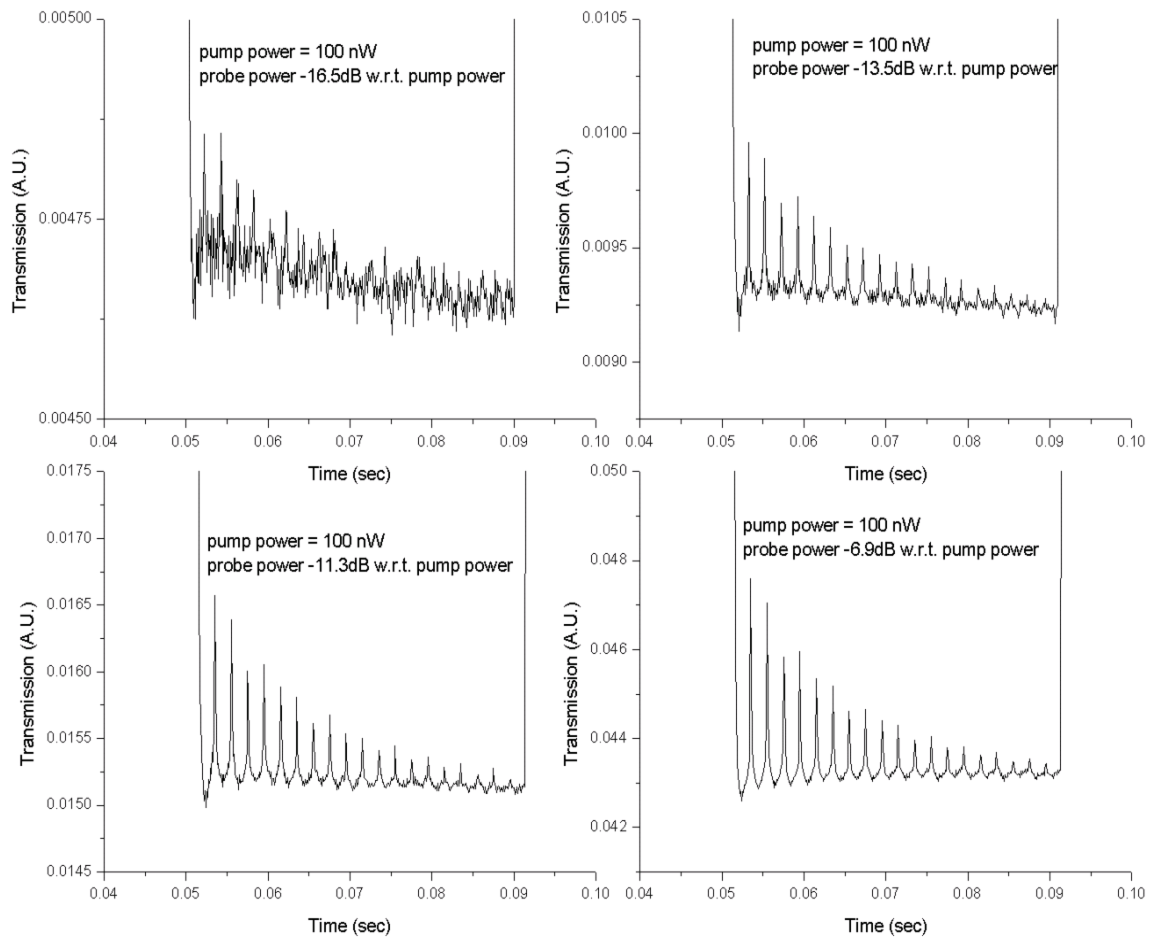


Figure 3.42. 100nW pump hole burning data.

Figure 3.43 shows, for 4 probe powers relative to the 10nW pump power, the frequency swept probe transmission through the burned frequency hole.

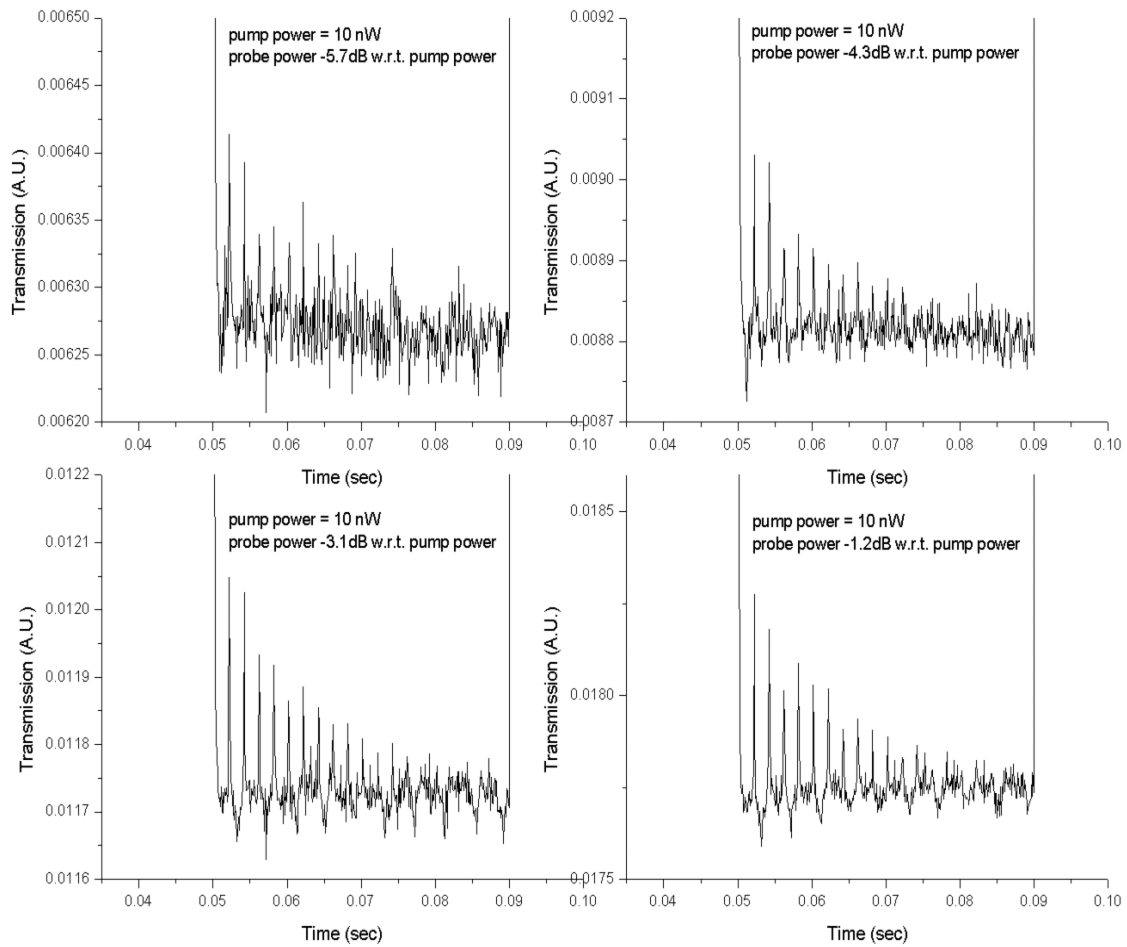


Figure 3.43. 10nW pump hole burning data.

Figure 3.44 shows, for a pump power of 1nW and a probe power down 1.5dB, the frequency swept probe transmission through the burned frequency hole.

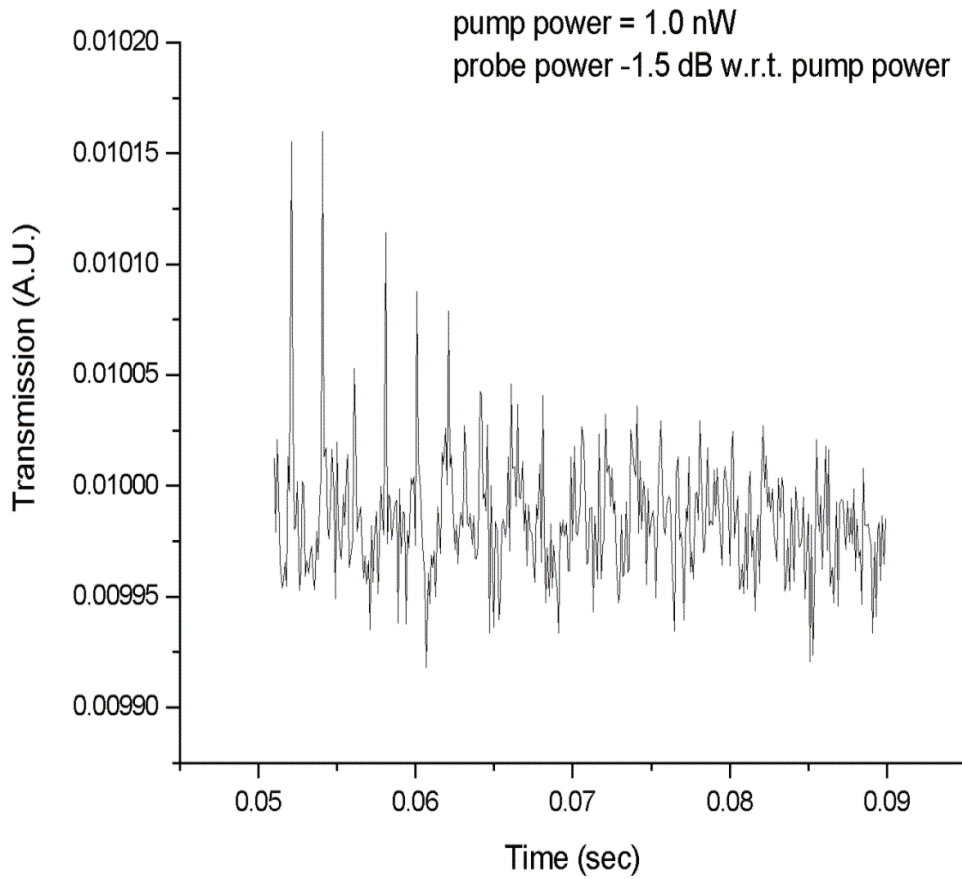


Figure 3.44. 1nW pump hole burning data.

Indicated in figure 3.45 is the decay constant ($1/e$ lifetime) as a function of pump power. The data points represent a statistical average (over the probe powers) of lifetimes measured for a given pump power.

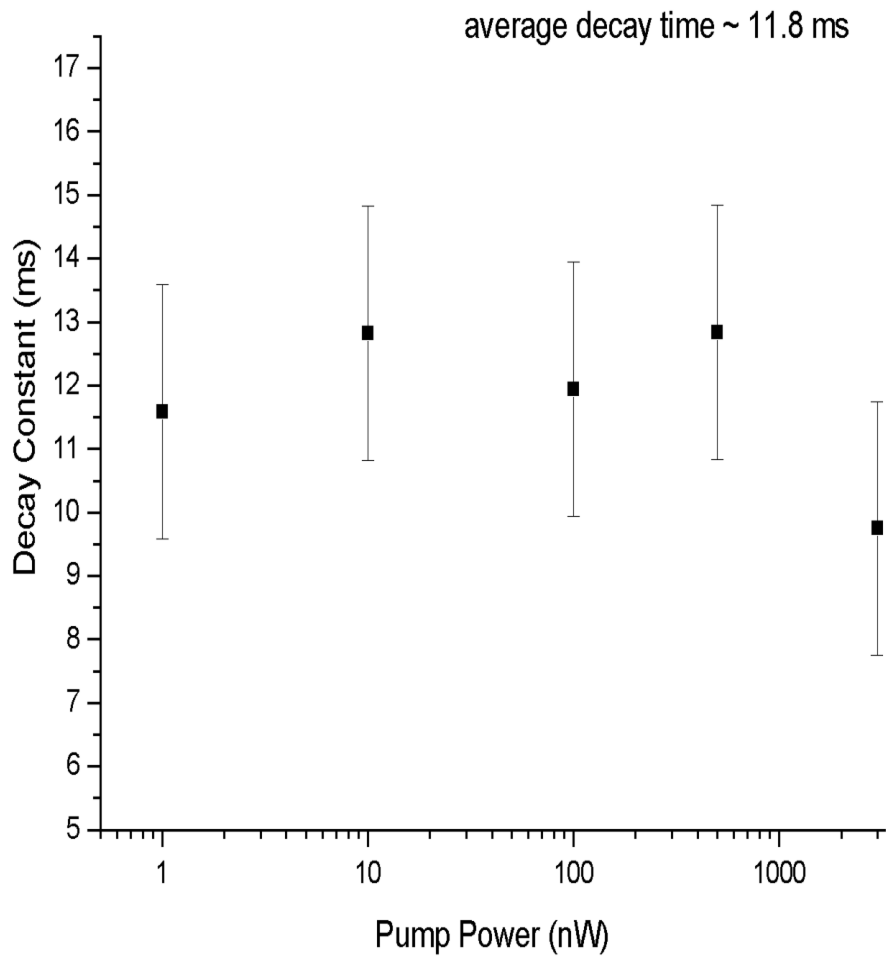


Figure 3.45. Decay constant versus pump power.

Shown in figure 3.46 is the hole width in MHz as a function of pump power in nW. The data points represent a statistical average of hole widths for a given pump power.

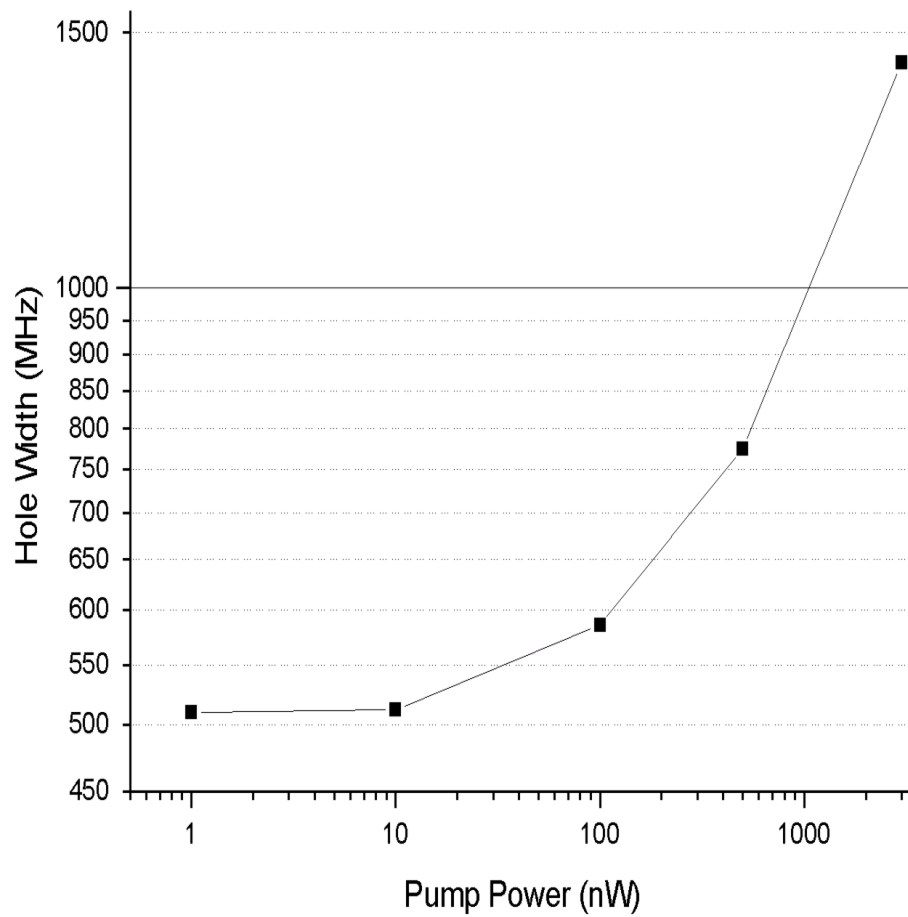


Figure 3.46. Hole width versus pump power.

Discussion of the Frequency Hole-Burning Data

As can be seen from figures 3.40 through 3.44 the pump power and relative probe power greatly affects the probe transmission. Figure 3.40 shows an average hole width of ~ 1.5 GHz, at the $3\mu\text{W}$ pump power employed, that is largely independent of the probe power. An increasing perturbation of the background (with respect to individual frequency scans) as the probe power increases can also be seen. The maximum background perturbation being $\sim 50\%$ of the maximum hole height for the case where the probe power is 10.7dB down from the pump power. 750 MHz is the average hole width shown in figure 3.41 where the pump power is $0.5\mu\text{W}$ and is again independent of probe power. However in this case the maximum background perturbation is $\sim 10\%$ of the maximum hole height. The hole width for a probe power of 100nW can be seen in figure 3.42 to be $\sim 600\text{MHz}$ (and is independent of probe power) where the maximum background perturbation is $\sim 100\%$ of the maximum hole height. Figure 3.43, in which the pump power is 10nW, shows a hole width of $\sim 500\text{MHz}$ that is again independent of probe power. The maximum background perturbation for this case is around 10% of maximum hole height. The pump power is 1.0nW for the data shown in figure 3.44 where the hole width is the same as in the previous case (500MHz). No background perturbation is observed in this case.

The hole decay time as a function of pump power is plotted in figure 3.45. The error bars include errors introduced due to the accuracy with which the hole widths can be measured. It can be seen that the decay time is approximately 11.8 ms and is largely

independent of pump power except possibly at the largest pump power where this may be due to excitation induced dephasing [48]. Figure 3.46 shows the hole width as a function of pump power. As mentioned above, given the data, the hole width is not discernibly a function of probe power. The hole width can be seen to decrease as a function of decreasing pump power until the pump power reaches $\sim 10\text{nW}$. This decrease is most likely due to power broadening of the transition. Below 10nW pump power the hole width is basically constant at $\sim 500\text{ MHz}$. Since the homogeneous width is half the hole width this yields a homogeneous width of $\sim 250\text{MHz}$.

This width is larger than that reported for typical rare-earth ions in crystalline hosts ($\sim \text{few kHz}$) because of the likely existence of low-energy, two-level tunneling states in amorphous materials [49-52]. That is, in glasses, at low temperatures there is an excess (with respect to ordered systems) of states that couple electronic and vibrational systems. This coupling brings about increased dephasing of the excited ion and thus a broadened homogeneous linewidth [53-60].

In considering the on/off fiber-Bragg grating resonance variation in the ionic spontaneous emission radiation rate of the real erbium solid state system, the multi-level state manifolds (upper and lower) and the intra-Stark level energy migration dynamics must be taken into account. As was shown at the end of Chapter II, the theoretical two-level lifetime variation is approximately 1%. It was assumed that all the light radiated from the excited ions existed spectrally within the grating's bandgap. As can be seen from the fluorescence line narrowing data, this is not the case. As a first approximation, the ratio of the area of the narrow spectral feature to the area of the broad spectral feature is a reduction factor in the observable lifetime variation. That is, not all the ions excited

by the grating-resonant excitation pulse radiate with the same wavelength as the excitation pulse. Therefore some ions do not experience a spatially and spectrally perturbed vacuum field and consequently radiate at their free-space rates reducing the overall lifetime variation. Considering that the narrow feature in the FLN data is instrument (spectrometer) limited and taking the true width to be the homogeneous width from the holeburning data, the reduction factor may be ~ 0.005 or smaller. Given this result and the objective of the lifetime measurement, the best choice for grating resonance is one that maximizes the reduction factor. A grating resonance wavelength (at LHe temperature) $\geq 1535.00\text{nm}$ will do this. A spectrally broader excitation source would likely be beneficial as well as discussed at the end of the next chapter.

CHAPTER IV

LIFETIME MODIFICATION MEASUREMENT: EXPERIMENTAL ATTEMPTS

In Chapter III the physical parameters of the erbium-doped fiber-optic system were reported. With these physical attributes measured, an attempt to determine the variation in the on/off fiber-Bragg grating resonance ionic lifetime may be made. This chapter serves as an exposition of the experimental attempts to measure the variation of the erbium-ion lifetime in the fiber-Bragg grating sample.

This exposition will begin with a description of the sample and experimental setup used in the attempt to measure the ionic lifetime variation. The results of the first attempt are then reported along with a discussion of these results. Following is a description of a second, altered experimental setup and the resultant lifetime variation measurement on the sample. The results of the second attempt are then given along with a discussion of the differences (and possible reasons for the differences) in the results between the first and second attempt. The first and second attempts were made before the spectroscopic measurements reported in the previous chapter were performed and, as a result, the sample fiber-Bragg grating resonance wavelength was not chosen so as to maximize the lifetime variation (as discussed at the end of the last chapter). A possible (but unrealized) future attempt is then outlined were a second sample (chosen in light of the spectroscopic measurements) and third experimental setup is employed.

First Attempt: Experimental Setup

The experimental setup used in the first attempt to measure the vacuum mediated ionic-lifetime variation is shown in figure 4.1.

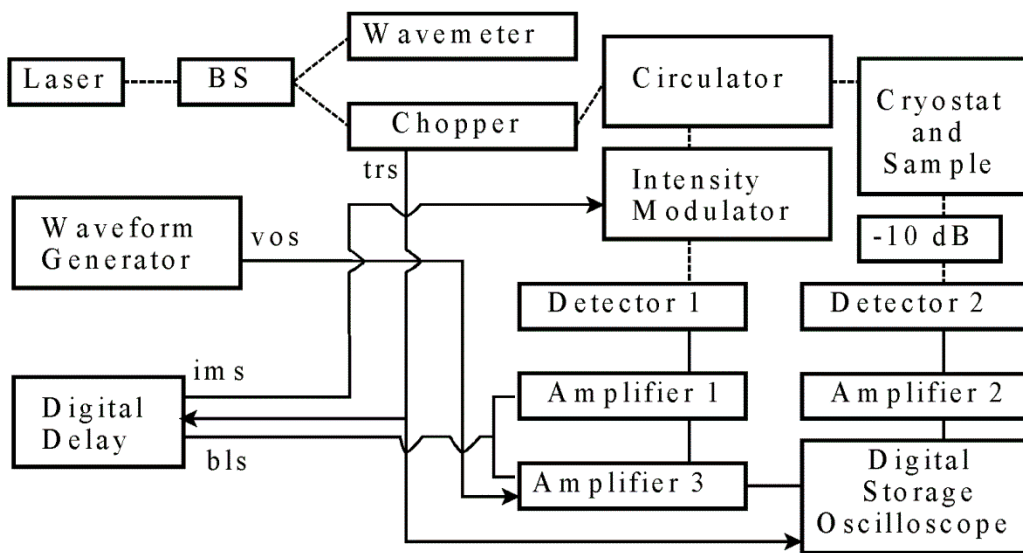


Figure 4.1. Experimental setup for first series of lifetime variation measurement attempts.

Now that the schematic of the experimental setup has been given in figure 4.1, a detailed description of the components and their function is necessary. The laser, 50/50 beam splitter (BS), Wavemeter, chopper (used with a different chopper wheel to be described below), circulator, cryostat, intensity modulator, detectors 1 and 2 and digital storage oscilloscope are the same as described in Chapter III. Figure 4.1 shows a 10dB fixed fiber optical attenuator from WaveOptics Inc. (box labeled -10 dB) between the sample and

detector 2. Amplifier 1 is the current amplifier SR570, Amplifiers 2 and 3 are voltage amplifiers SR560 (previously described). The waveform generator is from Sony/Tektronics and is model number AWG 2041. The digital delay is from Stanford Research Systems and is model number DG535. The dotted lines in figure 4.1 represent fiber optic coupled light paths while the solid lines represent electronic signal paths.

The excitation light originates from the laser and is directed to the 50/50 fiber optic beam splitter where 50% (power) of the laser light is sent to the Wavemeter in order to monitor the wavelength of the excitation light. The other 50% (power) of the laser light is sent to the optical chopper that is set to chop at ~ 10 Hz with a 50% duty cycle. A non-commercial chopper wheel (different from the wheel described in Chapter III) was fabricated in the University of Oregon's student shop with the help of Chris Johnson and David Senkovich. A schematic of the ~ 4 inch diameter chopper wheel is shown in figure 4.2. The dark curved area is the open portion of the chopper wheel. When the open region is rotated in front of the excitation light's path the excitation light is allowed through to the circulator and on to the sample. Conversely, when the open region is not in the beam path excitation light is not allowed through to the rest of the system. When the light is allowed through the chopper wheel it is then sent to the circulator's port number 1 where it is routed to the circulator port number 2. The excitation light is then sent to the LHe cooled sample. The sample is a 1 cm length of INO's ER103 erbium doped fiber (characteristics given in Chapter III) whereupon a fiber-Bragg grating has been imprinted. Two multi-meter lengths of SMF-28 standard communication optical fiber have been fusion spliced to the ends of this sample. The sample (fiber-Bragg grating and fusion splices) was manufactured by O/E Land Incorporated.

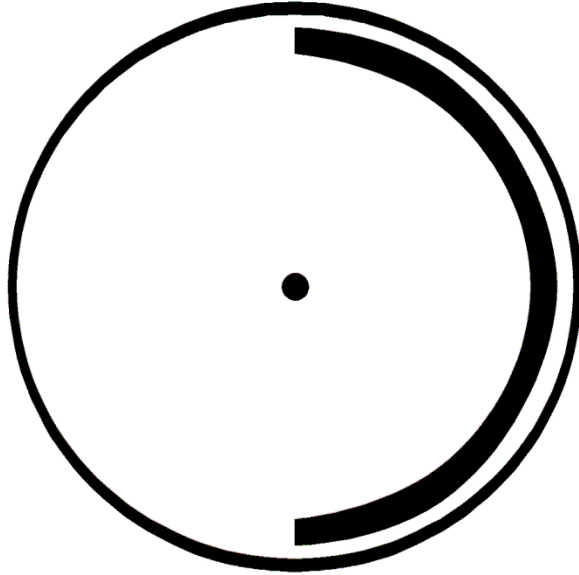


Figure 4.2. Diagram of optical chopper wheel employed in ionic lifetime measurements.

A schematic of the sample is shown in figure 4.3. The black dots (vertical lines) in figure 4.3 represent erbium ions (fiber-Bragg grating planes). As was the case for the sample used in the spectroscopic measurements of the previous chapter, the exact nature of the spliced regions is unknown. The entire sample is enclosed in a plastic fusion splice protection jacket. Light that is transmitted through the sample (used to observe the fiber-Bragg grating transmission profile) is sent to a fixed fiber-optic 10 dB attenuator and then to detector number 2. Detector number 2 converts the optical signal to an electrical signal and sends the photo-current to amplifier number 2 which sends an amplified signal to the digital storage oscilloscope for storage and/or processing.

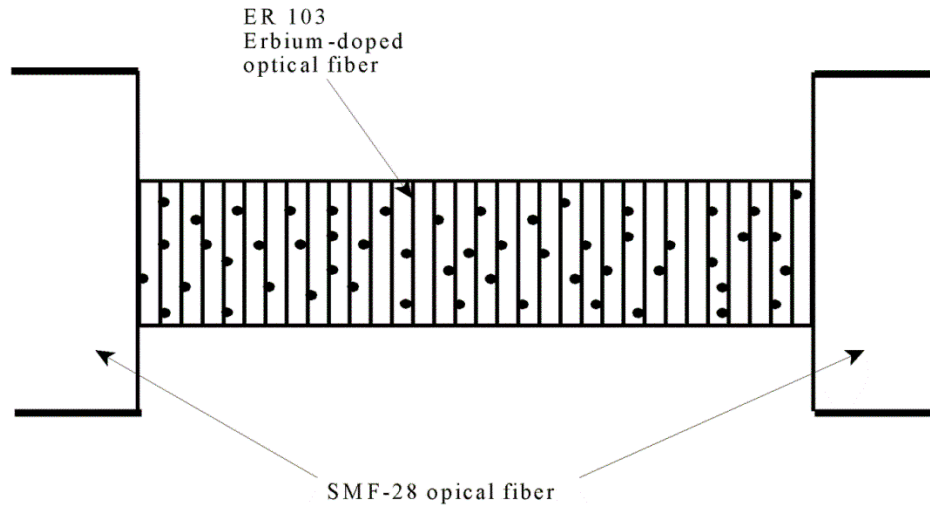


Figure 4.3. Schematic of erbium doped fiber-Bragg grating sample. Only fiber cores are shown (not fiber claddings).

The portion of the erbium-fluorescence light that is guided in the fiber core back toward the circulator is incident on port 2 of the circulator and is transmitted to circulator port 3. From port 3 the fluorescence is sent to the intensity modulator. The intensity modulator is controlled by the electronic signal, labeled *ims* in figure 4.1, from the digital delay (which is triggered by the electrical signal from the optical chopper controller labeled *trs* in figure 4.1) in such a way as to reduce the excitation pulse power into detector 1 by ~ 30 dB while allowing the sample fluorescence to pass with ~ 5 dB attenuation on to detector 1. Detector 1 then converts the 30dB attenuated excitation pulse and the 5 dB attenuated fluorescence signal to a photo-current which is sent to amplifiers 1 and 3. Amplifier 3's intrinsic voltage offset is reduced by subtracting a constant dc voltage level (labeled *vos* in figure 4.1 supplied by the waveform generator) from the background

voltage level. The signal (excitation pulse plus fluorescence) is then sent to the digital storage oscilloscope.

First Attempt: Transmission Versus Wavelength of Sample

For the initial sample a minimum in transmission at 4.5 K occurs at approximately 1519.75 nm. The experimental setup used to measure the transmission versus wavelength is shown in figure 4.4. The laser is the same as used in the previous measurements. The detector is the D400 FC model, the amplifier is the SR570 current amplifier, and the oscilloscope is the 9384L model (all mentioned previously). The light travels from the laser to the erbium doped fiber-Bragg grating sample and then on to the detector. The detector responds with a photo-current that is sent to the amplifier which amplifies and filters the photo-current with a 100 Hz low-pass filter. The subsequent signal is sent to the oscilloscope where it is stored. The laser also sends to the oscilloscope a voltage signal (marked W_{av} in figure 4.4) that is proportional to the wavelength. Using the voltage signal W_{av} and the amplified photo-current the transmission versus wavelength may be plotted. Figure 4.5 shows the transmission as a function of wavelength of the initial sample at 4.5 K. This transmission profile was obtained with an eight-bit vertical resolution digital oscilloscope so the true depth of the transmission minimum is not shown.

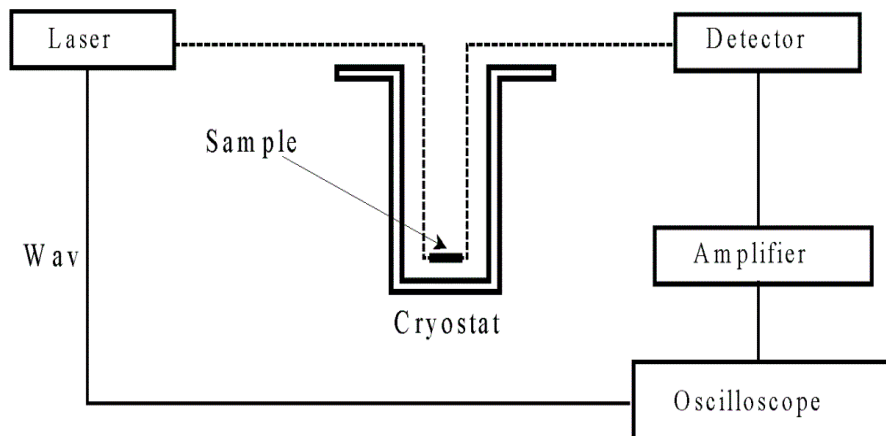


Figure 4.4. Experimental setup for measuring transmission at 4.5 K of sample.

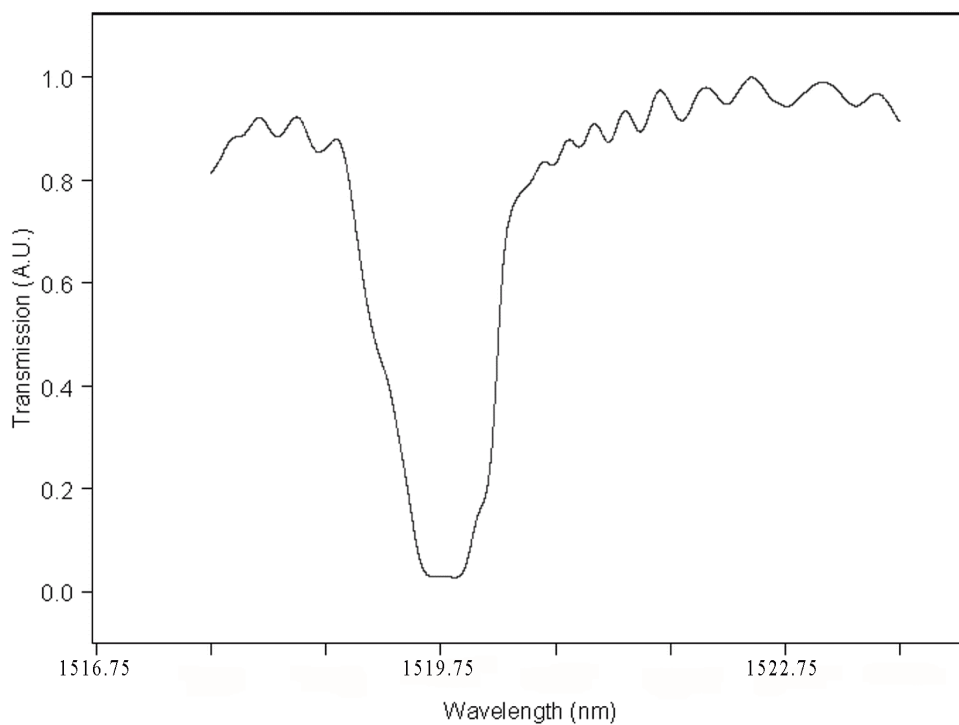


Figure 4.5. Transmission versus wavelength of sample at 4.5 K.

Fractional Lifetime Change Versus Wavelength

The fractional lifetime change is given by $(T_1 - T_0)/T_0$, where T_1 is the lifetime measured from fitting the temporally resolved fluorescence to an exponential decay function and T_0 is the off fiber-Bragg resonance or unperturbed lifetime. The fractional lifetime change is shown in figure 4.6. The data plotted in figure 4.6 is obtained employing the experimental setup shown in figure 4.1 and contains the average of the fractional lifetime change for two experimental runs. The error bars are assigned to be the averaged statistical standard error.

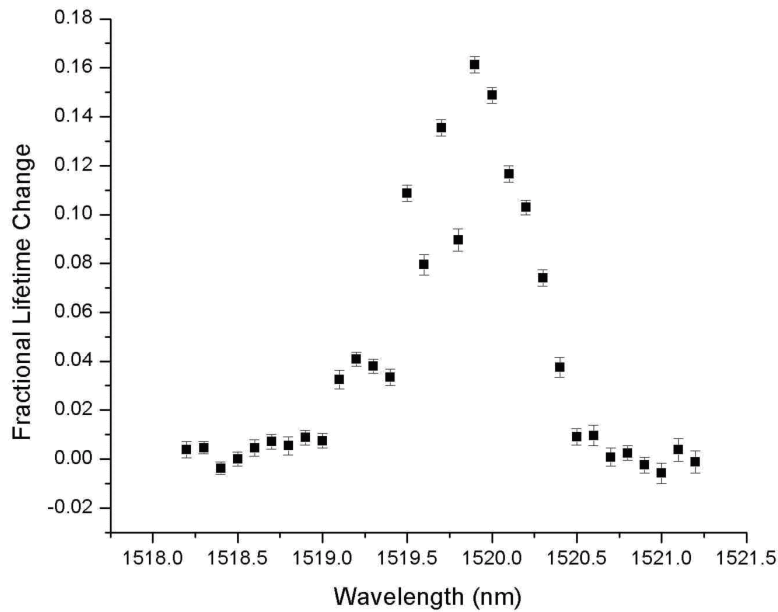


Figure 4.6. The fractional lifetime change for the sample and experimental setup.

Each data point is the average of ~ 50 recorded traces each of which is the average of 250 decay events. That is, 250 decay events are averaged into a single recorded trace and approximately 50 of these traces are averaged to produce the data point at a single wavelength.

This plot seems to indicate a lifetime enhancement of ~ 16% associated with the fiber-Bragg grating resonance. Due to (at the time this data was taken) unknown systematic errors associated with the experimental setup (believed to be associated with the interaction between the reflected resonant excitation laser power, intensity modulator and the amplifiers) this turns out not to be the case as will be discussed below. A single recorded trace for wavelength = 1521.2 nm is shown in figure 4.7 in a linear-linear plot and in figure 4.8 in a log-linear plot. The raw data has been fitted to an exponential decay function $y(t) = A + Be^{-t/T_0}$, where A, B and T_0 are constants and the constant A (as determined by the computer fitting procedure) has been subtracted off the raw data with the resultant data being normalized and plotted in figure 4.7 and figure 4.8.

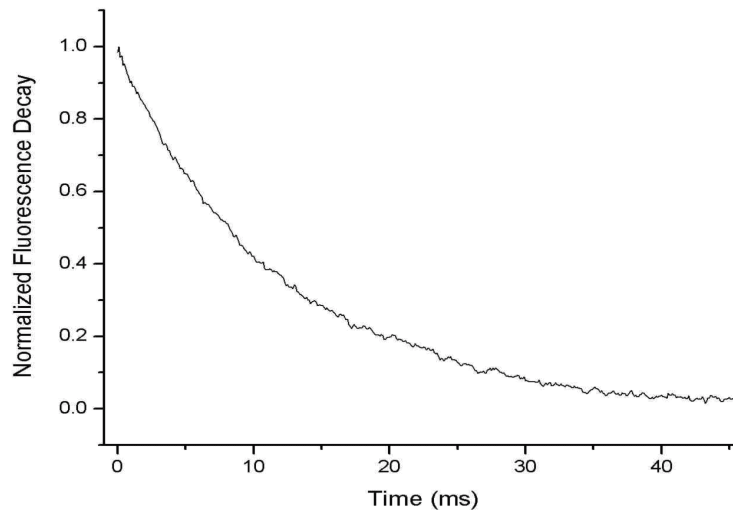


Figure 4.7. Fluorescence decay versus time for a single trace recorded at 1521.2 nm.

As can be seen in figure 4.8, the fluorescence decay extends over only a $1\frac{1}{2}$ decade range before the noise becomes significant. A larger range would clearly allow the computer fitting procedure to yield decay constants of higher integrity.

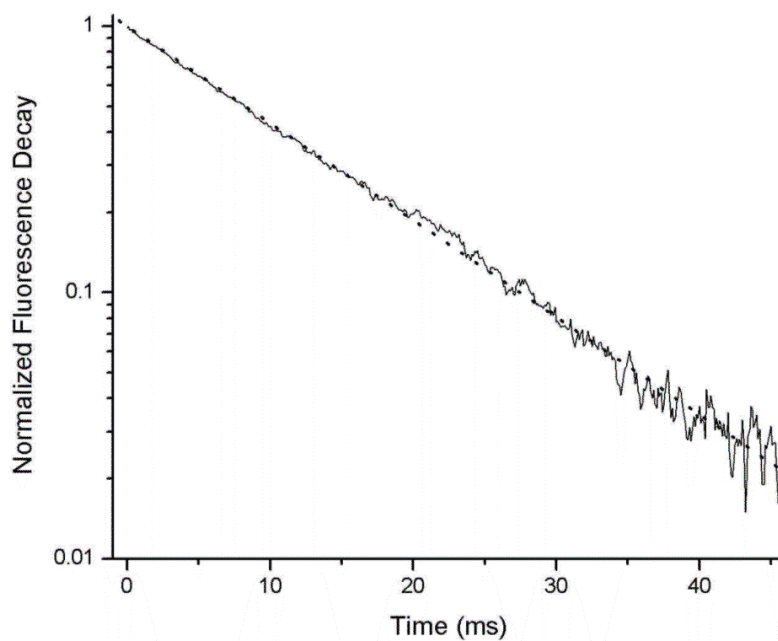


Figure 4.8. Fluorescence decay versus time for trace recorded at 1521.2 nm. Solid line: data. Dotted line: linear fit.

Second Attempt: Experimental Setup

The second attempt to measure a change in ionic radiative lifetime was performed using the same sample and an altered experimental setup as shown in figure 4.9. The excitation light originates with the laser (same as in figure 4.1) and travels through single mode fiber to the 99-01 beam splitter (BS) where it is sent to the optical chopper (labeled chopper 1 in figure 4.9 and is the same as in figure 4.1) and the Wavemeter.

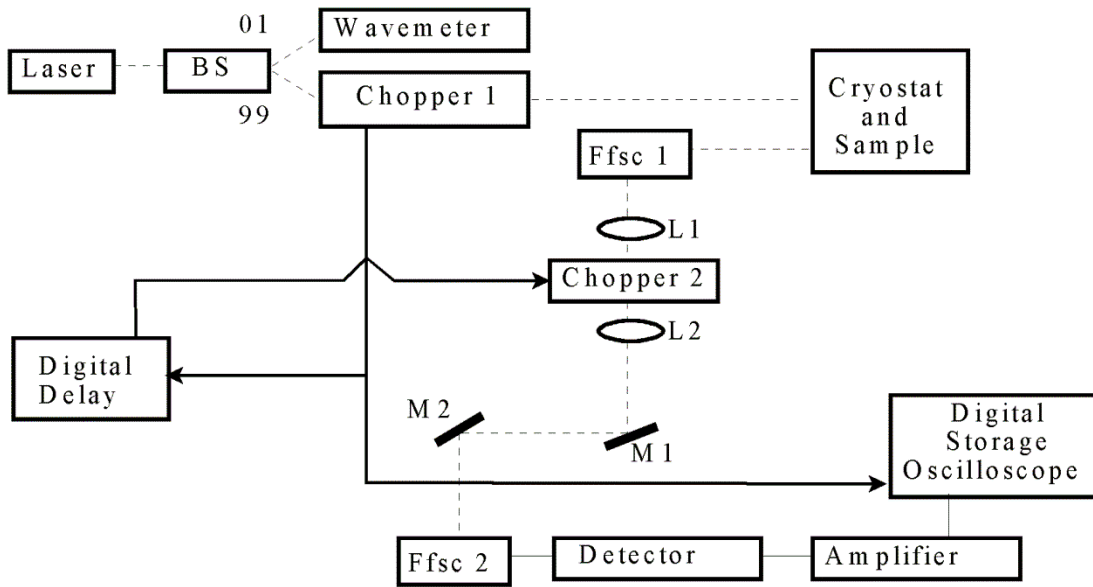


Figure 4.9. Experimental setup for second lifetime variation measurement attempt.

From chopper 1 (chop rate is 7 Hz) the light is sent to the sample located in the cryostat. Fluorescence from the erbium ions that is collected in the fiber core is sent to the free space light coupler Ffsc1(Thorlabs model number F220FC-1550). The fluorescence is

then sent through free space (not fiber guided) to a 10cm lens L1 that focuses it down to a spot at chopper 2 (Uniblitz model 100-2B) yielding a fluorescent light pulse with a 50 μ s rise time. This light pulse is then sent to a 5cm lens L2 followed by two steering mirrors (M1 and M2) and on to a second fiber to free space coupler used in reverse (Ffsc 2). The light is then fiber guided to the detector (a multimode fiber coupled InGaAs avalanche photodiode (APD)) and on to the current amplifier (SR570 with the input filters turned off and running under battery power). The electric fluorescence signal is then sent to the digital storage oscilloscope for recording. Chopper 1 triggers both the oscilloscope and the digital delay. The digital delay sends an electronic triggering signal to chopper 2 so that chopper 2 completely eliminates the excitation pulse from the detection, amplification and recording systems while allowing the fluorescence light pulse to travel on to the detection (and subsequent) systems.

The main difference in this setup, as compared to the setup initially employed, is the replacement of the Mach-Zehnder intensity modulator with its less than infinite extinction ratio, i.e., it let $\sim 0.1\%$ of the reflected excitation light reach the detection system, with the free space optical chopper (chopper 2) that has an infinite extinction ratio, i.e., no reflected excitation light gets to the detection system. The optical circulator is also eliminated in this setup. The amplification system is altered and simplified by the replacement of the PIN photodiode with the InGaAs APD and the elimination of the voltage amplifier (and its associated long term drift and recovery time) used in conjunction with the current amplifier in the previous setup.

Second Attempt: Data

Figure 4.10 shows a two wavelength (on-off fiber-Bragg grating resonance) ionic lifetime measurement, using the sample discussed above, taken with the experimental setup that is depicted in figure 4.9.

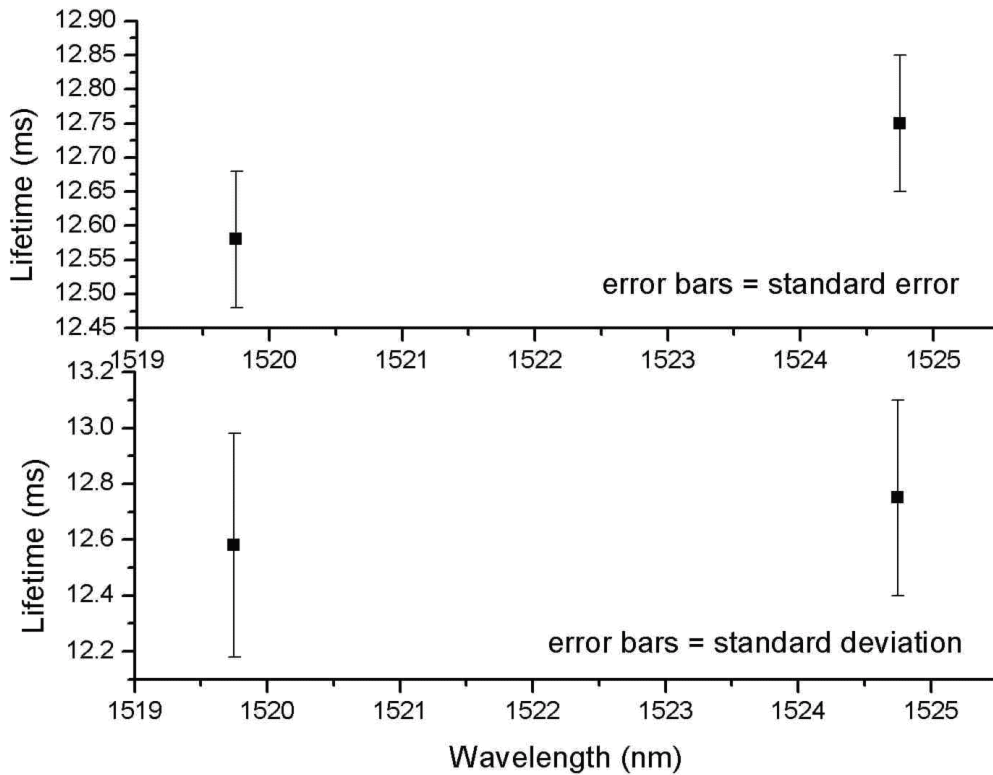


Figure 4.10. Two wavelength ionic lifetime measurement of sample and second experimental setup (two data runs).

The data shown in figure 4.10 indicates that no statistically significant lifetime modification is observed. As can be seen, the ratio of the error to the average value in the top (bottom) data set in figure 4.10 is $\sim 1.5\%$ (6%). While the maximum expected change

is $\sim 1\%$ (and with the unfortunate choice of FBG cavity wavelength closer to 0.005%). In addition, the edge effects of this sample are largely unknown and are likely a significant contributor to the measured fluorescence signal. This results from the diffusion of the Er ions that occurs when Er-doped fiber is fusion spliced onto standard single mode fiber (smf) [42]. The larger relative error here (as opposed to the results of the first attempt) comes from the change of the all fiber guided post-sample fluorescence of the first attempt to the partial fiber-guided and partial free-space path (with its concomitant coupling losses) of the second experimental setup as shown in figure 4.9. That is, relatively less fluorescence light was incident upon the detection/amplification system so the decaying fluorescence signal was closer to the system noise floor. Stated in another way, the change in observation method from the first to the second attempt reduced systematic errors but increased random errors.

Possible Future Attempt

A possible future experiment, where a new sample is chosen so that its LHe temperature FBG wavelength lies around 1535nm and also has greater absorption (yielding more fluorescence signal) coupled with a new excitation/detection scheme, may overcome some of the deficiencies of the previous two attempts and yield an observable cavity-induced lifetime modification. That is, an excitation source with a spectral width chosen so as to maximize the reduction factor (mentioned at the end of chapter III) coupled with time correlated single photon counting may yield a measurable result. In addition, a side pumping scheme may also be employed to produce higher pump powers

within the grating. This would require a sample without the fusion splice protection jacket. The new sample, in addition to having a LHe wavelength close to 1535nm could be constructed in a way so as to eliminate edge effects of the cavity. That is, ensure that the Er ions are deep within the grating. This could be done by first fusion splicing a small section of Er-doped fiber between two longer sections of smf (not a simple task) then writing a FBG that spatially extends relatively far beyond the fusion splices (also not a trivial procedure given the core NA, and co-dopant mismatches between the fibers). Another possible sample that would extend the photonic bandgap fully into 3 dimensions (greatly increasing the lifetime modification) is one where an Er-doped FBG core is contained within a photonic crystal fiber with an appropriately chosen transverse bandgap. This would shield the Er-ions from the vacuum field over a 4π solid angle range.

CHAPTER V

CONSTRUCTION AND CHARACTERIZATION OF A RAPIDLY TUNABLE LASER SYSTEM

The tuning and coherence properties of a short-external-cavity diode laser are examined using a fiber-based self-heterodyne technique [61]. Insertion of an electro-optic crystal in the 5 cm external locking cavity is shown to enable continuous, voltage-controlled, tuning over approximately 3 GHz at tuning speeds up to 23 GHz/ μ sec. The quiescent short-term, 1 ms optical linewidth is approximately 10 kHz. Coherence properties during active frequency scans are characterized through analysis of time-dependent heterodyne beat signals at the output of a fiber interferometer. A frequency locking method based on stabilization of the same self-heterodyne beat frequency is described.

Semiconductor diode lasers, because of low cost, high quantum efficiency, and compact size have been utilized in a variety of applications. When high coherence is required, the laser diode can be locked to an external cavity. Lasers with high coherence and the capability for rapid continuous tuning are important for a number of applications. We investigate the high-speed continuous tuning properties of a diode laser stabilized by a short 5 cm external cavity and tuned using an intracavity electrooptic crystal.

A large body of results pertaining to the spectral tuning properties of external cavity diode lasers has previously been reported [62]. These investigations have primarily focused on tuning several nanometers with the use of mechanically controlled intracavity etalons or mechanical rotation of a grating while simultaneously adjusting the diode current or the external cavity length, or acousto-optic tuning. In the present work, we explore the spectral tuning behavior as well as quiescent and frequency-swept coherence properties of an external cavity laser diode with an intracavity electrooptic crystal (EOC), designed for spectral holographic memory applications.

Description of System

The schematic of our laser system is shown in figure 5.1 . The laser employs the Littrow grating configuration to provide relatively high feedback intensity and to facilitate external-cavity-length minimization.

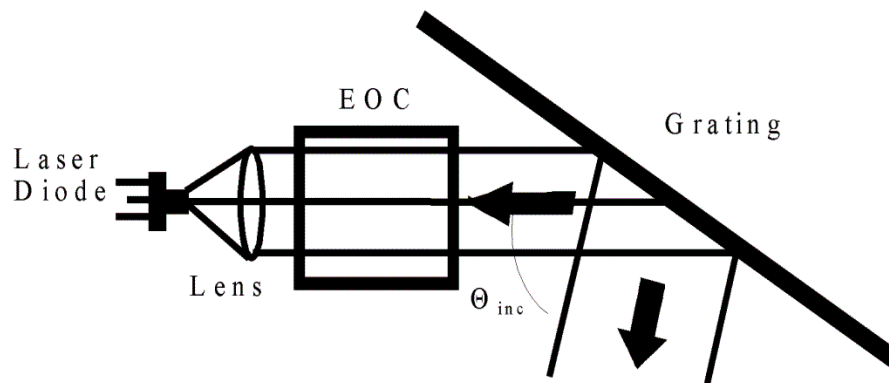


Figure 5.1. Littrow grating laser configuration.

The laser diode (Sharp LT0 25 MD0) is anti-reflection (AR) coated. Its output polarization (direction of maximal output divergence) is parallel (perpendicular) to the grating rulings. The grating (130.1200 from American Holographic) is measured to diffract about 55% of the laser diode's power into the Littrow feedback beam (first order). The band pass of the grating is given by

$$\Delta \nu_g = \frac{dc}{\lambda D} \cos(\Theta_{inc}) \quad (5-1)$$

where $\lambda = 790\text{nm}$ is the wavelength and $\Theta_{inc} = 28^\circ$ is the grating input angle, $d = (1200\text{lines/mm})^{-1}$ is the grating line spacing, $D = 2.2\text{ mm}$ is the optical beam width perpendicular to the grating grooves, and c is the speed of light. It follows that $\Delta \nu_g \approx 130\text{ GHz}$. Single mode operation is observed despite the fact that $\Delta \nu_g \gg \Delta \nu_{ext} = 3\text{ GHz}$, where $\Delta \nu_{ext}$ is the external cavity mode spacing, as verified by a 1 cm confocal Fabry-Perot spectrum analyzer. The aspheric collimating lens is AR coated with a focal length of 4.5 mm and a numerical aperture of 0.5. The EOC is comprised of an antireflection coated Lithium Tantalate crystal configured as a transverse phase modulator. For our system the relevant electrooptic coefficient is $r_{33} = 33 \times 10^{-12}\text{ m/V}$ and the extraordinary refractive index is $n_e = 2.16$, $l = 5\text{mm}$ is the crystal length, and $z = 1\text{mm}$ is the electrode spacing. The diode laser and external cavity are mounted on an Invar plate. The temperature of the laser diode was stabilized to better than 10mk.

Figure 5.2 shows a detailed outline of the experimental setup. A 2.26 km or a 8.43 km single mode fiber (Corning SMF-28) producing a time delay of 11 μs or 40 μs was used to provide a self-referenced local oscillator.

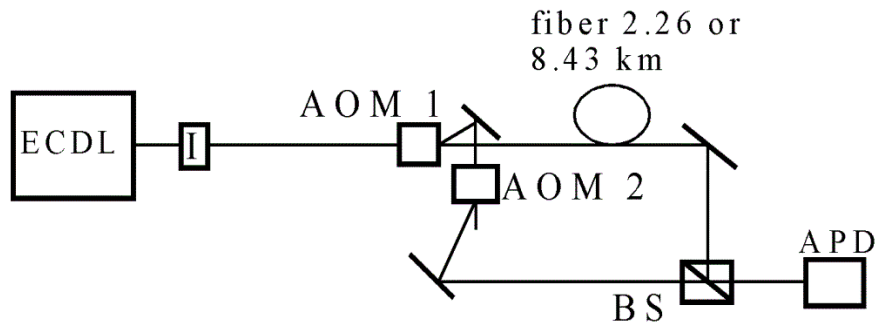


Figure 5.2. Schematic of experimental setup.

ECDL is the external cavity diode laser, I is an optical isolator, AOM1(2) are acousto-optic modulators and BS of a beam splitter/combiner and APD is an avalanche photodiode. AOMs 1 and 2 were used to produce two light beams with a variable offset within the bandwidth of our detection system. One beam went through the fiber while the other did not. The two beams were then optically combined on an EGG30998-050 avalanche photo-diode (APD) or a Hamamatsu S2382 APD depending on our expected detection bandwidth requirements. The beatnote produced in the absence of active frequency scanning was approximately 1 MHz.

Tuning

Grating rotation provides for slow frequency scanning which is not of interest here. High speed, many GHz/ μ sec, frequency scanning requires non-mechanical activation. To achieve this, the external cavity employed here is equipped with an electrooptic crystal, providing rapid voltage-controlled cavity-length laser output scans with cavity length change dL according to the relation $dL = \lambda V / (2 V_{\pi})$ and hence frequency scanning according to the relation

$$d\nu = -\Delta\nu_{ext} \left(\frac{V}{V_{\pi}} \right) \quad (5-2)$$

V is the applied voltage and $\Delta\nu_{ext} = 3$ GHz is external cavity mode spacing and for the crystal geometry employed, the half-wave voltage is given by $V_{\pi} = \lambda z / (r_{33} n_e^3 l)$ implying $V_{\pi} \approx 475$ V. Cavity length variation provides frequency tuning over approximately 1 external cavity mode spacing thereby motivating the cavity-length minimization employed in the present design. The continuous tuning using the EOC can be effected at great speed and over a range of ~ 3 GHz.

Self-Heterodyned vs. Actual Laser Frequency

Modeling and Interpretation

For a simple interpretation of the results of the self-heterodyne method for measuring the temporal coherence or linewidth of a laser the time delay between the two

heterodyned fields must be many times the coherence time of the laser itself. This ensures the independence of the two heterodyned fields. Then assuming a certain lineshape (usually Gaussian or Lorentzian) one can easily estimate the linewidth of the laser itself. The linewidth of the beatnote signal is twice the laser linewidth if one assumes a Lorentzian line profile or $\sqrt{2}$ times the laser linewidth if one assumes a Gaussian line profile. If the time delay is not many times the coherence time of the laser then the two fields are not independent and the resulting linewidth will be narrower than in the case above due to the partial correlation between the two fields. In order to infer what the result of the measurement would be for the independent fields given the partially correlated fields one can do numerical modeling based on various random phase jump models of the laser.

In our models we assume a constant laser field amplitude and four different types of sudden, discrete phase jumps all characterized by a single parameter τ_c that specifies the time scale on which the phase jumps occur. The four laser linewidth models are characterized as follows: (1) $\pm \pi$ phase jumps, with jump intervals evenly distributed between 0 and $2 \tau_c$, (2) the same as model (1), except that the phase jumps have random amplitudes in the range $(-\pi, \pi)$, (3) the same as model (1), except the jump intervals are distributed exponentially with an average jump interval equal to τ_c , (4) the same as model (2) except that the jump intervals are distributed exponentially with an average jump interval equal to τ_c .

We then create random phase histories $\Phi_0(t)$ (based on the models) and write the phase of the field as

$$\varphi(t) = 2\pi\nu \cdot t + \Phi_0(t). \quad (5-3)$$

We then heterodyne the field with a time delayed (τ_D) and frequency shifted version of itself to attain a beatnote signal proportional to $\cos(\Phi_0(t) - \Phi_0(t - \tau_D) + 2\pi\Delta\nu_{AOM} t)$. The full width at half-maximum of the autocorrelation function of this beatnote signal may be interpreted as the measured partially correlated coherence time of the combined fields given the time delay τ_D . A relation between laser linewidth $\Delta\nu_{laser} \sim 1/t_c$, τ_D and the measured linewidth of the partially correlated heterodyned fields can be attained as given in figure 5.3.

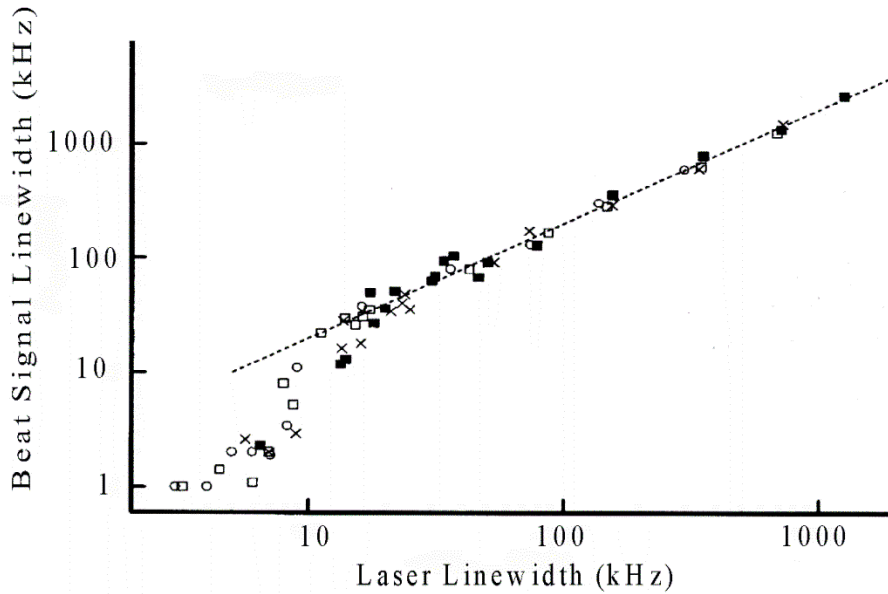


Figure 5.3. Interferometer intensity beat signal linewidth as a function of laser linewidth calculated assuming a time delay of $40 \mu s$ and one of the four different phase evolution models for the laser field. The symbols \times , \circ , \blacksquare and \square respectively, refer to phase models (1), (2), (3) and (4) described above. Dashed line, $\Delta\nu_{beat} = 2 \Delta\nu_{laser}$.

Each data point represents an average over 25 randomly generated phase histories of 1ms duration. The dashed line corresponds to $\Delta v_{\text{beat}} = 2\Delta v_{\text{laser}}$, which is expected for $\tau_c \ll \tau_{\text{delay}}$. When the laser linewidth is less than 25kHz, Δv_{beat} varies with Δv_{laser} in a complex fashion.

Experimental Results: Quiescent Linewidth

The setup in figure 5.2 was used with the EGG detector and with the 2.26Km fiber replaced by a 8.43Km SFM-28 single mode fiber. The linewidth, defined to be the full width at half maximum of the Fourier transform of the beatnote Δv_{beat} , over 1ms was measured to be 3KHz. Based on the results of the numerical modeling the laser quiescent linewidth Δv_{laser} is estimated to be approximately 10kHz.

Tuning Characteristics

Upon application of either an 80ns or a 350ns 300V linear ramp to the EOC, supplied by a high-voltage field-effect transistor, the beatnote ($\Delta v_{\text{AOM}} = 0$ in this case) initially increases in frequency, due to the time delay caused by the fiber ($\tau_f = 11\mu\text{s}$) as can be seen in figure 5.4. For frequency chirps longer than τ_f the beatnote frequency would stop increasing even though the laser frequency would still be rising.

The points in figure 5.4 a) represent a portion of the observed self-heterodyne beat signal. The solid curves in figure 5.4 are fits of a linear frequency chirp to the data. The dashed lines in figure 5.4 are the frequencies of the beat signal fits versus time. The chirp rate for the first 40ns of the 80ns chirp shown in figure 5.4 a) is $R_{\text{ch}} \approx 23\text{GHz}/\mu\text{s}$. In

figure 5.4 b) is plotted the heterodyne beat signal with a short time delay $\tau_D = 25$ ns and a chirp rate $R_{ch} \approx 6\text{GHz}/\mu\text{s}$. The beat frequency remains essentially constant (after the delay time) at $R_{ch} \tau_D$.

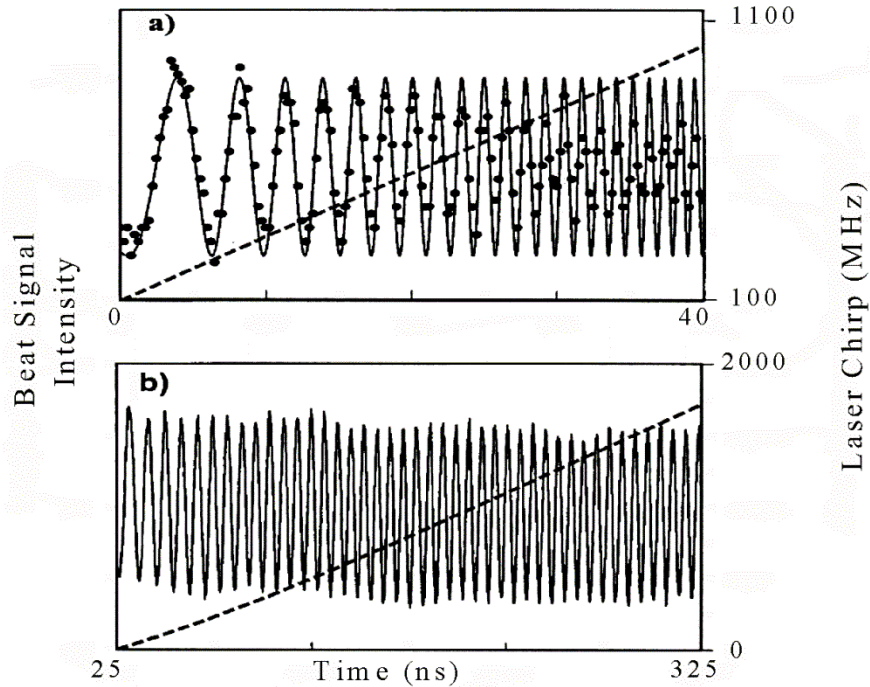


Figure 5.4. a) Interferometer output intensity beat signal versus time during an 80 ns frequency chirp. Filled circles, recorded data; solid curve, fit of the linear frequency chirp to the data; dashed line, frequency of the fit to the beat signal. b) Interferometer output intensity beat signal versus time during a portion of a 350 ns frequency chirp. Solid curve, recorded data; dashed curve, frequency of the fit to the beat signal.

Frequency-Swept Coherence

Laser coherence during high-speed tuning is difficult to measure. We employed a method based on cross correlation that is applicable to quasi-linear frequency excursions.

The basis of the method is clarified by simulation. We generate simulated beat signals of the form $I_{\text{beat}}(t) \propto \sin[at + bt^2 + ct^3 + \phi_0(t)]$, where $\phi_0(t)$ is a phase jump history of model (4) described above. Beat signals generated with different random phase histories are cross correlated according to

$$CCR(\tau) = \int I_{\text{beat}}(t)^{(1)} I_{\text{beat}}^{(2)}(t - \tau) dt, \quad (5-4)$$

where the superscripts (1) and (2) imply different beat signal traces. We calculated 20 cross correlations among simulated beat signals and averaged their magnitudes. The results are displayed in figure 5.5 a). In these simulations, $\tau_c = 1 \mu\text{s}$, $a = 1 \text{ MHz}$, $R_{\text{CH}} = 2b = 250 \text{ kHz}/\mu\text{s}$, and $c = 0$. The temporal FWHM of the cross correlation, τ_{cc} , is found to provide information on the laser coherence time through the relation $\tau_c = (R_{\text{CH}} \tau_{\text{cc}})^{-1}$. This relation implies that τ_{cc} is approximately the inverse of the frequency swept out in the laser coherence time. That is, the cross-correlation will be non-negligible over a time approximately equal to $1/(R_{\text{CH}} \tau_c)$. This result is generic, provided that coefficient c is suitably small. In figure 5.5 b) we plot the magnitude of a typical cross correlation performed between two 50-ns-long experimental recordings of beat signals during frequency sweeps.

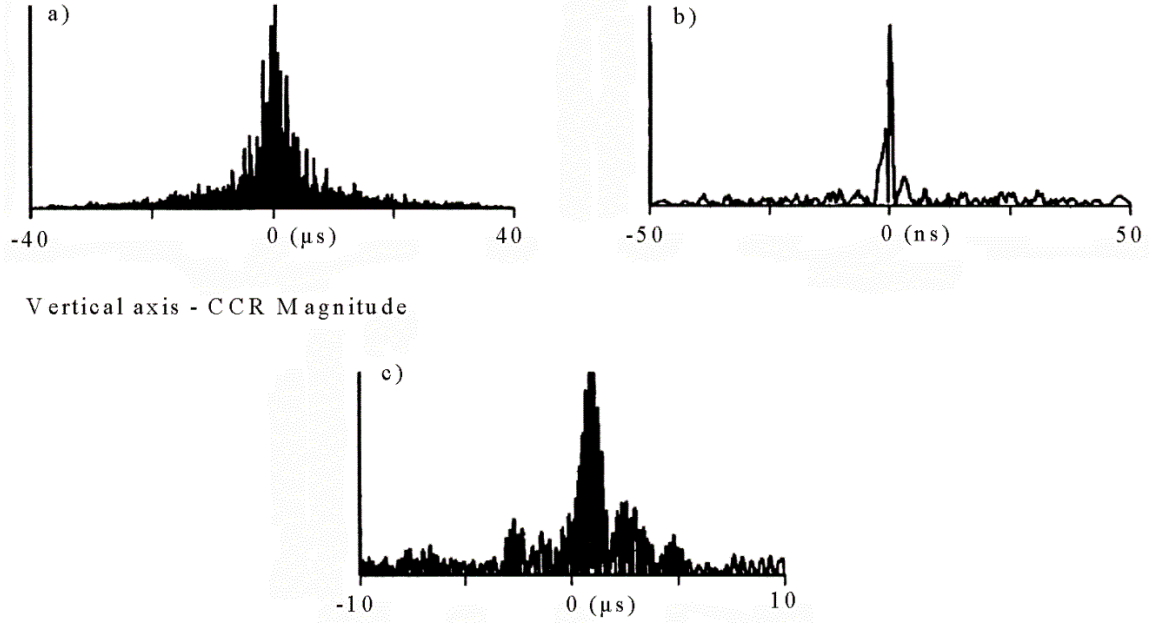


Figure 5.5. a) Average cross-correlation magnitude of simulated beat signals during frequency sweeps of phase-noisy laser field. b) Cross-correlation magnitude for two experimental beat signals during frequency sweeps of $R_{ch} \approx 23\text{GHz}/\mu\text{s}$. c) Cross-correlation magnitude for two experimental beat signals during frequency sweeps of $100\text{kHz}/\mu\text{s}$.

Here $\tau_D = 11\mu\text{s}$ and $R_{CH} = 23\text{GHz}/\mu\text{s}$. The average value of τ_{cc} calculated from 15 similar pairs of experimental traces is approximately 1.0ns , which is the inverse of our $\approx 1\text{GHz}$ chirp bandwidth, implying that $\tau_c \approx 50\text{ns}$. In figure 5.5 c) we plot the same cross correlation as in figure 5.5 b), except that $R_{CH} = 100\text{kHz}/\mu\text{s}$ and the chirp duration is $10\mu\text{s}$. We find a value of $\tau_{cc} \approx 1.8\mu\text{s}$ by averaging the FWHMs of 28 similar experimental traces. This result implies that $\tau_c = 6\mu\text{s}$.

Locking Suggestions

By monitoring the beatnote frequency in the unswept case and comparing it to the AOM frequencies it can be determined whether the laser has undergone a frequency shift [63].

This information can be used to adjust the laser diode current or the voltage across the EOC in order to cancel out some of the unwanted frequency deviations of the laser itself. That is, the linewidth of the unswept laser diode may be further narrowed by a feedback circuit which monitors the beatnote frequency of the self-heterodyned laser and simultaneously adjusts the injection current of the diode. This method may also be used to tailor the frequency chirp characteristics arbitrarily [64]. This system could be useful for time-dependent spectroscopic measurements, implementations of swept-carrier time-domain optical storage as well as in other applications.

CHAPTER VI

CONCLUSION

The motivation for the ability to manipulate the spontaneous radiation rate in a fiber based system is that it would allow an easy way to vary some of the relevant parameters for a variety of interesting and technologically important systems, e.g., fiber lasers and EDFAs. The technologies involved (doped fiber and FBGs) are reasonably mature.

The physical system and measurements thereupon explored in this work demonstrate that the complexities due to its non-two-level nature (inter/intra-Stark level dynamics) make a definitive demonstration of spontaneous lifetime difficult but maybe not impossible. By choosing appropriate system parameters and techniques, e.g., FBG resonance, excitation bandwidth, sample absorption and physical construction, method of sample excitation and signal detection scheme a modification might yet be measured.

As other systems and technologies mature , e.g. photonic crystal fibers, radiative lifetime modification in optical fibers may lead to a more complete control of the effects of the quantum light field on systems of scientific and technological interest.

REFERENCES CITED

- 1) E.M. Purcell, Phys. Rev. 69, 681 (1946)
- 2) Hulet, et al., Phys. Rev. Lett., 55, 2137 (1985)
- 3) Jhe, et. al., Phys. Rev. Lett., 58, 666 (1987)
- 4) Lange and Walther, Phys. Rev. A 48, 4551 (1993)
- 5) Neogi, et. al., Phys. Rev. B 66 (2002)
- 6) Vesseur and Polman, Appl. Phys. Lett., 99 (2011)
- 7) Tocci, et. al., Phys. Rev A 53 2799, (1996)
- 8) Boroditsky, et. al., J. Light Wave Technol. 17, 2096 (1999)
- 9) Romanov, et. al., J. Appl. Phys. 91, 9426 (2002)
- 10) Englund, et.al., Phys. Rev. Lett., 95, (2005)
- 11) Jiang, et. al., Phys. Rev. A 83 (2011)
- 12) Leistikow, et. al., Phys. Rev. Lett., 107, (2011)
- 13) Liu, et. al., Opt. Express, 19 (2011)
- 14) Gopinath, Appl. Phys. Lett., 96 (2010)
- 15) Yablonovitch, Phys. Rev. Lett., 58, 2059 (1987)
- 16) Ho, et. al., Phys. Rev. Lett., 65, 3152 (1990)
- 17) E. Yablonovitch, Proc. 4th Int. Symp. Foundations of Quantum Mechanics, Tokyo (1992)
- 18) E. Yablonovitch, J. Opt. Soc. Am. B 10 (1993)
- 19) Allenn L., Eberly, J.H. (1987), Optical Resonance and Two-Level Atoms. Dover Publications, Inc. New York
- 20) Dirac, Proc. Roy. Soc., A114, 243 (1927)
- 21) Milonni,P. W. (1993), The Quantum Vacuum. Academic Press, Inc., San Diego

- 22) Loudon, R. (2000), *The Quantum Theory of Light*. Oxford University Press, New York
- 23) Shore and Knight, *J. Mod. Opt.* 40, 1195 (1993)
- 24) Yun and Chang, *IEEE Transactions on Microwave Theory and Techniques*, 49, 549 (2001)
- 25) Morey, et. al., *SPIE Vol. 1169, Fiber Optic and Laser Sensors VII* (1989)
- 26) Krauss, et. al., *Nature* 383, 699 (1996)
- 27) Blanco, et. al., *Nature* 405, 437 (2000)
- 28) Agrawal, G. P. (2010) *Fiber-Optic Communications Systems*. John Wiley & Sons, Inc., Hoboken, New Jersey
- 29) Othonos, *Rev. Sci. Instrum.* 68, 4309 (1997)
- 30) Hill, et.al., *Appl. Phys. Lett.* 32, 647 (1978)
- 31) Lam and Garside, *Appl. Opt.* 20, 440 (1981)
- 32) Yeun, *Appl. Opt.* 21, 136 (1982)
- 33) Desurvire and Simpson, *Opt. Lett.* 15, 547 (1990)
- 34) Wang, et.al., *J. Appl. Phys.* 95, 4025 (2004)
- 35) Du and Cormack, *J. Non-Cryst. Solids*, 351, 2263 (2005)
- 36) Todoroki, et. al., *J. Appl. Phys.* 72, 5853 (1992)
- 37) Reddy, et. al., *J. Alloy. Compd.* 509, 4047 (2011)
- 38) Tanabe and Hanada, *J. Non-Cryst. Solids*, 196, 101 (1996)
- 39) Fox, *Optical Properties of Solids*, Chpt. 9
- 40) Mortier, et. al., *J. Alloy. Compd.* 300-301, 407 (2000)
- 41) Stepanov and Hernandez, *Opt. Lett.* 30, 1926 (2005)
- 41) 3M Application Note (2001): *Fusion Splicing of Erbium Doped Optical Fiber*. 3M Optical Components, Austin Texas

- 42) Bigot, et. al., Phys. Rev. B 66 (2002)
- 43) Jurdyc, et. al., J. Lumin. 58, 316 (1994)
- 44) Weber, et.al., J. Lumin. 12/13 729 (1976)
- 45) Brundage and Yen, Phys. Rev. B 34, 8810 (1986)
- 46) G. F. Imbusch, Phys. Scripta, T19, 345 (1987)
- 47) Motegi and Shionoya, J. Lumin. 8, 1 (1973)
- 48) Taylor and Hessler, Phys. Lett A 50, 205 (1974)
- 49) Selzer, et. al., Phys. Rev. Lett., 36, 813 (1976)
- 50) Reineker, et. al., Phys. Rev. B 29, 4546 (1984)
- 51) Garcia, et. al., J. Lumin. 83-84, 417 (1999)
- 52) Hofmann and Orrit, J. Phys. Chem. B 110, 18925 (2006)
- 53) Yen and Brundage, J. Lumin. 36, 209 (1987)
- 54) Zeller and Pohl, Phys. Rev. B 4, 2029 (1971)
- 55) W. A. Phillips, Rep. Prog. Phys. 50, 1657 (1987)
- 56) Enss and Hunklinger, Phys. Rev. Lett. 79, 2831 (1997)
- 57) Coppersmith, Phys. Rev. Lett. 67, 2315 (1991)
- 58) Laird and Schober, Phys. Rev. Lett. 66, 636 (1991)
- 59) Nalbach, Phys. Rev. B 71 (2005)
- 60) Busiello and Saburova, Physica B 263-264, 324 (1999)
- 61) Boggs, et. al., Opt. Lett., 23, 1906, (1998)
- 62) Labachellerie, et. al., J. Phys. III France 2, 1557 (1992)
- 63) Greiner, et. al., Opt. Lett., 23 (1998)
- 64) Mossberg, et. al., US Patent 6,034,976